JUSTUS-LIEBIG- UNIVERSITÄT GIESSEN

Justus-Liebig-Universität Gießen
Fachbereich 08 – Biologie und Chemie
Physikalisch-Chemisches Institut
AG Prof. Dr. Herbert Over

Ruthenium-Iridium Mixed Oxides $Ru_xIr_{1-x}O_2$ Prepared by Sol-Gel Method and Applied to Catalytic Methane Combustion

Inaugural-Dissertation
zur Erlangung des akademischen Grades
doctor rerum naturalium
(Dr. rer. nat)

vorgelegt von
Omeir Khalid

Giessen, Juni 2021

The beginning seems to be more than half of the whole.
-Aristotle

Erstgutachter: **Prof. Dr. Herbert Over**
Zweitgutachter: **Prof. Dr. Bernd Smarsly**

Selbstständigkeitserklärung

Die vorliegende Arbeit fasst die wesentlichen Ergebnisse der Arbeiten zusammen, welche im Zeitraum von Oktober 2017 bis April 2021 in der Arbeitsgruppe von Prof. Dr. Herbert Over (Physikalisch-Chemisches Institut der Justus-Liebig-Universität Gießen) durchgeführt wurden.

Ich erkläre: Ich habe die vorgelegte Dissertation selbstständig und ohne unerlaubte fremde Hilfe und nur mit den Hilfen angefertigt, die ich in der Dissertation angegeben habe. Alle Textstellen, die wörtlich oder sinngemäß aus veröffentlichten oder nicht veröffentlichten Schriften entnommen sind, und alle Angaben, die auf mündlichen Auskünften beruhen, sind als solche kenntlich gemacht. Bei den von mir durchgeführten und in der Dissertation erwähnten Untersuchungen habe ich die Grundsätze guter wissenschaftlicher Praxis wie sie in der „Satzung der Justus-Liebig-Universität Gießen zur Sicherung guter wissenschaftlicher Praxis" niedergelegt sind, eingehalten.

This dissertation summarises the most important results of the work carried out between October 2017 and April 2021 in the research group of Prof. Dr. Herbert Over (Institute of Physical Chemistry, Justus Liebig University Giessen).

I declare: This thesis was written by myself and without any unauthorised outside help. I have marked quotations taken verbatim, from the literature or from personal communications accordingly. The principles of good scientific practice, as documented in the relevant statutes of Justus Liebig University, have been applied to all studies that makes up this thesis.

21.06.2021

Datum/Date

Unterschrift/Signature

Beteiligung an wissenschaftlichen Arbeiten

O. Khalid, T. Weber, G. Drazic, I. Djerdj and H. Over, *Journal of Physical Chemistry C*, 2020, **124**, 18670-18683.

O. Khalid, A. Spriewald Luciano, G. Drazic and H. Over, 2021, *submitted to ChemCatChem*, 2021.

Z. Wang, O. Khalid, Y. Wang, T. Weber, A. Spriewald Luciano, W. Zhan, B. Smarsly and H. Over, 2021, *to be submitted to ChemCatChem.*

T. Weber, M. J. S. Abb, O. Khalid, J. Pfrommer, F. Carla, R. Znaiguia, V. Vonk, A. Stierle and H. Over, *Journal of Physical Chemistry C*, 2019, **123**, 3979–3987.

Y. Sun, P. Cop, I. Djerdj, X. Guo, T. Weber, O. Khalid, Y. Guo, B. M. Smarsly and H. Over, *ACS Catalysis*, 2019, **9**, 10680–10693.

P. Cop, R. Maile, Y. Sun, O. Khalid, I. Djerdj, P. Esch, S. Heiles, H. Over and B. M. Smarsly, *ACS Applied Nano Materials*, 2020, **3**, 7406–7419.

Y. Sun, C. Li, I. Djerdj, O. Khalid, P. Cop, J. Sann, T. Weber, S. Werner, K. Turke, Y. Guo, B. M. Smarsly and H. Over, *Catalysis Science and Technology*, 2019, **9**, 2163–2172.

S. Urban, I. Djerdj, P. Dolcet, L. Chen, M. Möller, O. Khalid, H. Camuka, R. Ellinghaus, C. Li, S. Gross, P. J. Klar, B. Smarsly and H. Over, *Chemistry of Materials*, 2017, **29**, 9218–9226.

T. Weber, J. Pfrommer, M. J. S. Abb, B. Herd, O. Khalid, M. Rohnke, P. H. Lakner, J. Evertsson, S. Volkov, F. Bertram, R. Znaiguia, F. Carla, V. Vonk, E. Lundgren, A. Stierle and H. Over, *ACS Catalysis*, 2019, **9**, 6530-6539.

Abstract

The mechanism of the methane combustion reaction is split into an initial activation of the C-H bond to form methyl (CH_3) and methylene (CH_2), followed by either a direct oxidation to CO_2 or alternatively to the formation of CO and H_2 via the formaldehyde route first. This work presents ruthenium-iridium mixed oxides ($Ru_xIr_{1-x}O_2$) applied to methane combustion for the first time. The high activity of ruthenium during catalytic oxidation reactions and the ability of iridium to activate the C-H bond at low temperatures are combined to form promising materials.

The Pechini sol-gel method allows to prepare the rutile ruthenium-iridium mixed oxides ($Ru_xIr_{1-x}O_2$) with high compositional and structural control throughout the whole composition range x. In addition, a slightly modified route enables the preparation of supported ruthenium-iridium mixed oxides ($Ru_xIr_{1-x}O_2@TiO_2$) in order to increase the noble metal utilization for catalytic purposes.

With X-ray diffraction and X-ray photoelectron spectroscopy a core-shell-like structure has been revealed. The metallic core shows a miscibility gap in the composition range $x=0.21$ and $x=0.74$ forming fcc-$Ru_{0.21}Ir_{0.79}$ and hcp-$Ru_{0.74}Ir_{0.26}$, as confirmed by Rietveld refinement. The overgrown oxide, unlike the metallic core, shows no segregation throughout the entire composition range, shown by systematic composition-dependent shifts for the rutile (101) reflection spot (XRD) and O 1s binding energy (XPS) for the various compositions, indicating the successful formation of solid solutions. Raman spectroscopy underpins the successful formation of oxide solid solutions by showing a continuous shift in the wavenumbers of the Raman active modes according to the ruthenium (iridium) content.

The number of accessible surface noble metal atoms in the supported materials ($Ru_xIr_{1-x}O_2@TiO_2$), measured via CO chemisorption experiments, determine the relative active surface areas, which are required for proper normalization of the catalytic activities in terms of space-time-yield. Additional XPS studies confirm high dispersion of the active component on the TiO_2 support by revealing high relative surface noble metal concentrations, three to five times higher than as expected from the nominal loading (5 mol%). This indicates the high amount of interface between support and active component, which is mandatory for a good combustion catalyst to show thermal stability and hinder sintering, for instance.

Catalytic activity tests of the unsupported $Ru_xIr_{1-x}O_2$ catalysts are conducted with the prototypical CO oxidation reaction under oxidizing and under stoichiometric reaction conditions. The metallic core is buried and does therefore not contribute to the activity. IrO_2 is the least active of the presented materials. Surprisingly, not the pure RuO_2 but the

$Ru_{0.875}Ir_{0.125}O_2$ has proven itself as the best catalyst validating the harmonious and synergistic interplay of both noble metals. All $Ru_xIr_{1-x}O_2$ catalysts are bulk-stable under the reaction conditions considered. However, upon CO oxidation reaction the Ir^{4+} concentration at the mixed oxide surface is significantly enhanced with respect to its bulk composition.

Catalytic and kinetic data for the methane combustion over both unsupported $Ru_xIr_{1-x}O_2$ and supported $Ru_xIr_{1-x}O_2@TiO_2$ catalysts with varying compositions x are presented. In absolute contrast to the CO oxidation reaction, pure RuO_2 is the least active catalyst for methane combustion. However, not the analogue counterpart, pure IrO_2, but $Ru_{0.25}Ir_{0.75}O_2$ showed the highest intrinsic activity. The same trend can be observed for the supported materials ($@TiO_2$), where $Ru_{0.25}Ir_{0.75}O_2@TiO_2$ is the most active material. Surprisingly, even $Ru_{0.75}Ir_{0.25}O_2$ and $Ru_{0.75}Ir_{0.25}O_2@TiO_2$ are remarkably active in methane combustion, indicating that little iridium in the mixed $Ru_xIr_{1-x}O_2$ oxide component improves the activity of the methane combustion considerably.

Recalling the results from both CO oxidation and methane combustion, the C-H activation is rate limiting in methane combustion rather than the further oxidation to CO and CO_2. Additional reaction order experiments underline this statement by revealing a reaction order of zero for O_2 and a reaction order of one for CH_4, implying that the reaction rate correlates with the superficial population of methane molecules while the dissociative adsorption and supply of oxygen at the active site for further oxidation are not hampered.

The relatively inferior performance of pure RuO_2 during methane combustion obviously shows that iridium is important for the initial activation of methane but the admixture of ruthenium is mandatory to guarantee efficient oxidation of the methyl and methylene to form CO_2. Thus, accompanied by synergistic effects, the ruthenium-iridium mixed oxides are uncovered as promising candidates, which can compete with the Pd-based benchmark catalysts as concluded from direct comparison of $T50$ and $T90$ values, where the conversion is 50% and 90% respectively. Especially the $Ru_{0.75}Ir_{0.25}O_2@TiO_2$, with a slightly lower intrinsic activity compared to pure $IrO_2@TiO_2$ but much higher amount of the more abundant ruthenium turns out to be most interesting for further methane combustion studies.

Table of Content

1. Introduction: Methane – Curse and Blessing

Human society has become the dominant force in driving enormous changes in the environment and climate of our planet, especially since the mid-20th century.[1] Although there are still many scientists who doubt the human-induced alterations in the ecosystem „Earth",[2,3] global warming is real and undeniable.[4] Overpopulation is hard to ignore and the human footprint is accompanied by a significant increase in greenhouse gases such as carbon dioxide. Up to the point at which humanity started to burn fossil fuels the concentration of CO_2 in the atmosphere was being kept in balance by nature. With the immense consumption of carbonaceous resources like wood, coal, and fossil fuels for power generation, this natural equilibrium is out of control.[5] The increase in average global temperatures is mainly attributed to emissions caused by humans.[6] The so-called "Kaya identity" signifies the total emission of greenhouse gases (in the original form limited to carbon dioxide) caused by human society.[7]

$$\#CO_2 = \frac{\#CO_2}{E} \cdot \frac{E}{GDP} \cdot \frac{GDP}{Cap} \cdot Cap \qquad\qquad (1.1)^{[7]}$$

The main drivers of the total emission ($\#CO_2$) are classified into socioeconomic factors including the gross domestic product (GDP) and the population (Cap) as well as technological drivers including the emissions per unit energy ($\#CO_2/E$) and the energy consumption per gross domestic product (E/GDP). If at all, the socioeconomic drivers mainly are subject to political and ethical discourses. Science and technology, however, can improve efficiency in both energy production and energy consumption to minimize greenhouse gases hazardous to our planet.

Global energy consumption is mainly driven by the industrial sector, the transportation sector (transportation of goods and services as well as public transport system), and the building sector (commercial and residential) with a share of about 50%, 20%, and 30% respectively.[8,9] Heat and mechanical work provide the energy required for transport systems, industrial manufacturing as well as electrical supply. Combustors convert chemical energy into thermal energy (heat) which is optionally converted to mechanical work by so-called heat engines, which is why about 85% of the global energy consumption is supplied by fossil fuels such as oil, coal, and natural gas.[10,11]

However, fossil fuels not only contain the needed chemical energy but also carbon, which is why about 25% of the total anthropogenic CO_2 are traced back to the transport sector[9,12,13] and another 60% are traced back to the use and production of electricity as stated by the International Energy Agency (IEA).[14] Thus, fossil fuels are almost solely responsible for

human-caused carbon dioxide, accounting for two thirds of all greenhouse gases.[15] The IEA further reports that over the last decade, more than 50% of global oil (petroleum) consumption has been used to meet 94% of the global transport energy demand to provide high-value transportation services to modern civilization.[9,16,17] The global vehicle stock is still increasing dramatically with a present stock of 1.4 billion and an estimated number of 2.0 billion in 2030.[9,16-18] Unfortunately, the conversion of petroleum goes hand in hand with high amounts of carbon dioxide, enhancing the natural greenhouse effect.[19] In addition, we face the equally problematic fact that the world's oil reserves are dwindling. Currently, the total oil reserves in the world are estimated at 1.5 trillion barrels of oil.[10,20] With a total oil consumption of about 100 million barrels per day, the reserves would last for another 40 to 45 years.[10]

Therefore, a shift towards carbon-free alternatives will play an essential role for our planet, yet unfortunately, this change is not happening fast enough. The energy transition hopes for technological innovations, especially in the renewable energy sector,[21,22] but forecasts predict that the global share of solar, wind, and other renewables in the total energy consumption will be only 2% in 2030, compared to 1% in the present (2020).[23,24] While society struggles to adapt to a carbon-neutral future, harmful changes in the environment naturally do not pause. Therefore, humanity will need an interim period characterized by rigorous efforts to achieve at least low-carbon energy balances in the upcoming decades.

Natural gas (fossil gas) consists primarily of methane, the hydrocarbon with the lowest carbon-to-hydrogen ratio providing the highest heat of combustion (thermal energy) per mole of carbon dioxide,[25] leading to the lowest $\#CO_2/E$ ratio and a higher gravimetric energy density of methane ($56\,\mathrm{kJ\cdot g^{-1}}$) compared to petroleum ($44\,\mathrm{kJ\cdot g^{-1}}$) and coal ($39\,\mathrm{kJ\cdot g^{-1}}$).[25] Because of that, methane experiences an increasing trend and share in the global total energy consumption, already at a current share of about 24%.[24] The estimated reserves of about 1.1 trillion barrels of oil equivalent last for about 50 to 60 years at the current rate of consumption.[25] This estimation does not include undiscovered but still suspected natural gas as well as methane reserves present in clathrates (methane hydrates) found under shallow continental shelves in the ocean and in Arctic permafrosts[26] with an estimated amount of about two times that of methane in natural gas reserves. This abundance would last for another 100 years, however, technological knowledge is considered limited so far to enable sufficient and successful methane production from these hydrates.[27]

The projected worldwide energy mix for 2040 shows that the share of natural gas will rise slightly from 24% (2018) to 25% (2040), while that of oil will decrease significantly from 31%

(2018) to 28% (2040).[28] The seemingly small increase of 1% for natural gas is substantial considering that the trend should actually be moving in direction of renewable energies. However, methane from biogas is also a promising energy vector for future circular energy economy based on renewable energies,[25] which is why the interest in energy production based on methane is not limited to the abundance of natural gas.

Unfortunately, methane has a global warming potential 84 times (as per same mass) higher than carbon dioxide over the first 20 years after release and about 28 times higher after a whole century.[29] Therefore, the use of natural- and biogas based fuels in transportation requires an efficient oxidation catalyst in particular under lean conditions to prevent methane-slip to the atmosphere[30], otherwise the beneficial aspect of a reduced carbon dioxide emission is nullified. Furthermore, methane is the most difficult hydrocarbon to oxidize catalytically so that a relatively high temperature is needed for the reaction to proceed with an acceptable rate.[31,32] The downside of methane, which is both a curse and blessing, also becomes clear considering that the rising temperatures due to climate change degenerate the earlier mentioned methane clathrates ($CH_4 \cdot xH_2O$) to water and free methane. The latter is bubbling to the water surface and slipping to the atmosphere[26,27,33] further accelerating the climate change, as if in an endless loop. The catalytic methane combustion reaction thus is of great importance not only for more decades of efficient energy production from natural gas and biogas but for preventing methane-slip in general, which is seen as a novel type of global threat.[26,34]

Despite the fact that noble metals are very active during combustion reactions, they are also very rare and expensive. Thus, their application must be studied carefully in order to employ suitable materials with a maximum utilization of the precious metals. This work examines ruthenium-iridium mixed oxides, referred to as $Ru_xIr_{1-x}O_2$, with the motivation to combine the catalytic properties of pure RuO_2 and IrO_2 and to uncover synergistic effects which may give promising alternatives to the benchmark catalysts (Pd) for catalytic methane combustion.

2. Catalytic Combustion

2.1 Thermal Combustion vs. Catalytic Combustion

Catalysed combustion reactions (complete oxidation) have been extensively studied over the last four decades,[35-39] mainly because of the following advantages:

1. Lower working temperatures (<1400 °C) resulting in higher energy efficiency
2. No limitation of the fuel-oxygen-mixture by the explosion range
3. Less harmful pollutants like NO_x and less reactant-slip into the atmosphere
4. Controllable reaction paths

In conventional flame combustion (thermal combustion), the high temperatures initiate the formation of radicals, which rapidly undergo the oxidation steps to form carbon dioxide and water as the main products.[36] The flame working temperatures reach about 1500 °C to 2000 °C depending on the choice of fuel as well as the partial pressures of both the fuel and oxygen. At such high temperatures, formation of nitrogen oxides is well known[39-41] whereby nitrogen is fed by the fuel or is introduced from air. Thermal combustion occurs only within the explosion limits given by the lower flammability limit (LFL) and the upper flammability limit (UFL).[42] In the case of methane, for instance, only mixtures of about 4% (LFL) to 17% (UFL) by volume of air are flammable.[43] While too high concentrations of fuel are too rich to burn, an insufficient amount of fuel results in lean mixtures with unstable combustion flames. This in turn leads to incomplete conversion with a fuel-slip to the atmosphere.

Unlike in thermal combustion, the oxidation of the fuel on a catalytically active surface takes place without the contribution of open flames.[39] The catalysts surface interacts with the molecules to enable alternative reaction pathways with decreased energetic barriers (activation energies). Therefore, lower working temperatures well below the auto-ignition temperature (537 °C for methane)[44] are required, which is why the risk of explosions is small as well.

The benefits of catalytic conversion are undeniable, but inevitably come at the expense of using often expensive catalyst materials. The right type and design, technological implementation, and process parameters need to be considered to achieve the best performance. Noble metals, which are most promising for combustion reactions, additionally are low abundant (precious metals), examining their intrinsic activity to improve efficiency therefore is an important scientific task.
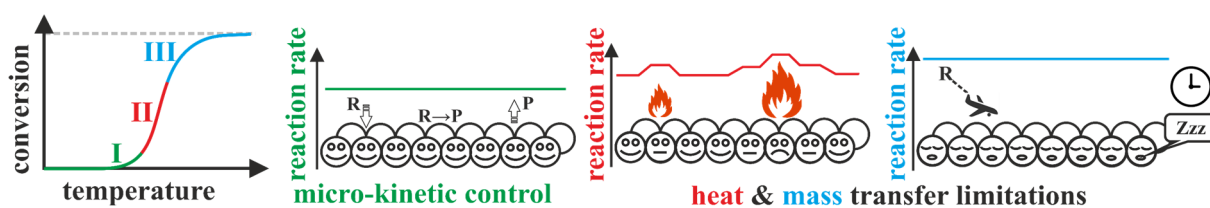
Figure 2.1: Illustration of a typical catalyst performance (turn-over or conversion as a function of temperature) with three main regions. In region I, micro-kinetics are rate-determining. In region II, the increased heat of reaction results in hot spots and insufficient heat transfer. The third region is characterized by a lack of reactant molecules above the surface, resulting in mass transfer limitations that may be rate-limiting.

The typical performance of a (combustion) catalyst identifies three common regions, denoted as I, II and III in **Figure 2.1**.[36,45] In the first region, micro-kinetics, including adsorption, surface reactions, and desorption, are rate-determining. Kinetic data attributed to the active site, such as the activation energy and reaction orders, can be studied. The heat of reaction introduced by the negative enthalpy change (of the combustion reaction) in region I is small and transferred by the gas stream, so that the temperature of the catalysts surface is under control. As the surface temperature increases (region II), the reaction rate increases according to the Arrhenius equation[46] as well. Furthermore, the catalyst's temperature additionally rises due to the increased heat of reaction compared to region I and the gas stream cannot sufficiently dissipate this heat. The catalyst experiences irregular hot spots and the observed catalytic data represent the surface reaction unevenly, which is why they can no longer be designated as kinetic data. Therefore, in this work a distinction is made between the terms "catalytic data" and "kinetic data", whereby the former refers to results, which may represent superimposed sets of kinetic data due to different reaction rates on the catalyst surface. In region III, the catalyst approaches at high temperatures or rather high conversions and the diffusion of the reactants to the catalysts surface (film diffusion) becomes relevant. These mass transport limitations (macro-kinetics) dominate and the surface is depleted with reactants, the micro-kinetics are no longer rate-determining. Further details on micro- and macro-kinetic control are given in chapter 7.2.

2.2 Support Effects

A support, or carrier, is used in heterogeneous catalysis for the following reasons.

1. To increase the accessible surface area of the active component by providing a matrix that allows high dispersion
2. To reduce sintering of the active component and thus improve thermal stability
3. To avoid hot spots for improved heat transfer (carrier as heat condenser)
4. To improve the catalytic performance by contributing either directly with own activity or by beneficial interactions between the support and the active component (metal-support interactions)

To a first approximation, the active component forms spherical particles with a surface-to-volume ratio given by $3 \cdot r^{-1}$ where r is the radius of the sphere. For a constant mass or volume of (catalyst) material the surface area therefore increases with smaller particle sizes according to $A = V \cdot (3 \cdot r^{-1})$. Nevertheless, a larger surface area is not synonymous with a larger active surface area. For example, porous materials may increase the dispersion of the active component due to their own high internal surface area providing more nucleation sites,[47] however, this internal surface area may be meaningless if mass transport limitations within the pores become rate-determining, resulting in a small or negligible contribution to the catalytic performance. In addition, less of the precious metal adheres to the outer surface, resulting in a decrease of the product yield. If the pores are too small and the reactants collide more frequently with the geometric boundaries (pore walls) than with other molecules, pore diffusion (Knudsen diffusion) additionally occurs.[48] On the one hand, decreasing pore sizes lead to higher total surface areas, but on the other hand, too small pores are even counterproductive. Several works report optimized activity utilizing mesoporous carriers with pore sizes of 6 to 8 nm.[49] For non-porous or macro-porous supports, however, the catalytic performance scales with the accessible number of active sites since no inner mass transportation limits occur.

Another essential task of the support material is to maintain the high dispersion of the active component on the carrier even under harsh reaction conditions, preventing the active component from thermodynamically induced sintering processes.[50] Surface atoms differ from those in the bulk because they cannot form bonds towards the interface, which leads to unsatisfied bond structures (dangling bonds). A reconstruction or rearrangement of the surface takes place, resulting in a distorted and stretched structure with higher energy compared to the symmetric and energetically saturated bulk. Particle growth will reduce these surface tensions

and favour the total Gibbs free energy.[50] However, a suitable carrier can suppress this thermal instability through energetically favourable interactions at the interface, resulting in reduced driving forces for sintering.

Furthermore, interactions between the support material and the active component can induce additional catalytic improvement as well by so-called metal-support interactions.[51,52] This term refers to several phenomena, most notably charge-transfer effects (electron exchanges), unique synchronized reactions occurring only at the three-phase boundaries (interfacial perimeter), spillovers across the metal-support interface, carrier-induced shape and morphology manipulation of the active component due to adhesion energies, as well as so-called strong metal-support interactions.[52] The latter is briefly explained by the formation of sub-oxides originating from the carrier material and overgrowing the active component with only very few layers to minimize the surface energy.[52-54] Complete coverage of the active component leads to deactivation, however, a partially covered surface introduces Lewis acidic sites, known to enhance the catalytic activity.[52]

3.   Methane Conversion – A Short Review

3.1 CH$_4$ – Chemical Properties

Methane is a chemically inert molecule with a central carbon tetrahedrally surrounded by four hydrogen atoms forming four strong covalent C-H bonds ($\Delta_d H$=440 kJ·mol^{-1}) which are only weakly polarized due to very similar electronegativities of carbon at 2.56 and of hydrogen at 2.21 relative to the Pauling scale.[55,56] Although this slight difference in electronegativity leads to partial charges, δ^+ for the H- and δ^- for the C-atom, the resulting electric bond dipole moments sum to zero, which is a consequence of the symmetry of methane. Therefore, the total molecular dipole moment vanishes, i.e. the molecule is non-polar which inhibits intermolecular forces and thus the reactivity. Furthermore, free methane is an extremely weak acid with a pK_a of about 50 (K_a=[CH$_3^-$]·[H$^+$]·[CH$_4$]$^{-1}$=10^{-50} mol·L^{-1}),[57] which is an equilibrium balance extremely favouring the protonated (CH$_4$) species, methane is thus effectively unable to donate a proton. Moreover, methane shows a very low proton affinity E_{pa} (CH$_4$+H$^+$→CH$_5^+$),[58] which is why it will not participate as a reactant in acid-base-chemistry. Due to this inertia, high temperatures (>1400 °C) and aggressive reaction conditions are necessary to activate methane in the absence of a catalyst, rendering conventional thermal combustion quite inefficient.

The following paragraphs give a short review of the economically and scientifically most important catalytic conversions (syngas formation, partial oxidation, and combustion) of methane and qualitatively ranks the catalytic materials implemented. This little review aims to show the relevance of ruthenium and iridium and the intention to intermix both to form a mixed oxide.

3.2 Syngas Formation from Methane

Although 90% of natural gas is used for power production and transport services, a significant proportion of about 3% to 4% is flared as waste in oil production (associated gas flaring) in countries such as Russia, Nigeria, Iran, Iraq.[56,59] Gas flaring is also practised for security reasons to release pressure in petrochemical plants where methane from various chemical processes (non-associated gas flaring) accumulates.[60] This wasteful behaviour is attributed to the three orders of magnitude lower volumetric energy density of methane (30-40 MJ·m^{-3}) compared to oil (40 MJ·dm^{-3}) and the resulting difficulties in transportation of fossil gas in pipelines and LNG-tankers (liquefied natural gas).[56] Less natural gas would undergo

inadequate flaring if profitable conversion routes existed to convert methane right at the wellhead into more easily transportable and valuable chemicals/liquids.

Synthesis gas (syngas), a mixture of CO and H_2, is an important feedstock in the chemical industry and can be formed by catalytic conversion of methane (and other hydrocarbons) via steam reforming and dry reforming.[56,61] The global demand for syngas, which is mainly needed for ammonia production (Haber-Bosch process[62]), methanol production (BASF process[63]) and synthetic hydrocarbon production (Fischer-Tropsch process[64]), is almost exclusively obtained from natural gas.[63]

In steam methane reforming (SMR), methane is mixed with water in a highly endothermic reaction to form carbon monoxide and dihydrogen (**equation 3.1**).

$$CH_{4(g)}+H_2O_{(g)}\rightarrow CO_{(g)}+3H_{2(g)} \qquad \Delta H_c(298\ K) = +206\ kJ\cdot mol^{-1} \qquad (3.1)^{[65]}$$

To optimize the hydrogen yield, the carbon monoxide can be converted with another equivalent of water to carbon dioxide and additional hydrogen in the so-called water-gas shift reaction (**equation 3.2**).

$$CO_{(g)}+H_2O_{(g)}\rightarrow CO_{2(g)}+H_{2(g)} \qquad \Delta H_c(298\ K) = -41\ kJ\cdot mol^{-1} \qquad (3.2)^{[65]}$$

The group VIII transition metals, including iron, cobalt, and nickel as well as the platinum group members, are catalytically active for the SMR reaction.[56] In particular, the cheap Ni-based materials experimentally and theoretically show sufficient activity, which explains that these catalysts are used commercially for steam reforming for more than 50 years.[56,66] Theoretical calculations interestingly define ruthenium (together with rhodium) as the most active noble metal for steam methane reforming, modelling the activation step of methane to methyl ($CH_4\rightarrow CH_3$*) as the rate determining step.[65] However, this is in conflict with the results from Ertl et al., who report that no activation of methane has been found for RuO_2.[67] Iridium-based catalysts are rarely found for steam reforming reactions in general and there is no report about steam reforming of methane over iridium catalysts.

Considering the high emission of greenhouse gases, the chemical reduction of CO_2 to chemical feedstock is considered highly desirable to achieve a low-carbon future.[68] The endothermic dry reforming of methane (DRM) transforms two main greenhouse gases, namely CH_4 and CO_2, to the valuable syngas mixture (**equation 3.3**).

$$CH_{4(g)}+CO_{2(g)} \rightarrow 2CO_{(g)}+2H_{2(g)} \qquad \Delta H_c(298\ K) = +247\ kJ \cdot mol^{-1} \qquad (3.3)^{[68]}$$

It must be taken into account that heat, which does not result from combustion of fossil fuels, must be fed to the strongly endothermic reaction to justify the positive contribution to the environment. Compared to the formation of syngas from steam reforming (**equation 3.1**), dry reforming results in a higher CO-to-H_2 ratio, enabling long-chain hydrocarbon synthesis in a subsequent Fischer-Tropsch process downstream.[69] However, industrial implementation is hampered by severe problems. The activation of CO_2 on transition metals is initiated by charge-transfer effects, forming CO_2^- species,[70] which are only stable at low temperatures. However, the net dry reforming reaction is endothermic and therefore requires high temperatures, obviously counterproductive. Another problem is the deactivation of the catalyst by carbon depositions that form due to pyrolysis and the Boudouard equilibrium.[70]

While non-noble metals such as nickel and cobalt show high activities, they lack in terms of thermal stability and coking resistance.[69,71] Noble metals, on the other hand, with ruthenium and iridium as the most active ones, show significantly higher resistance to carbon deposits, compromised with higher costs and limited abundance.[69] The formation of mixed oxides, such as the perovskite-type materials, recently received increasing attention, combining the advantages of noble and non-noble metals to form catalytically excellent yet affordable materials. $La_{0.4}Ru_{0.6}Al_{0.2}Ni_{0.8}O_3$ has proven itself to be one such promising candidate with beneficial synergistic effects.[72,73] Among the mixed noble metal systems, the bimetallic Pt-Ru@Al_2O_3 catalyst showed higher activity and stability compared to the monometallic species, highlighting the advantages of synergistic interactions for a more robust and more active catalyst.[74]

3.3 Partial Oxidation of Methane (CPOM)

The term partial oxidation actually refers to the direct catalytic conversion of methane with molecular oxygen to syngas,[56] sometimes it is also referred to the formation of other valuable molecules like methanol. The CPOM is a mildly exothermic reaction (**equation 3.4**), which allows moderate operating temperatures compared to the SMR and DRM reactions.

$$CH_{4(g)}+0.5O_{2(g)} \rightarrow CO_{(g)}+2H_{2(g)} \qquad \Delta H_c(298\ K) = -36\ kJ \cdot mol^{-1} \qquad (3.4)^{[56]}$$

Partial oxidation can occur employing less than a stoichiometric (sub-stoichiometric) amount of O_2, otherwise complete oxidation (combustion) dominates, as the C-H activation is usually

the most challenging, followed by less hampered oxidation steps.[56] Therefore, CO must be isolated as an intermediate and retained from further conversion to CO_2, achievable by a deficiency of oxygen population on the surface. An alternative to the direct route (**equation 3.4**) is the so-called combustion-reforming route[56] with an initial total/complete oxidation (**equation 3.5**) followed by either the steam reforming step (**equation 3.1**) or the dry reforming step (**equation 3.3**). The CO-to-H_2 ratio obtained by the CPOM is desirable for methanol synthesis downstream.[75]

$$CH_{4(g)}+2O_{2(g)} \rightarrow CO_{2(g)}+2H_2O_{(g)} \qquad \Delta H_c(298\ K) = -803\ kJ \cdot mol^{-1} \qquad (3.5)^{[56]}$$

In a review, Enger et al. pointed out that there is no uniform reaction pathway but an inherent dependence of the chosen catalyst system. They summarised the large amount of transition metal catalysts for efficient partial oxidation of methane.[81] Similar to the SMR reaction, the group VIII transition metals nickel, cobalt, and iron exhibit high turn-over frequencies (*TOF*s), high thermal stability, and low costs. That is why they are listed among the most promising candidates for CPOM.[76-80] Green et al. observed high yields of syngas over nearly all the noble metals with a high resistance to carbon deposition in the order Ru, Rh, Pt, Ir >> Pd > Ni.[78,81] Ruthenium catalysts with a 300 times lower mass loading still showed higher activity for CPOM than the nickel catalysts considered.[82] Furthermore, Green et al. synthesized so-called pyrochlores, a type of mixed oxides such as Ln_2RuO_7 and measured excellent yields of syngas.[83] A recent bimetallic catalyst screening revealed ruthenium-chromium mixed oxides as highly active with a syngas selectivity of 64%, being up to 18 times cheaper than the benchmark catalysts based on Rh, Pt and Pd.[84]

Nakagawa et al. studied the CPOM over iridium catalysts with several support materials and reported high catalytic activity comparable with Rh, which is most active for the partial oxidation.[85] Furthermore, the iridium-based materials showed no deactivation due to carbon deposition. The mechanism is reported to follow the two-step combustion-reforming pathway (**equations 3.5, 3.1, 3.3**). Despite these findings, iridium has not gained much interest for further use as a methane combustion catalyst, most probably due to the low abundance.

In addition to the formation of syngas, the direct partial oxidation of methane to more valuable chemicals like methanol and cyanides is highly interesting and designated as the "holy grail" of chemistry, although no ground-breaking results have yet been reported.[56] In fact, the direct conversion of methane to molecules other than CO or CO_2 always competes with the

exothermic Fischer-Tropsch process, the water gas-shift reaction, and the total oxidation (combustion) reaction.

3.4 Total/Complete Oxidation of Methane (Combustion)

Despite the fact that partial oxidation to syngas or other more valuable chemicals is desirable, 90% of the natural gas scooped is used for energy production, mainly transportation, electricity production, and heating.[56] Therefore, the methane combustion reaction (**equation 3.5**) aims at maximum yield of chemical energy stored in CH_4 and transformation into thermal energy and optionally into mechanical work (heat engines) and electricity (electrical generators). Six σ-bonds and two π-bonds are broken to form six σ-bonds and two π-bonds again, however, the much stronger C=O double bond ($\Delta_d H$=745 kJ·mol^{-1}) compared to the formal double bond in O_2 ($\Delta_d H$=498 kJ·mol^{-1}) leads to the strongly exothermic reaction enthalpy (−803 kJ·mol^{-1}).[56]

The high abundance, the lower C-to-H ratio, and the higher energy content of methane compared to other fossil resources[25] render the catalytic methane combustion reaction responsible for several hundred of articles published yearly, dealing with the question of what makes a good and stable methane combustion catalyst, as reported by Thomson Reuters Web of Science.[31] Main subjects include the examination of the active site in terms of turn-over frequencies and activation energies, the understanding of the reaction mechanism, the influence of the carrier on activity and stability and last but not least the deactivation due to sulfur, nitrogen oxides, water, as well as carbon poisoning or deposition.[25,32,35,56] Considering that methane is a 20 to 84 times worse greenhouse gas compared to CO_2, a methane-slip must be hindered, otherwise the use of methane/natural gas is even disfavoured. A good combustion catalyst therefore must ensure both total/complete oxidation and the highest possible conversion under real operating conditions.

3.4.1 Noble Metal Catalysts

Noble metals in general show very high turn-overs per site and time (turn-over frequency) and also exhibit a higher resistance to sulfur poisoning, which is why they are all promising candidates for combustion reactions. Palladium-based catalysts are considered best up to now, also because of a much lower volatility compared to the other members of the noble metal group, followed by rhodium and platinum.[31,35,86-90] Especially at low reaction temperatures Pd is more active than rhodium and platinum.[25,88,89] Rhodium has a one order of magnitude lower abundance than Pd, that is why it is not considered suitable for realistic industrial

implementations. Platinum, on the other hand, is accepted as the most promising catalyst for the combustion of ethane, propane and *n*-butane rather than for methane.[31,35,40]

The nature of the active phase of Pd-based catalysts is studied with extremely high interest in the literature to understand the excellent catalytic activity of palladium.[91-93] DFT calculations and synchrotron X-ray diffraction experiments reveal that either metallic Pd or under-coordinated sites in PdO are required to obtain efficient dissociative adsorption of methane.[94] This is in line with the negative apparent activation energy reported by Pfefferle et al., who observed an increase in conversion with decreasing temperatures after a pre-treatment of the catalyst at 800 °C. Metallic Pd is formed at such high temperatures, which contributes to the activity. However, when cooling down Pd partially is re-oxidized to PdO, which exhibits a higher catalytic activity than the metallic species, resulting in a negative apparent activation energy.[90][95] For this reason, there is a general consensus that PdO is the more active species at lower temperatures, while the metallic species features the activity at temperatures above 600 °C.[25,35,86,96,97] Pd or rather PdO has shown even higher activities when supported on γ-Al_2O_3, demonstrating beneficial interactions between support and the active component.[98]

The fact that palladium catalysts are vulnerable to sulfur poisoning due to formation of $PdSO_4$ species[99] and also towards water poisoning due to $Pd(OH)_2$ formation[100] fuels the ongoing search for alternative materials. Rhodium in the form of Rh_2O_3 is a candidate which reveals a higher tolerance than Pd to both sulfur but also water poisoning,[101,102] however, as mentioned Rh is substantially more expensive and less abundant than Pd.

The fact that Pt and Rh exhibit less yet comparable activities suggests that the magnificent performance of these elements can be traced back to properties characteristic of the platinum group members. The "catalytic wizardry" of noble metals, which has been realised during the industrial revolution, is mainly attributed to their outstanding bond-breaking abilities without being chemically consumed themselves.[37,103] The section of the periodic table of elements shown in **Figure 3.1** ranks the noble metals on the basis of their bond-breaking capability based on temperature-programmed reaction spectroscopy (TPRS) experiments.[103] Model catalysts with controlled structure and composition are exposed to the reactants under UHV (ultra-high vacuum) conditions and are subsequently heated to detect the products with a mass spectrometer. In combination with isotopic labelling of the reactant molecules, bond rupture and recombination can be studied, demystifying the individual catalytic performance of the noble metals.[103]

Ruthenium 44	Rhodium 45	Palladium 46	Silver 47
C—*—C N—*—C	C—*—C N—*—C	C—C N—C	C—C N—C
C—*—O H—*—H	C—*—O H—*—H	C—O H—*—H	C—O H—H
C—*—H	C—*—H	C—*—H	C—H
O—*—O	O—*—O	O—*—O	O—*—O

	Iridium 77	Platinum 78	Gold 79
* bond cleavage capability	C—*—C N—*—C	C—C N—C	C—C N—C
	C—*—O H—*—H	C—O H—*—H	C—O H—H
	C—*—H	C—*—H	C—H
	O—*—O	O—*—O	O—O

Figure 3.1: Excerpt of the periodic table of elements classifying the bond-breaking ability of the noble metal elements compiled from TPR experiments.[103] A decrease in bond rupture capability from left to right reveals ruthenium and iridium to be the most broadly suitable catalysts from this point of view.

Key steps during catalytic combustion of methane include the activation of the C-H bond in methane as well as the dissociation of molecular oxygen in order to achieve sufficient regeneration of the reduced catalyst. All elements of the platinum group exhibit the ability of C-H and O-O bond rupture as marked in **Figure 3.1**. Interestingly, palladium (but also platinum) shows a decreased potential for the C-C bond cleavage, which suggests that ruthenium, rhodium, and iridium may be very active for the activation and combustion of ethane and propane, for instance, where the C-C bond cleavage is the major task.[104] Indeed, ruthenium was found to be very active for the propane combustion reaction.[105] The decreasing trend in activity from left to right manifests ruthenium and iridium as the most active noble metals at least in terms of bond activation capabilities covering nearly all bonds available in lower alkanes and organic compounds. Note that this discussion refers to purely intrinsic activity and does not consider real operating conditions, where poisoning effects may dominate the actual performance.

While Pd and Pt are firmly integrated for combustion reactions, ruthenium experiences less interest due the volatility at higher temperatures,[106] showing a strong tendency to take higher oxidation states, resulting in volatile species like RuO_3 and RuO_4. Both show several orders of magnitude higher partial pressure in air atmosphere compared to RuO_2.[106-108] Moreover, the over-oxidation of RuO_2 is fuelled by nitrogen oxides,[108] unfortunately making RuO_2 even less considerable for real operating systems. On the other hand, the addition of ruthenium is also reported to positively affect the catalyst by providing very high resistance to sulfur

poisoning.[109] A screening of single noble metal catalysts during methane combustion recently reported by Kumsung et al. revealed high activity of ruthenium supported on Al_2O_3, only surpassed by rhodium based materials.[110]

In contrast to ruthenium-based catalysts, which are under advanced scientific debate in particular for syngas formation and partly also for combustion of methane, iridium shows hardly any reports on catalytic methane conversion except the pioneering works of Nakagawa et al.[85,111] Ever since, iridium has only briefly been explored as a part of the previously mentioned catalyst screening of Kumsung et al. investigating noble metals for methane combustion at 475°C. Iridium (supported on alumina) was inferior to the remaining platinum group members and therefore no further investigations of the kinetics have been carried out.[110] However, this study does not allow to assess whether the apparently low activity of iridium is of intrinsic nature or due to the preparation method, a low dispersion of iridium on the carrier or any other effects. It is not even clear if the iridium is present in the metallic state or as an oxide. Recently, Weaver et al. reported on low-temperature activation of methane under UHV conditions over a single-crystalline $IrO_2(110)$ surface. In temperature programmed reaction (TPR) experiments the oxidized surface of Ir(100) was covered with methane (and oxygen) at temperatures below 100 K and then the products such as CO, CO_2 and H_2O were detected between 150 and 600 K with a mass spectrometer while ramping the sample to 700-800 K.[112] The active phase has been assigned to a $IrO_2(110)$ layer. Two years later, it was further reported that methane adsorbs on under-coordinated iridium sites with the additional statement that on-top oxygen enhances the conversion of methane to CO_2 and water,[113] confirming the DFT calculations by Wang et al. seven years earlier.[114] Very recent in-situ Raman and in-situ DRIFTS (diffuse reflectance infrared fourier transform spectroscopy) measurements by Liu et al. emphasize the role of the oxidation state of iridium during methane activation over IrO_2 nanoparticles. They conclude that IrO_2 and also partially reduced iridium dioxide are the most active species.[115] Despite the innovative UHV and in-situ spectroscopy studies, still no catalytic data under steady-state conversion and under flow conditions exist for the methane combustion reaction.

3.4.2 Non-Noble Metal Oxides

The high prices and low abundance of noble metal oxides are the main reasons why non-noble metals are attracting more and more attention in catalytic (methane) combustion.[25,31,35-37,86,116] Non-noble metal oxides suppress the formation of NO_x species during catalytic fuel combustion and their multiple potential valence states support an expanded pool of redox cycles enabling unique catalytic pathways.[31,35] Additional phenomena such as high oxygen storage capacities due to high reducibility rapidly supply the active sites with monoatomic oxygen (Mars-van-Krevelen mechanism) required for regeneration.[117] Unfortunately, the various beneficial features of non-noble metals are compromised by lower intrinsic activities (lower turn-over frequencies). Amongst the single non-noble metal systems, copper-, cobalt-, manganese- and more recently chromium-based materials have attracted attention.[25,31,35,118-121] Cerium- or rather ceria-based materials have gained an enormous interest due to their high oxygen storage capacities as well,[31,122,123] being well-established in automobile catalysts promoting complete fuel oxidation and reduced NO_x emissions.[124]

With advancement over atomic scale syntheses, the formation of solid solutions enabled new chemical compounds with unique electron structures and improved thermal and chemical stabilities affecting the catalytic activity.[125] For instance, the so-called perovskite-type is responsible for an innumerable amount of publications considering catalytic combustion over the last three decades.[25,31,35,56,116,126] This type of mixed oxide solid solution with the general chemical formula ABX_3 carries two different cations A and B while X is the anion (mostly oxygen). A is cub-octahedrally surrounded by X, the cation B is coordinated by an octahedron of X, resulting in a large number of structural combinations which can be even expanded by partial substitution of the A and/or B cations with additional elements, leading to variations in the catalytic performance.[127,128] So far, the combination of lanthanum and strontium (A) together with copper, iron or manganese (B) revealed the highest activities for this type of mixed oxide solid solutions containing only non-noble metals.[126] One of the problems, which this type of solid solution deals with is the fact that perovskites tend to sinter quite easily, resulting in a decreased active surface area.[35]

To recapitulate this short review, in principle ruthenium and iridium show the highest bond-breaking capacity, as illustrated in **Figure 3.1**. Experimental and theoretical results indicate ruthenium to be among the best catalysts for steam and dry reforming. Binary systems such as the Ru-Pt supported on alumina are very active and robust against sulfur poisoning and coking. Mixed oxides such as the perovskite-type $La_{0.4}Ru_{0.6}Al_{0.2}Ni_{0.8}O_3$ combine the benefits of both

non-noble metals and ruthenium for highly active dry reforming catalysts. Pyrochlore-type mixed oxides containing ruthenium result in outstanding catalysts for the partial oxidation of methane to form syngas. A very recent catalyst screening revealed ruthenium to be the second-most active species after Rh for methane combustion. For iridium, on the other hand, hardly any studies can be found for catalytic methane conversion, however, very recent works revealed single-crystalline IrO_2 as a very efficient promoter for methane activation at low temperatures.[112] Unfortunately, the total oxidation capability of iridium seems quite poor as claimed by the recent catalyst screening reported by Kumsung et al.[110] which is in contrast to RuO_2, that is known to be an efficient oxidation catalyst.[129] Therefore, considering the high activity of ruthenium in oxidation reactions, the promising low-temperature activation of methane over $IrO_2(110)$ and the beneficial synergistic effects of mixed oxides, this work presents ruthenium-iridium mixed oxides ($Ru_xIr_{1-x}O_2$) as new candidates for the methane combustion reaction.

4. Ru$_x$Ir$_{1-x}$O$_2$ – Structure & Synergistic Interplay in Electrocatalysis

Both RuO$_2$ and IrO$_2$ adopt the rutile structure (shown in **Figure 4.1b),** which crystallizes in a tetragonal unit cell ($a=b\neq c$, $\alpha=\beta=\gamma=90°$) and belongs to the centrosymmetric point group 4/mmm (Hermann-Mauguin notation), alternatively D$_{4h}$ (Schoenfliess notation), and to the space group P4$_2$/mnm (No. 136).[130] The metal ions are octahedrally coordinated, forming MO$_6$-octahedra connected by edges (shown by blue line in **Figure 4.1a**). The six M-O bonds are not of equal length, resulting in a tetragonal distortion. The oxygen ions are surrounded by the metal ions in a planar and equilateral triangle (shown by green lines in **Figure 4.1a**). The oxygen-oxygen distances along the edges connecting the MO$_6$-octahedra are shorter compared to the remaining oxygen-oxygen distances as a result of the distortion.[131] The very similar ion radii of ruthenium (0.67 Å) and iridium (0.68 Å)[132] allow the intermixture of ruthenium dioxide and iridium dioxide at atomic scale forming ruthenium-iridium mixed oxides referred to as Ru$_x$Ir$_{1-x}$O$_2$, exemplary illustrated in **Figure 4.1c**.
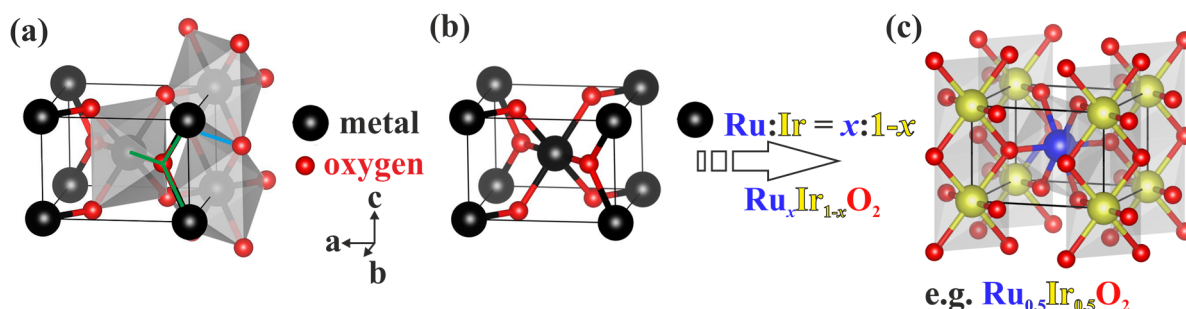
Figure 4.1: tetragonal unit cell (b) of the rutile structure showing the metal (Ru, Ir) ions with black balls and the oxygen with red balls. The MO$_6$-octahedra (a) are connected by edges (blue line) and are attached to a third MO$_6$-octahedron at the oxygen vertices in an equilateral triangle (green lines). Intermixing of ruthenium and iridium leads to the solid solution Ru$_x$Ir$_{1-x}$O$_2$ (c) adapting the rutile structure.

Mixed oxides in general are frequently used in heterogeneous catalysis in the hope to combine beneficial properties of the corresponding pure oxides.[133,134] For instance, oxides and mixed oxides including RuO$_2$, IrO$_2$, CeO$_2$, CeZrO$_2$, and CuCrO$_4$ have been shown to be efficient catalysts in the catalytic HCl oxidation reaction (Deacon process) to recover chlorine.[135-137] However, different from electrocatalysis, which has long since taken advantage of the benefits of ruthenium-iridium mixed oxides,[138-146] this material has not yet been considered for heterogeneously catalysed reactions. The harmonious interplay of ruthenium and iridium can be particularly realised in the oxygen evolution reaction (OER), which occurs for example in the electrochemical water splitting.[147] On the one hand, ruthenium dioxide is accepted as the most active electrocatalyst for OER, but on the other hand, it exhibits poor stability in both acid and alkaline media[148,149] with observable decomposition and dissolution of Ru$^{>4+}$ species

leading to a deactivation of the electrode material.[150] Few catalysts are able to resist the harsh and corrosive conditions present during OER in both acidic media ($2H_2O \rightarrow O_2 + 4H^+ + 4e^-$) and basic media ($4OH^- \rightarrow O_2 + 2H_2O + 4e^-$).[150] So far, only IrO_2 has shown the required longevity in operation[151,152] without being too inferior to ruthenium in terms of catalytic activity, however, iridium has a much lower abundance compared to ruthenium. Therefore, many works report attempts to combine the stability of iridium dioxide with the higher intrinsic activity and greater abundance of ruthenium (dioxide) without facing catalytic deterioration.[153-156] Kötz and Stucki, for instance, demonstrated the increased stability of ruthenium with small admixtures of iridium dioxide by the absence of any surface segregations during anodic oxygen evolution.[157] Both ruthenium and iridium showed uniform corrosion with a common corrosion rate equal to that of pure iridium dioxide. The formation of a solid solution with a single valence band spectrum thus is suggested here and IrO_2 is supposed to share electrons with RuO_2 preventing its oxidation to volatile Ru^{6+} and Ru^{8+} species and decomposition of the electrode.[157]

In addition to OER, ruthenium dioxide shows high activities for the hydrogen evolution reaction (HER) and chlorine evolution reaction (CER), which is why it has an excellent performance in the chlor-alkali electrolysis, where both HER and CER occur to produce H_2 and Cl_2.[158,159] The low stability of ruthenium dioxide is enhanced by TiO_2, which is considered inactive, to form so called dimensionally stable anodes (DSA).[138,155,160] Further improvement in selectivity, durability and economics is achieved by a ternary system, where iridium dioxide is added to form even more active and more stable DSA electrodes. This materials are promising catalysts for the electro-oxidative removal of long-chain phenolic compounds from industrial water waste, for instance.[161-163]

The deactivation of ruthenium-based materials in heterogeneous catalysis and in electrochemistry share the same origin, Ru^{4+} can be further oxidised to volatile and more soluble species. As one can learn from electrocatalysis, the concept of a mixed oxide containing iridium among others significantly improves the stability of ruthenium dioxide catalysts without losing activity. This work is inspired by the synergistic interplay of ruthenium and iridium, which has not yet been considered for the methane combustion reaction.

5.   Pechini Sol-Gel Route

The binary solid solution $Ru_xIr_{1-x}O_2$ can be prepared in different ways. Thin films are obtained by sputtering[157,164] or thermal decomposition[147] while powders are formed with hydrolysis routes[165] as well as the Adams fusion.[166] However, in order to establish structure versus activity correlations of the $Ru_xIr_{1-x}O_2$ powder catalysts, a high degree of structural control is required during synthesis. Unfortunately, the preparation of the ruthenium-iridium mixed oxide phases is non-trivial. Starting from the corresponding metal alloy will inevitably lead to the preferential oxidation of the metallic component with the higher oxygen affinity so that the composition of the resulting oxide is at least different from the prepared metal alloy and therefore the composition is less controlled. Additionally, the mixed Ru-Ir metal system reveals a pronounced miscibility gap[167] and post-oxidation may lead to an iridium-rich oxide that coexists with a ruthenium-rich oxide. Just co-precipitation methods are not sufficient, since the oxidation behavior of the metal precursors is different, so that the composition of the mixed oxide will not be well defined.

In this context, the Pechini method is a promising and powerful synthesis strategy to produce well-mixed solid solutions.[168-171] However, as mentioned, this method leads frequently to a metallic phase besides the desired mixed oxide so that the control of properties of the oxide particles may be aggravated.[172-175] The nature of the metallic phase and the question whether it contributes to the catalytic active surface need to be considered. Yet, the Pechini route allows for a statistical distribution of the metal cations in the solution and thus an intermixing at the atomic scale. This tends the formation of solid solutions rather than composites, which are not desired. This work aims at investigating synergistic effects on the intrinsic activity, which originate from an uniform structure with an unique valence band structure and varied metal-oxygen bond lengths and strengths, for instance. In case of composites, the observed catalytic activity is more likely a superposition of the activities of the individual oxides rather than a result based on synergistic effects.

The Pechini sol-gel method, named after Maggio Paul Pechini born in Pennsylvania in 1922, was originally developed to prepare lead and alkaline-earth titanates and niobates,[176,177] which are difficult to synthesize via hydrolysis methods because of the low solubility of the metal precursors and the unfavourable hydrolysis equilibria.[177] Over the last three decades, the original Pechini method has been modified and specified by varying the precursors, the solvents, as well as the reaction conditions to unlock a range of innovative materials. Mainly popularised by H. Anderson, who originally applied the synthesis to produce perovskite-type

materials for high-temperature magneto-hydrodynamic electrodes in the 1970s, the Pechini method and its modified variants nowadays are applied from laboratory to industrial scale with a great number of publications dealing with the preparation of superconducting, photocatalytic, magneto-optical and electrolytic materials.[177]

In a first step, an aqueous solution of the desired metal cations with readily soluble metal precursors is prepared. A carboxylic acid (or the corresponding carboxylate) such as citric acid is added to form coordination complexes. Citric acid is a polydentate ligand that bonds the metal atom twice with each oxygen atom of the carboxylic group. This so-called chelation forms more stable complexes, which is why the citric acid-metal complex is more stable than the alternative complexes that can form in solution with the present mono-dentate ligands such as water or chloride anions if, for example, chloride precursors are used. After chelation, the complex units are cross-linked by esterification of the remaining carboxylic groups of citric acid with ethylene glycol. Heating the reaction mixture evaporates the solvent (water) and further promotes cross-linking, resulting in a resin that is transferred to a crucible and calcined at temperatures typically between 500 °C and 900 °C for several hours to break down the carbon polymer and form the metal oxides.[178,179] **Figure 5.1** gives a general overview of the Pechini sol-gel synthesis route.
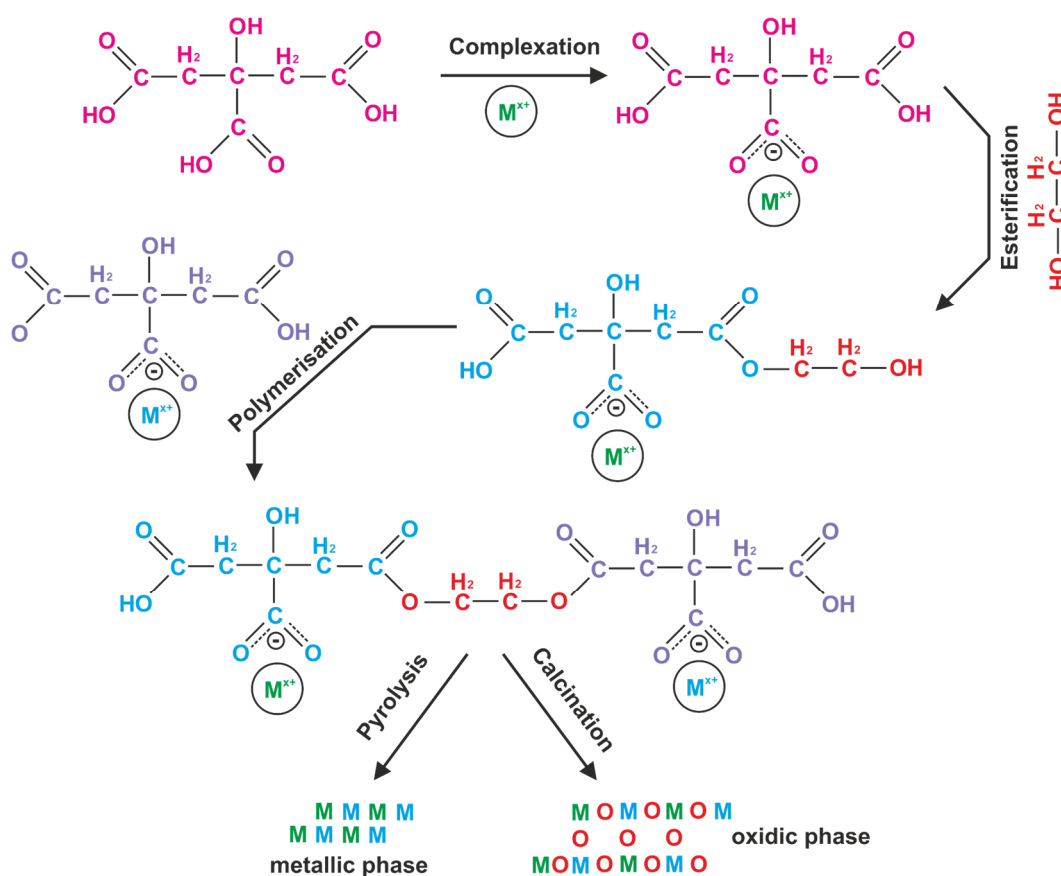
Figure 5.1: General overview of the Pechini sol-gel route including the complexation/chelation, the polymerisation and cross-linking followed by the pyrolysis or calcination to form the metal or oxide particles, respectively.

6. Characterization Techniques

6.1 Crystal Structure and Bulk Composition x

Ruthenium dioxide and iridium dioxide both adopt the tetragonal ($a=b\neq c$ & $\alpha=\beta=\gamma=90°$) rutile-type structure and have similar cation radii (Ru: 0.67 Å and Ir: 0.68 Å),[132] therefore similar unit cell parameters are expected. However, while the unit cell parameters a and b actually do not vary much, the unit cell parameters c differ significantly,[180] which is explained by crystal field effects due to the unequal amount of d-electrons in RuO_2 and IrO_2 leading to varied bond lengths and distortions in the MO_6-octahedra.[132] Due to the variation in c only, all d-spacings of planes parallel to the c-vector such as (110) are nearly equal between RuO_2 and IrO_2, whereas all d-values of planes with a Miller index l (hkl) other than zero such as (101) differ significantly. The phenomenon of a varying c parameter is advantageous for the analysis of the mixed oxides, since the d-spacing of (101) and the corresponding 2theta value correlate with the chemical composition x of $Ru_xIr_{1-x}O_2$ according to Vegard's law.[181] It states that the lattice parameter of a solid solution is given, to a first approximation, by the weighted mean of the corresponding lattice parameters of the two individual unary compounds.[153,181] **Figure 6.1** illustrates the physical principle of XRD analysis exemplified on the rutile (101) plane. Electromagnetic waves, in this case X-ray waves, are scattered by the symmetrically arranged electrons in the crystallographic rutile (101) plane, and according to Bragg's law the reradiated waves only experience constructive interference in certain directions.[182] The path length difference, an integer multiple of the wavelength of the electromagnetic wave, is constant for a certain, here rutile (101), reflection spot, which is why larger d-values ($d+\Delta d$) lead to smaller diffraction angles ($\theta+\Delta\theta$) to meet Bragg's law.

$$2d\cdot \sin(\theta) = 2(d+\Delta d)\cdot \sin(\theta+\Delta\theta) \qquad\qquad (6.1)$$

Like this, the 2theta value of the rutile (101) reflection of the mixed oxide is shifting depending on the unit cell parameter c. Since every measurement generally is accompanied with a 2theta shift originating from different specimen heights, the addition of LaB_6 (NIST) is required to correct the 2theta values in order to allow the use of Vegard's law without Rietveld refinement being necessary. For this work a "PANanalytic Empyrean" powder diffractometer is used with a θ-2θ (Bragg Brentano) geometry and a Cu Kα source (40 kV, 40 mA). The step size is 0.013° in 2θ and the scanning speed is about 0.8° min^{-1}.
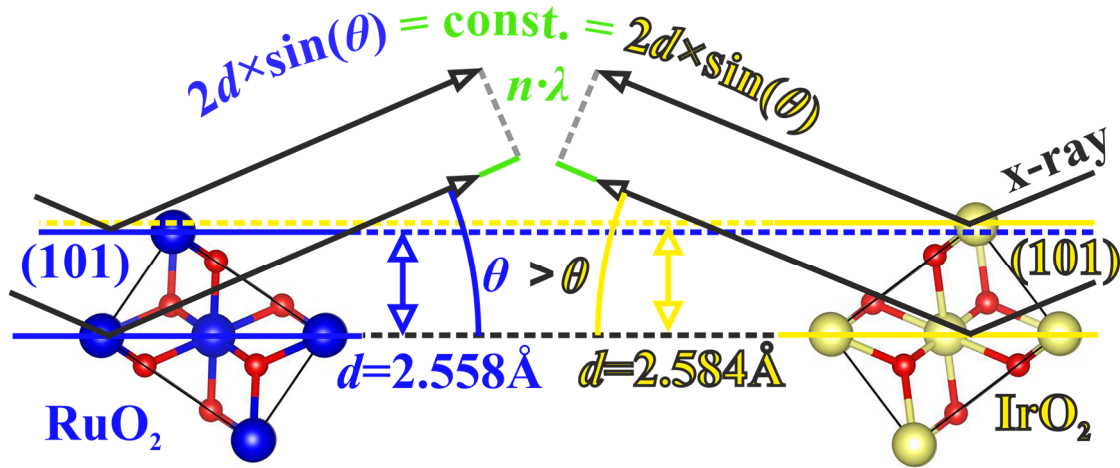
Figure 6.1: The principle of constructive diffraction exemplified with the rutile-(101) planes. The incoming X-ray beams are scattered spherically but only in directions where the path length difference (shown with a green line) is equal to an integer multiple of the wavelength λ (Bragg's law) a constructive interference occurs generating a reflection spot (Bragg-reflection) in the XRD pattern. RuO_2 and IrO_2 exhibit different d-spacings for the (101) plane and thus will give different 2theta values for this plane to meet the Bragg equation.

The successful intermixing of ruthenium and iridium on the atomic scale can also be studied via Raman spectroscopy by investigating the vibrational Raman active modes visualized in **Figure 6.2**.[183,184] The Raman-effect is based on the inelastic interaction of electrons of the material with the electric field of electromagnetic waves.[185,186] Light generates an electrical field E representing an electromagnetic and time dependent wave with E_0 being the maximum of the oscillation amplitude and v_0 the frequency of the electromagnetic wave. As soon as it interacts with a material, a polarisation P is induced with α being the polarizability factor depending on the material (**equation 6.2**).

$$P = \alpha \cdot E = \alpha \cdot E_0 \cdot \cos(2\pi v_0 t) \tag{6.2}$$

The polarizability factor can be approximated with a Tailor series for small vibrational displacements q with a two-terms approximation, α_0 being the polarizability factor around the equilibrium position and $(d\alpha/dq)_0$ being the polarizability change at a small deflection q around this equilibrium position. The polarization P induced during the interaction can then be described by **equation 6.3**, where the first term describes the elastic Rayleigh-scattering and the second term the sum of the inelastic Stokes and anti-Stokes scattering.

$$P = \alpha_0 \cdot E_0 \cdot \cos(2\pi v_0 t) + (d\alpha/dq)_0 \, q \cdot E_0 \cos(2\pi v_0 t) \tag{6.3}$$

Thus, if the change in polarizability while passing the equilibrium position is equal to zero, the selection rule is not met and the Raman-effect (inelastic scattering) cannot be observed. The

rutile type with the space group P4$_2$/mnm shows (**Figure 6.2**) four Raman active modes A$_{1g}$, B$_{1g}$, B$_{2g}$ and E$_g$.[183]
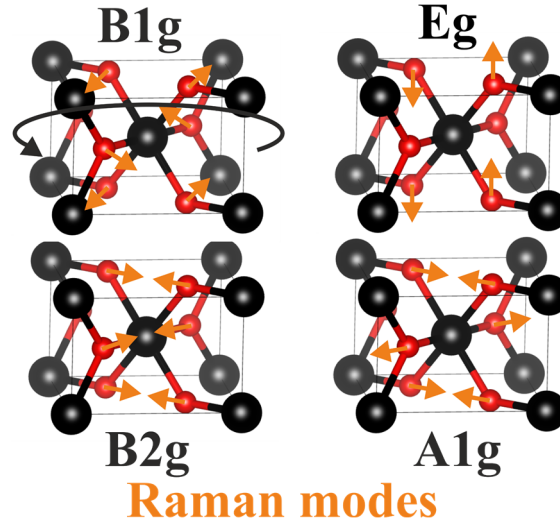
Figure 6.2: Raman active vibrational modes for rutile structure showing A1g, B1g, B2g and Eg mode. The B1$_g$ vibrational mode equals a rotation of the whole oxygen sublattice in the a-b-plane, which is why the energy transfer most probably is hampered and the signal may be too weak to be detected.

The inelastic scattering, accompanied by energetic interaction of the photon and the sample material, results in a change in the photon energy (with respect to the energy of the incident photons). The energy is transferred to vibrational energy of the Raman active modes in order to meet the energy conservation. If the Raman active vibrational modes are seen as classic springs subject to Hook's law with a force constant k and extended with the model of the harmonic approximation, the quantized vibrational energy levels E_n can be expressed by **equation 6.3**.

$$E_n = h \cdot v = (n + \frac{1}{2}) \cdot \frac{h}{2\pi} \cdot \sqrt{\frac{k}{\mu}} \qquad (6.3)$$

h = Planck constant

μ = reduced mass

v = frequency

The different bond strengths, electron densities, and unit cell parameters c among the various Ru$_x$Ir$_{1-x}$O$_2$ samples project different force constants k for A$_{1g}$, B$_{1g}$, B$_{2g}$, and E$_g$. Therefore, the energy levels differ between the samples. To conclude, the energy exchange ΔE (or $\Delta \tilde{v}$) of the photons and the ruthenium-iridium mixed oxides during inelastic scattering differ depending on the composition x. The signal of the B1g mode most probably may be too weak for detection

or may be overshadowed by the other, more dominant signals. The Raman spectra are recorded by using a "Senterra Raman microscope" from Bruker with a 632.8 nm laser as the excitation source. All samples are measured with a spectral resolution of 3-5 cm^{-1}, 20 co-addition, and 10 seconds integration time. The Raman spectra are measured in backscattering geometry at room temperature and processed with OPUS 7.5 software.

6.2 Surface Composition

X-ray photoelectron spectroscopy (XPS) is seen as most essential in this thesis, as it examines the catalytically important surface-near structure. XPS allows to determine the oxidation states of ruthenium and iridium as well as their relative concentration, mandatory to determine the composition x of $Ru_xIr_{1-x}O_2$ in both the supported and unsupported materials for an accurate interpretation of structure-activity relationship.

Kötz and Stucki reported that for a binary alloy system (Ru_xIr_{1-x}) there is a systematic composition-depending shift in the binding energies for both ruthenium (e.g. Ru 3d) and iridium (e.g. Ir 4f).[141] In another work, they also report that the binary oxides $Ru_xIr_{1-x}O_2$, on the other hand, show no shifts for the ruthenium and iridium signals but instead the binding energy of the oxygen (O 1s), interlinking and conveying the electron density of ruthenium and iridium, exhibits a systematic composition-dependent variation.[153,157,187] **Figure 6.3** illustrates the photoelectric effect and schematically shows the expected variation in the O 1s binding energies of the presented mixed oxides ($Ru_xIr_{1-x}O_2$).
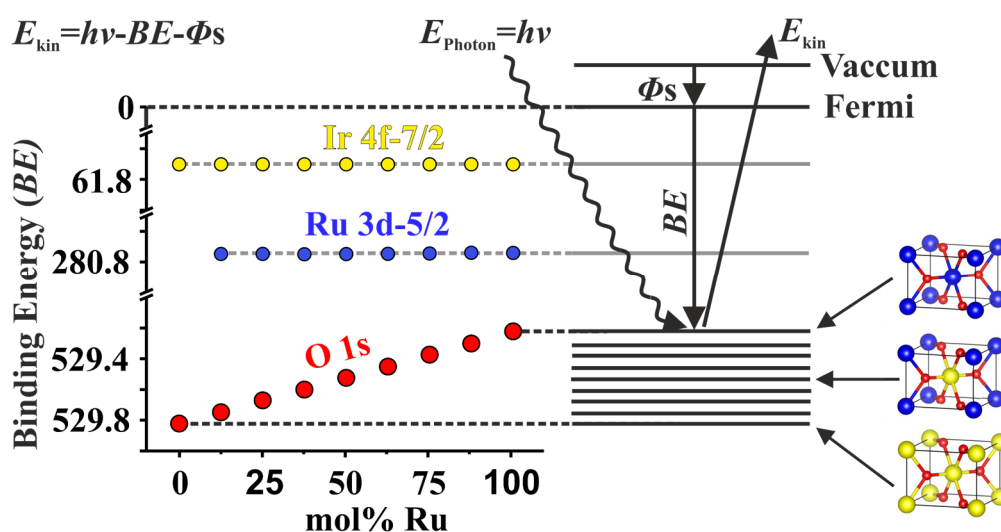
Figure 6.3: Schematic illustration of the photoelectric effect. The photon energy is adsorbed by an electron, whereby the binding energy of the electron is lower than the initial energy ($h\nu$) of the photon, which results in ejection of the electron with a residual kinetic energy E_{kin}. Detecting these emitted electrons and determining their kinetic energy, the binding energy, specific for elements and their valence states, can be calculated. Therefore, the wavelength of the incident X-ray beam as well as the work function Φ_S need to be known.

The XP spectra are recorded with a "PHI VersaProbe II". The photon energy for X-ray photoelectron spectroscopy is 1486.6 eV (monochromatized Al-K_α line), the X-ray spot size is ~200 µm with an excitation power of ~50 W. For overview spectra the pass energy is set to 58.7 eV and a step size is set to 0.5 eV, while the detail spectra are acquired with a pass energy of 23.5 eV and a step size of 0.2 eV. The system pressure during the experiment is ~10^{-6} Pa and all XPS spectra are recorded at room temperature. Deconvolution of the XP spectra is performed using the CASAXPS Version 2.3.17 software.

6.3 Number of Actives Sites, Dispersion and Surface Coverage

Employing XRD, Raman spectroscopy, and XPS, the successful preparation of unsupported ruthenium-iridium mixed oxides $Ru_xIr_{1-x}O_2$ with a single-phase rutile structure and high compositional control is questioned. For catalytic purposes, however, supported materials, referred to as $Ru_xIr_{1-x}O_2@TiO_2$, are prepared additionally in order to increase the dispersion and enhance thermal stability. Therefore, analyses of these supported materials need to be carried out to evaluate the dispersion of the active component and whether it is highly covering the carrier's surface, which is desirable for maximum noble metal utilization and thermal stability. In addition, the examination of the accessible active surface area is of utmost importance to enable a proper normalization of the kinetic and catalytic data such as the space time yield (further details on kinetic data are found in chapter 7). In case of unsupported materials, the active surface area, to first approximation, is proportional to the total surface area measured by physisorption experiments (BET method). The supported materials, however, need to be normalized exclusively to the active surface area of the active component but not to the support surface. With CO chemisorption experiments, the number of noble metal sites, given in mol per mass of catalyst, can be measured and may be referred to as number of active sites (*#a.s.*) given in $mol(\#a.s.) \cdot g_{cat}^{-1}$, which allows to calculate the dispersion (*D*) of the active component. However, a high dispersion or number of active sites is not equivalent to a high coverage of the carrier surface. The active component particles may occur as isolated agglomerates rather than highly dispersed on the support surface, therefore, additional examination is mandatory. XPS measurements are performed to determine the relative surface coverage *θ*. **Figure 6.4** illustrates how the number of active sites and the dispersion derived by CO chemisorption experiments as well as the surface coverage derived by XPS studies are calculated.

(a) CO chemisorption

(b) XPS

$\#a.s. = \text{mol(CO)} / \text{kg}_{cat}^{-1}$

$D = \text{mol(CO)} / \text{mol(Ru+Ir)}$

$\theta = (\text{at\%Ru}+\text{at\%Ir})\% / (\text{at\%Ru}+\text{at\%Ir}+\text{at\%Ti})\%$
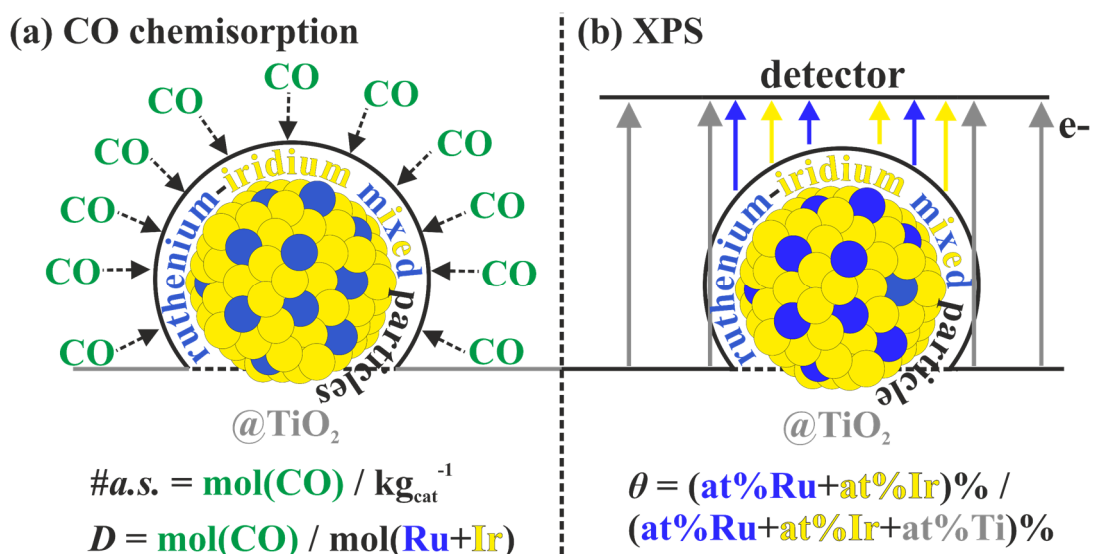
Figure 6.4: Graphical illustration of a) the CO chemisorption experiment for determining the number of active sites ($\#a.s.$) as well as the dispersion (D) and b) the XPS measurements for examining the coverage (θ) of the carrier material with the active component.

The CO chemisorption experiments (CO uptake experiments) are conducted in a home-built apparatus in order to determine the number of active sites provided by the active component of the ruthenium-iridium mixed oxide samples. The titration experiment quantifies the amount of accessible surface noble-metal atoms per gram catalyst according to the number of adsorbed CO molecules. With the approximation that each of the ruthenium/iridium sites is an active center for the methane conversion the number of active sites is equal to the number of adsorbed CO molecules. Even if this approximation of every metal site being an active center might not entirely be correct it still will provide the relative concentration of the number of actives sites between the different samples for a proper normalization of the catalytic STY (space time yield). Prior to the CO uptake experiments the samples are reduced for 20 h in a CO-stream at 350 °C; this pre-treatment is required since CO would otherwise partly reduce the oxide and be transformed to CO_2, thereby systematically overestimating the CO uptake. Subsequently, the surface is degassed in argon for 3 h at 350 °C. The CO concentration downstream is detected with a thermal conductivity detector (TCD). Well-separated CO-pulses are introduced until the CO signal in the TCD detector remains constant. The integral intensity of the final pulse serves as the reference signal. The integral difference signal between the reference signal and a measured CO-pulse corresponds to the amount of adsorbed CO during the pulse. The total CO uptake is determined by summing up all CO adsorption contributions from each pulse. Assuming that the CO-molecule adsorbs only on an active site the total amount of adsorbed CO corresponds to the total amount of active sites that can be normalized to the mass of used catalyst.

6.4 Supporting Characterization Techniques

With scanning electron microscopy (SEM), the morphology of the supported and unsupported materials is examined. Especially in the case of unsupported samples, where the Pechini method leads to xerogel-like porous networks, the questions of pore sizes (microporous and mesoporous materials) arises. Small pore sizes result in a strong increase in the total surface area, which in principle is beneficial for heterogeneous catalysis. However, the additional diffusion occurring in those pores may be rate limiting, therefore micropores (< 5 nm) are disfavoured. The porosity is investigated with a "Smart Merlin" SEM from Carl Zeiss. In addition, the mean composition of the unsupported $Ru_xIr_{1-x}O_2$ samples is determined by energy dispersive X-ray spectroscopy (EDS).

Transmission electron microscopy (TEM) is performed on a "Philipps CM30" instrument, operated at 300kV to investigate the particle size of both the carrier (TiO_2) and the active component ($Ru_xIr_{1-x}O_2$). The results are cross-checked with the dispersion D and surface coverage θ derived from the CO chemisorption experiments and the XPS results, respectively. The sample are ultrasonically suspended in isopropanol, and one or two droplets of the slurry are deposited on copper mesh grid afterwards.

For detailed structural, morphological and chemical analysis, a Cs probe-corrected Scanning Transmission electron microscope (STEM) "Jeol ARM 200 CF", operated at 80 kV and equipped with a cold-cathode field emission gun (FEG) electron source, is employed. A "Gatan Quantum ER" double electron energy loss spectroscopy (EELS) system and a "Jeol Centurio" energy dispersive X-ray spectrometer (EDS) with a 100 mm^2 silicon drift detector (SDD) are used for elemental analyses and mapping. The samples are directly transferred on a copper lacey-carbon coated grid.

In case of the unsupported material, the total surface is assumed to be proportional to the number of active noble-metal sites which is why Kr-physisorption experiments are performed to derive the specific surface area by applying the BET (Brunauer-Emmet-Teller) method. The measured specific surface area is referred to as *BET* surface area (short *BET*). The physisorption measurements are conducted with a "Autosorb iQ2" from Quantachrome Instruments. Kr-physisorption is about ten times more sensitive to the specific surface area than N_2 physisorption. While N_2-physisorption experiments need a total surface area of about 1 m^2, the Kr-physisorption experiments only need a total surface area of about 0.1 m^2. The samples are degassed in vacuum for 12 h at 120 °C before conducting Kr-physisorption experiments at 77 K. Even though the kinetic and catalytic data of the supported materials are not normalized to

the *BET* values, physisorption experiments are carried out for the supported samples too. Usefully, the *BET* values can be used to normalize the number of active sites to obtain the surface concentration of the number of active sites (#*a.s.*/*BET* given in mol·m^{-2}) for a pictorial image of the noble metal concentration at the surface.

Thermogravimetric analysis is conducted to determine the amount of crystal water in the used ruthenium and iridium precursors (RuCl$_3$·xH$_2$O and IrCl$_4$·xH$_2$O). In this work a "Setsys Evolution TGA" from Setaram is employed.

7. Homebuilt Flow Reactor & Process Management

7.1 Device Modules and Measured Quantities

The catalytic performance of the unsupported mixed oxides ($Ru_xIr_{1-x}O_2$) and the supported mixed oxides ($Ru_xIr_{1-x}O_2@TiO_2$) is investigated with a homebuilt flow reactor system, shown in **Figure 7.1** as a technical sketch. The reactor system allows to examine both the prototypical CO oxidation[188] as well as the methane combustion reaction.
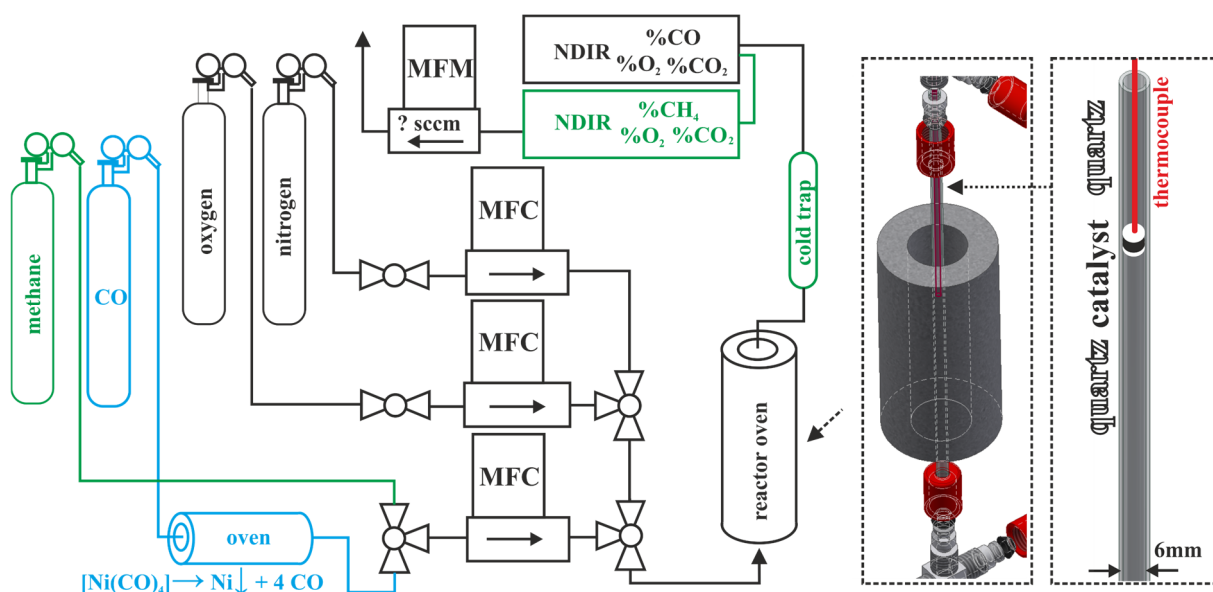
Figure 7.1: Technical sketch of the home-built flow reactor system for the prototypical CO oxidation reaction (blue components) and the methane combustion reaction (green components). The main components are mass flow controllers (MFC), which mix the desired gas composition consisting of CH_4, O_2 and N_2 for methane combustion and CO, O_2 and N_2 for CO oxidation. A quartz tube reactor, which is located vertically in a tubular furnace, contains the catalyst bed (1 to 2 nm thickness). A cold trap is installed to withdraw the water formed during reaction to protect the detectors. Nondispersive infrared sensors (NDIR) quantify the volumetric concentration of CH_4 and CO_2 for the methane combustion reaction and CO and CO_2 for the CO oxidation reaction. An electrochemical cell additionally quantifies the volumetric concentration of O_2. A mass flow meter (MFM) downstream measures the total gas flow required to determine the *STY* and to detect potential leaks. On the right side there are three-dimensional sketches of the oven and the reactor tube, indicating the catalyst bed and the separate glass tube (red stitch) with the thermocouple to measure the temperature in proximity to the catalyst bed.

The key parameter or quantity in this thesis, which is measured or rather calculated with the reactor systems shown in **Figure 7.1,** is the so called space time yield (*STY*). It defines the molar amount of product (here CO_2) produced per time and mass of catalyst ($mol(CO_2) \cdot kg_{cat}^{-1} \cdot h^{-1}$) and represents the quantitative performance of the whole reactor system. The space time yield also allows access to kinetic data such as the apparent activation energy and the reaction orders, as explained in chapter 7.4. The *STY* is determined by measuring the volumetric total flow rate $\dot{V}$, given in $ml \cdot min^{-1}$, with the mass flow meter (MFM) and the volumetric concentration of the

product ($Vol\%(CO_2)$) with the NDIR-sensor according to **equation 7.1**, where m_{cat} is the mass of catalyst given in kg and V_m the molar gas volume (ml·mol^{-1}).

$$STY \; (\text{mol}(CO_2) \cdot \text{kg}_{cat}^{-1} \cdot \text{h}^{-1}) = \frac{\dot{n}_{CO2}}{m_{cat}} = \frac{Vol\%(CO_2) \cdot \dot{V} \cdot 60 \cdot \text{min} \cdot \text{h}^{-1}}{m_{cat} \cdot V_m} \qquad (7.1)$$

7.1.1 Modules for Catalytic CO oxidation

The purities of used gases CO (Linde) and O_2 (NipponGases) are 4.7 and 4.0, respectively. The carrier gas nitrogen is produced by the Hampson-Linde cycle so that it must be dried and purified by a gas purifier prior to entering the mass flow system. A home-built copper trap-oven is installed prior to the mass flow controllers to thermally decompose potential metal carbonyl complexes formed in the CO-cylinder, most notably $Ni(CO)_4$. Otherwise, these metal carbonyls could decompose in the catalysts bed or along the entire reactor tube, thus adding Ni as an additional active component and therefore altering the detected catalytic activities.

The mass flow controllers (MFC, MKS Instruments 1179C) mix the desired reaction feed consisting of CO and O_2 balanced by N_2. MFC's are working based on the phenomenon of thermal dispersion, a physical property that is determined by the density and the heat capacity of a gas. The latter two quantities enter into the calculation of the so-called gas conversion factor. Thus, gases with identical gas conversion factors show same thermal dispersion if same volume flow rates are used. The flow rate is given in sccm (standard cubic centimetre per minute). Nitrogen was chosen as the calibration gas of the MFCs as well as the carrier gas since carbon monoxide and also oxygen have virtually the same gas conversion factor as nitrogen. This leads to smaller uncertainties in the actual volume flow rate since the mass flow controllers do not have to be adjusted and me be employed as calibrated.

The gas mixture is fed into the reactor that consists of a quartz tube with 6 mm inner diameter vertically placed in a "ThermConcept" tube furnace. The catalyst bed has been prepared by placing the pure sample (10mg to 30mg) on a 1mm thick layer of quartz sand in order to obtain a catalyst bed as flat as possible that is important for accurate kinetic data. Analogous, the catalyst material is covered with a 1 mm thick layer of quartz to prevent the nano-powder from carrying away downstream. The entire reactor is placed vertically in the oven to maintain a stable shape of catalyst bed during operation.

A nondispersive infrared sensor (NDIR) detects the volumetric CO concentration downstream to quantify the conversion $X=(Vol\%_0(CO)-Vol\%(CO))/Vol\%_0(CO)$ with $Vol\%_0(CO)$ being the

starting concentration and $Vol\%(CO)$ being the measured volumetric concentration of CO leaving the reactor. CO_2 is detected as well ($Vol\%(CO_2)$) to cross-check the accuracy of the determined conversion ($X=Vol\%(CO_2)/Vol\%_{max}(CO_2)$). The STY according to **equation 7.1** can be calculated considering that $Vol\%(CO_2)$ is equal to $Vol\%_{max}(CO_2)\cdot X$ where $Vol\%_{max}(CO_2)$ is the volumetric concentration of CO_2 at 100% conversion, a value which is determined in a preliminary experiment.

Finally, a mass flow meter is placed downstream the NDIR-sensor to quantify the actual volumetric flow rate ($\dot{V}_{total}$) required to calculate the space time yield according to **equation 7.1**. Besides, the flow meter is used to check for potential leaks along the gas lines, which would lead to lower volume flow rates and thus to higher contact times of the reaction mixture within the catalyst bed. The higher contact times in turn lead to higher conversion (X) values. Since the mass flow meter technically cannot distinguish between different gases, the welcome fact that the gases used during the CO oxidation experiments have the same gas conversion factor of one (CO, O_2 and N_2) and therefore no correction of the measured flow rate is required. However, this is different for the methane combustion experiments.

7.1.2 Reactor Modules for Catalytic Methane Combustion

The mass flow controllers (MFC, MKS Instruments 1179C) mix the desired reaction feed consisting of CH_4 and O_2 balanced by N_2. The purities of used gases CH_4 (Linde) and O_2 (NipponGases) are 4.5 and 4.0, respectively. A nondispersive infrared (NDIR)-sensor detects the volumetric concentration of C-H bonds giving the portion of CH_4 ($Vol\%(CH_4)$). The volumetric concentration of the product ($Vol\%(CO_2)$) is measured as well. Unlike during the CO oxidation experiment, where the conversion X and the STY are calculated by the measured volumetric concentration of CO and the volumetric concentration of CO_2 is only measured for cross-checking, during the methane combustion experiment the volumetric concentration of CO_2 is used to calculate the conversion according to $X=Vol\%(CO_2)/Vol\%_{max}(CO_2)$. This decision is based on the fact, that the NDIR sensor for CH_4 actually measures the amount of C-H bond and the formation of other hydrocarbons than methane, which form during reaction, may give faulty volumetric concentrations for CH_4. Therefore the $Vol\%(CH_4)$ is used for cross-checking purposes only.

As mentioned already, the MFCs employed are working based on the phenomenon of thermal dispersion, a physical property that is determined by the density and the heat capacity of a gas. The latter two quantities enter into the calculation of the so-called gas conversion factor. N_2

and O_2 have a gas conversion factor of 1.0 while methane has a gas conversion factor of 0.72. This needs to be considered and adjusted accordingly within the MFC device to have the correct reactant composition. The resulting volume flow rates $\dot{V}$ are given in sccm (standard cubic centimeters per minute) with reference conditions of 0 °C and 1 atm so that sccm actually is equal to $ml_n \cdot min^{-1}$ (milliliter normal per minute) even though the term "standard" and the term "normal" refer to different reference conditions originally.

The gas mixture is fed into the reactor that consists of a quartz tube with 6 mm inner diameter vertically placed in a "ThermConcept" tube furnace. The catalyst bed has been prepared by placing the pure sample (10mg to 30mg) on a 1mm thick layer of quartz sand in order to obtain a catalyst bed as flat as possible that is important for accurate kinetic data. Analogous the catalyst material is covered with a 1 mm thick layer of quartz to prevent the nano-powder from carrying away downstream. The entire reactor is placed vertically in the oven to maintain a stable shape of catalyst bed during operation. With a height of the catalyst bed of about 1.5 mm and a diameter of 6 mm the gas hourly space velocity is about $1.64 \cdot 10^5$ h^{-1} ($v_{GHSV=}\dot{V}/V_{catalyst\ bed}$) or 345.000 $ml \cdot g^{-1} \cdot h^{-1}$ ($v_{GHSV=}\dot{V}/m_{catalyst\ bed}$) if normalized to the average mass of catalyst.

A mass flow meter downstream the reactor measures the apparent total flow rate $\dot{V}_{total,apparent}$, which unfortunately, in case of the methane combustion experiment, is not equal to the actual $\dot{V}_{total}$. The latter is required to calculate the *STY* according to **equation 7.1**.

In the following the correction of the measured apparent total volume flow rate $\dot{V}_{apparent,total}$ is described. Since oxygen as the gas with the second highest share (8 *Vol%*) in the gas stream has virtually the same gas conversion factor as nitrogen (1.0), the measured volume flow rate at the mass flow meter will give reliable flow values independent of the nitrogen to oxygen ratio (which will vary while reaction). Unfortunately, the gas conversion factor of methane on the other hand is 0.72 and the conversion factor of CO_2, formed during reaction, is 0.7. Therefore, the mass flow meter downstream measures incorrect total volume flow rates ($\dot{V}_{apparent,total}$), which is different from the actual total volume flow rate $\dot{V}_{total}$. Besides, H_2O is formed and adsorbed by the cold trap so that the measured apparent total flow rate experiences an additional uncertainty. The actual total flow rate ($\dot{V}_{total}$) changes with conversion of the methane combustion reaction $CH_4+2O_2 \rightarrow CO_2+2H_2O$ and is given therefore by the equation $\dot{V}_{total}=\dot{V}_{total,0}-X \cdot 4sccm$. The 4 sccm reflect the maximum volume flow rate change from $X=0\%$ (with a gas composition downstream of 90 sccm N_2, 8 sccm O_2 and 2 sccm CH_4, thus 100 sccm) to $X=100\%$ (with a gas composition downstream of 90 sccm N_2, 4 sccm O_2 and 2 sccm CO_2,

thus 96 sccm). Due to potential leaks during operation, $\dot{V}_{total,0}$ is not necessarily equal to 100 sccm, which is why $\dot{V}_{total,0}$ is backcalculated at any time by $\dot{V}_{total,0}=\dot{V}_{apparent,total}+X\left|\Delta\dot{V}_{apparent,total}\right|$ where $\dot{V}_{apparent,total}$ is the measured apparent flow rate value given by the mass flow meter downstream. $\left|\Delta\dot{V}_{apparent,total}\right|$ reflects the maximum change in the by the MFM given apparent volume flow rate from $X=0\%$ to $X=100\%$ which can be determined in a preliminary experiment. Finally, $\dot{V}_{total}$ is equal to the expression $\dot{V}_{apparent,total}+X\cdot\left|\Delta\dot{V}_{apparent,total}\right|-X\cdot 4$ sccm. The $\dot{V}_{total}$ values determined this way are used to calculate the *STY* according to **equation 7.1**.

The space time yield, in the first instance, represents the performance of the overall reactor system rather than of the individual active sites of the catalyst material. To obtain kinetic data such as the apparent activation energy E_a several conditions need to be considered to equate the *STY* with the reaction rate of the surface reaction. The reaction must be controlled by micro-kinetics and the reactor has to be operated in a differential mode, both explained in the following chapter.

7.2 Micro-kinetics vs. Macro-kinetics

Before the reactants can interact on the catalyst surface (active sites), they must diffuse through the so-called boundary layer δ, which results from the reduced speed of the fluid elements above the surface due to viscosity (η).[189] This type of mass transport limitation is denoted as film diffusion and is associated to the macro-kinetics, referring to the entirety of heat and mass transfer processes in the reactor, which can be rate-determining. In this case, the measured *STY* is not representing the surface reaction including adsorption and desorption, denoted as the micro-kinetics. Note that for micro- and mesoporous materials additional mass transport limitation such as the Knudsen diffusion occur,[190] which is why for this work a non-porous carrier (rutile TiO_2 nanoparticles) is chosen, to exclude further macro-kinetic influences.

To reduce the influence of the film diffusion to a degree at which it has no influence on the overall reaction-rate, the dimension of the so-called boundary layer must be minimized in order to have sufficient supply of reactants at the surface and only the micro-kinetics contribute to the *STY*. Higher total volume flow rates $\dot{V}$ will lead to higher average gas velocities v_0 above the surface favouring a turbulent flow pattern, as described by the critical Reynolds-number, which defines the transformation of a laminar flow pattern towards a turbulent flow pattern.[191] With a turbulent flow the thickness of the (laminar) boundary layer δ_L experiences a sharp drop as schematically shown in **Figure 7.2** (blue line) and the diffusion rate perpendicular to the

catalysts surface increases according to Fick's law[192] ($v_D=-D(\Delta c/\Delta s)=-D(\Delta c/\Delta \delta_L)$), leaving the film diffusion less rate determining.

Preliminary experiments are conducted in this work to define the minimum total volume flow rate $\dot{V}$, which is suitable for the applied ruthenium-iridium materials to achieve micro-kinetic controlled data. Therefore, the *STY* is measured as a function of $\dot{V}$ with constant reactant concentrations and constant catalyst temperature. Starting with a low total flow of 50 sccm and stepwise adjustment of $\dot{V}$ to 90 sccm, a systematic increase of the *STY* is observed, which is due to the decreasing boundary layer and thus increasing mass transportation rates. A further increase of $\dot{V}$ above 90 sccm did not change the *STY* value anymore, which is a clear sign that the diffusion rate is not limiting anymore but the measured *STY* only depends on the micro-kinetics. Accordingly, 100 sccm (about 115 ml·min^{-1}) are chosen for the kinetic measurements in the methane combustion reaction. Too high volume flow rates, on the other hand, are disadvantageous since the catalyst bed is swirled and the accuracy of the NDIR sensor decreases too.
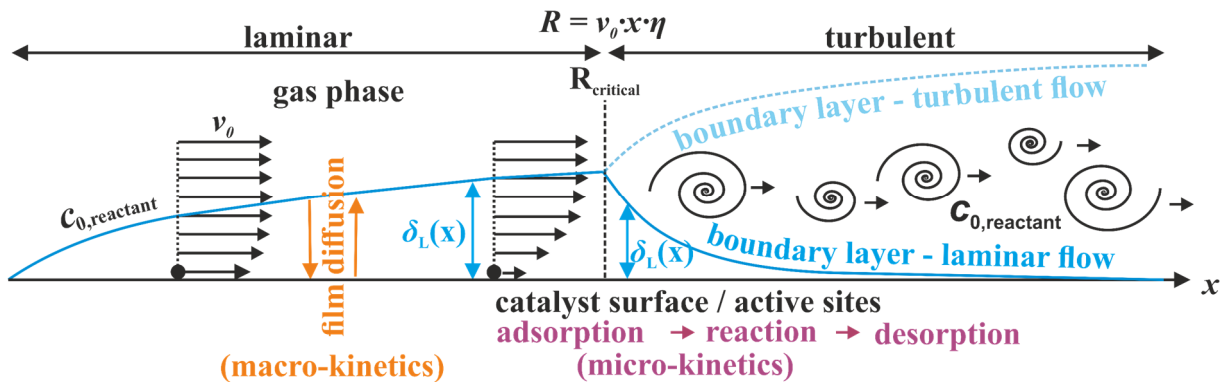
Figure 7.2: Illustration of the fluid dynamics above a non-porous surface. Depending on the thickness of the boundary layer, a result of the reduced velocities (red arrows) of gas molecules above the surface due to viscosity, either the surface reaction rate including adsorption and desorption (micro-kinetics) or the mass transport limitation rate (macro-kinetics) is limiting. High total volume flow rates $\dot{V}$ (proportional to the velocities v_0) favour a turbulent flow pattern (Reynolds number) and shrink the laminar boundary layer. This in turn will increase the diffusion rate according to Fick's law making it less rate-limiting. Note that the thickness of the overall boundary layer even increases with turbulent flow pattern along the *x*-axis, however, only the laminar fraction is crucial for the film diffusion since there is no concentration gradient in the turbulent boundary layer.

7.3 Differential Reactor

By considering an appropriate total flow rate, it is ensured that the micro-kinetics are rate-limiting. Nevertheless, additional conditions have to be met to ensure that the reaction rate of the surface reaction stays constant and does not vary along the catalyst bed. Furthermore, the contribution of any other reaction rates to the *STY*, originating from side reactions or product inhibitions, for instance, need to be prevented.

In a plug flow reactor (PFR) the reactant concentration is considered constant in radial direction (perpendicular to the reactor/tube axis) but changes along the reactor axis (axial direction) with no back-mixing occurring in axial direction.[193] The mass balance in a differential, small volume dV thus is maintained according to **equation 7.2**.

$$-d\dot{n}_{CO2} = -r' \cdot dV \tag{7.2}$$

The introduction of a differential conversion $dX_{CO2} = d\dot{n}_{CO2} \cdot \dot{n}_{CO2,max}^{-1}$ in the corresponding differential volume dV leads to **equation 7.3**.

$$d\dot{n}_{CO2} = -dX_{CO2} \cdot \dot{n}_{CO2,max} = -r' \cdot dV \tag{7.3}$$

The integration (**equation 7.4**) leads to the conversion achieved for a certain volume of catalyst (V_{cat})

$$\int_0^{Vcat} dV = \dot{n}_{CO2,max} \cdot \int_0^X \frac{dX_{CO2}}{-r'} = V_{cat} \tag{7.4}$$

Only if the conversion is low enough (<10%), the catalyst temperature and the reactant-concentrations (partial pressures) are nearly constant. This quasi-differential change allows the approximation of a constant reaction rate r' (**equation 7.5**).

$$\frac{V_{cat}}{\dot{n}_{CO2,max}} = \frac{1}{-r'} \cdot \int_0^X dX_{CO2} = \frac{1}{-r'} \cdot X_{CO2} \tag{7.5}$$

Finally (**equation 7.6**), the reaction rate is equal to $\dot{n}_{CO2} \cdot V_{cat}^{-1}$ or if multiplied with the density of the catalyst material to $\dot{n}_{CO2} \cdot m_{cat}^{-1}$, which is equal to the definition of *STY* (**equation 7.1**).

$$r' = \frac{-\dot{n}_{CO2,max} \cdot X_{CO2}}{V_{cat}} = \frac{\dot{n}_{CO2}}{V_{cat}} \sim \frac{\dot{n}_{CO2}}{m_{cat}} = r = STY \tag{7.6}$$

To conclude, the measured *STY* fortunately may represent the reaction rate of the micro-kinetic processes at the surface if the reactor runs in a differential way. Therefore, low conversions (2%

to 10%), small amounts of catalyst (10 mg to 30 mg) as well as high total volume flow rates ($\geq$100 sccm) are considered to meet the conditions, which allow to equate the *STY* with the catalytic performance of the entire number of active sites.

In case of the supported materials, the *STY* ($mol(CO_2)\cdot kg_{cat}^{-1}\cdot h^{-1}$) can be normalized to the number of active sites ($mol(\#a.s.)\cdot kg_{cat}^{-1}$), which de facto gives the commonly used turn-over frequency (*TOF* given in s^{-1}) defined as the number of turn-overs per time and per active site.[194] In this work, however, the normalized *STY* is not referred to as *TOF* for the simple reason that the CO-pulse experiments actually reveal the number of surface noble-metal sites, which may not be entirely equal to the number of active sites. This is why it is decided to stay with the more decent term "normalized *STY*" given in $mol(CO_2)\cdot mol(\#a.s.)^{-1}\cdot h^{-1}$.

7.4 Kinetic Data

In case that the *STY* sufficiently represents the surface reaction (micro-kinetics) including adsorption, surface reaction, and desorption, the following differential rate (**equation 7.7**) demonstrates how the apparent activation energy (E_a) and the reaction orders (e.g. *a* for methane and *b* for dioxygen) are connected to the measured *STY*.

$$STY = k\cdot[A]^a\cdot[B]^b = k_0\cdot\exp(-Ea/(RT)) \cdot [A]^a\cdot[B]^b = STY_0\cdot\exp(-Ea/(RT)) \qquad (7.7)$$

Actually, the determination of E_a requires knowledge of the reaction orders *a* and *b* in order to calculate *k* required for the Arrhenius plot ($\ln(k)$ vs. $1/T$). However, **equation 7.7** shows that one may obtain E_a simultaneously by an Arrhenius-like chart with $\ln(STY)$ as a function of $1/T$ leading to the same slope ($-E_a/(R\cdot T)$) and a pre-factor STY_0 ($k_0\cdot[A]^a\cdot[B]^b$) given by the y-axis intercept. Therefore, the *STY* is measured as a function of the catalyst temperature, referred to as light-off curves. Low activation energies are desirable in order to have sufficient activity at low temperatures, however, higher E_a values result in a more rapid increase in activity with higher temperatures. Highly active catalysts often show high activation energies which are compensated by high pre-exponential factors (k_0 or here STY_0) known as the Cremer-Constable-compensation.[195]

The examination of the reaction orders in methane and dioxygen is of great importance in this work since they partly contribute to the interpretation whether the dissociative adsorption and supply of monoatomic oxygen at the active site or the activation of methane (C-H bond) is hampered more and thus rate-limiting. The reaction order (e.g. for reactant A) is determined by varying the concentration of A ([A]) and detecting the change in the *STY*. The reaction order *a*

is then given by the slope $(\Delta\ln(STY)/\Delta\ln([A]))$ in a plot where $\ln(STY)$ is given as a function of $\ln([A])$ according to **equation 7.8**. The reaction order b is determined analogously.

$$\ln(STY) = \ln(k) + a\cdot\ln([A]) + b\cdot\ln([B]) = a\cdot\ln([A]) + C \qquad (7.8)$$

Recalling that low conversion is needed to achieve kinetic data of the considered surface reaction, the temperature for these reaction order experiments are chosen in a way that the conversion is about 10% only. That is why the temperatures differ among the various catalysts during these experiments. By choosing the same conversion, it is ensured that all catalysts have the same heat of reaction and similar micro- and macro-kinetic situations due to the similar gas phase and surface populations, which is considered more important than having same temperatures.

8. Experimental Results

Isotope labelling during methane chemisorption experiments revealed a mechanism roughly valid for all noble metal catalysts, with initial formation of methyl and methylene species, which further interact with the adsorbed oxygen and either directly form CO_2 and water or first lead to the formation of CO and H via the formaldehyde route.[25,196-198] **Figure 8.1** is giving a rough overview of the catalytic methane combustion (CMC) pathways.
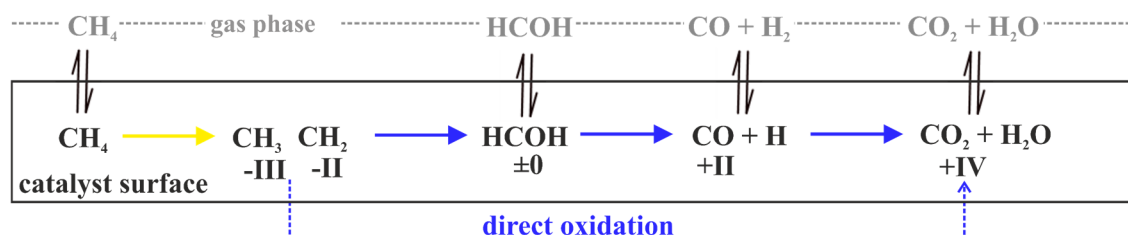
Figure 8.1: Reaction pathway of the methane combustion revealed by isotope labelling.[25] In the initial step, a rupture of the C-H bond takes place ("methane activation") followed by either direct oxidation of methyl and methylene to CO_2 or a stepwise oxidation to formaldehyde and carbon monoxide first.

The reaction pathway is split into an initial activation of the C-H bond, marked with a yellow reaction arrow in **Figure 8.1**, succeeded by oxidation steps (blue arrows). The ruthenium-iridium mixed oxides are presumed to be efficient catalysts combining the high catalytic activity of ruthenium for oxidation reactions[199] with the promising, recently reported, low temperature C-H activation over IrO_2.[112,113,200] Therefore, this work additionally examines the ruthenium-iridium mixed oxides during catalytic CO oxidation prior to applying them to the methane combustion reaction in order to achieve a better catalytic understanding of the presented catalysts and to assess the roles of ruthenium and iridium in the reaction pathway (**Figure 8.1**).

The following chapter 8.1 contains exhaustive results from characterization of the unsupported ruthenium-iridium mixed oxides. In addition, first catalytic performances during prototypical CO oxidation are presented. This chapter contains results previously published in the *Journal of Physical Chemistry C* (O. Khalid, T. Weber, G. Drazic, I. Djerdj and H. Over, *Journal of Physical Chemistry C*, 2020, 124, 18670-18683.). The chapter after next (chapter 8.2) is concerned with the synthesis and characterization of the supported (@TiO_2) $Ru_xIr_{1-x}O_2$ samples. Furthermore, both supported and unsupported materials are applied to the methane combustion reaction. In chapter 8.3, the reaction scheme developed on the basis of the characterization as well as the main catalytic results from catalytic CO oxidation and catalytic methane combustion are recapitulated at a glance.

8.1 Ru$_x$Ir$_{1-x}$O$_2$ Applied to CO Oxidation

8.1.1 Synthesis

The unsupported mixed ruthenium-iridium powder samples, prepared by the Pechini method[176] (**Figure 5.1**), are referred to as Ru_x with x being the nominal composition of ruthenium in mol% changing from 0 mol% to 100 mol% in steps of 12.5 mol% (pure iridium sample is referred to Ir_100 instead Ru_0). This special variant of sol-gel synthesis guarantees an immobilization of the metal cations by chelation with the carboxylate group of the citric acid and subsequent polymerization by glycol. Therefore, this robust synthesis strategy allows to mix the ruthenium- and iridium- cations at atomic scale, leading to the desired solid solution composition in the reaction mixture throughout the entire synthesis. The final calcination step results in the (mixed) oxide phase with the desired composition besides a (mixed) metallic phase.

The preparation of Ru_x with a nominal composition of x=50 mol% is exemplified: 0.5 mmol of RuCl$_3$·3.5H$_2$O and 0.5 mmol of IrCl$_4$·H$_2$O are dissolved in water. Subsequently, 50 mmol of anhydrous citric acid are added to the solution, the mixture is stirred for 30 min to ensure complete dissolution of the acid and then is mildly heated to 60 °C to accomplish the complete complexation of the metal cations. Afterwards 150 mmol ethylene glycol are added and the solution is heated to 100 °C with maximum heating power to induce sudden polymerization/ polycondensation. As soon as most of the solvent is evaporated, the resulting black resin is transferred to a crucible and is committed to a high temperature treatment at 450 °C for 7 hours with a heating rate of 1 K·min^{-1} under atmospheric condition. The obtained mixed ruthenium-iridium powders are grinded for the analytics and catalysis experiments.

8.1.2 Characterization of Ru$_x$Ir$_{1-x}$O$_2$

Experimental X-ray diffraction patterns of the ruthenium-iridium mixed samples (Ru_x) for various nominal compositions x (as derived from the ratios of the used metal precursors) are collected in **Figure 8.2**, focusing on two specific regions where once the mixed oxide phase dominates (**Figure 8.2a**) and a second region where the metallic phase is most prominently seen (**Figure 8.2b**).

All reflections in the XRD patterns can be explained by the superposition of a rutile structure and two metallic phases with fcc and hcp structure. For the pure iridium sample (Ir_100), the

coexistence of rutile $IrO_2(110)$ and fcc-Ir is observed, while for the pure ruthenium sample (Ru_100) rutile RuO_2 and hcp-Ru are formed. The coexistence of oxide and metal, as mentioned in chapter 5, is known as a shortcoming of the Pechini method.[172-174]

When adding small amounts of ruthenium to iridium, the rutile oxide structure is hardly affected, while the metal phase remains in the fcc structure for x=12.5 mol% of ruthenium; no hcp structure is discernible in XRD. The diffraction peaks of fcc shifts slightly with the metallic Ru concentration, consistent with the formation of a Ir-rich fcc metal alloy. The formation of alloys for the mixed metallic Ru-Ir system was recently decribed.[201] When the ruthenium content is further increased the hcp phase appears as well in the range x=25 mol% up to 62.5 mol%. Beyond a nominal composition of x=62.5 mol%, the metal phase appears only as hcp structure. The diffraction peaks of the hcp structure shifts slightly with the ruthenium concentration, consistent with the formation of a Ru-rich hcp metal alloy. In the region of x=25 mol% to 62.5 mol% the positions of diffraction peaks of the coexisting fcc and hcp structures do not vary. This behavior of the metallic phase is indicative of a miscibility gap that is also expected from the different structures of pure metallic Ru (hcp) and pure metallic Ir (fcc). The miscibility gap is experimentally observed at least for x=25 mol% up to 62.5 mol%. In the miscibility gap the compositions of the of Ir-rich fcc metal phase and the Ru-rich hcp metal phase are invariant, implying that also the structure is fixed as observed in XRD (**Figure 8.2b, right**).
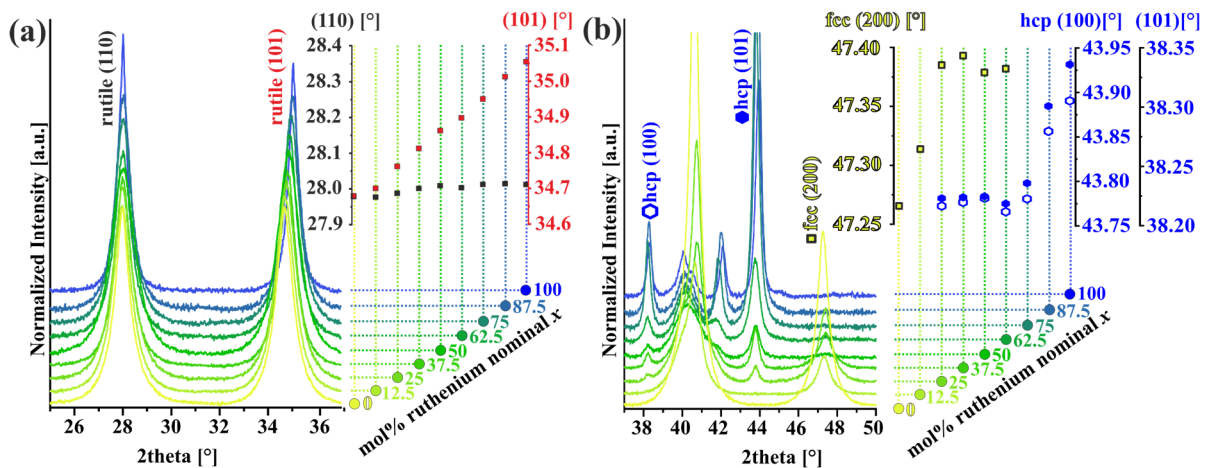
Figure 8.2: Experimental X-ray diffraction patterns of the mixed ruthenium-iridium powder samples are shown for various nominal compositions x given in mol% of ruthenium, focusing on two regions where once the mixed oxide phase is dominating (a) and the other region where the metal phase is most prominently seen (b). The mixed oxide phase (a) is represented by strong rutile (110) and rutile (101) reflections, and two metallic phases (b) are characterized by the hcp (100), hcp (101) and fcc (200) reflections.

Quite in contrast, the diffraction peaks of the rutile phase shift continuously from that of IrO_2 to that of RuO_2, (**Figure 8.2a, right**) when the nominal composition is varied from $x=0$ mol% to 100 mol%, evidencing that there is no miscibility gap for the corresponding mixed $Ru_xIr_{1-x}O_2$ oxides; recalling both pure oxides, RuO_2 and IrO_2, crystallize in the rutile structure. The oxide phase constitutes a solid solution throughout the full composition range x, only slightly changing the lattice unit cell, namely the c values. Actually only the rutile (101) peak continuously shifts with the nominal composition x.

These XRD data are subject to systematic Rietveld refinements, assuming that the mixed oxide phase crystallizes always in the rutile structure and the mixed metal phase crystallizes in the fcc structure for Ir-rich alloys and in the hcp structure for Ru-rich alloys with negligible stacking fault concentration. In the composition range, roughly from $x=25$ mol% up to 62.5 mol%, the mixed Ru-Ir metal system reveals a miscibility gap whose exact boundary concentration can be determined with Rietveld analysis, when besides the lattice constants also the intensities are considered. The actual molar composition of the solid solution (rutile oxide) and that of the hcp and fcc metal alloys as well as the phase composition in weight%, the lattice constants, and the averaged crystal size can be derived from Rietveld refinement. The boundary compositions of the miscibility gap in the metal phase turn out to be $x=21$ mol% and 74 mol%. The optimized parameters of Rietveld refinement for prepared ruthenium-iridium mixed powders with various nominal compositions x are compiled in **Table 8.1**.

Table 8.1: Rietveld Refinement data of the mixed ruthenium-iridium powder samples, including chemical formula, phase composition in weight% (*wt%*), average crystallite size (*av. c. size*), and lattice parameters of both oxide (rutile) and metallic (hcp and fcc) phases.

	Ir_100	Ru_12.5	Ru_25	Ru_37.5	Ru_50	Ru_62.5	Ru_75	Ru_87.5	Ru_100
actual comp. *rutile phase*	0	0.16	0.28	0.36	0.53	0.60	0.75	0.87	1
a,b [nm]	4.506	4.507	4.505	4.503	4.502	4.502	4.501	4.501	4.501
c [nm]	3.155	3.152	3.147	3.139	3.133	3.128	3.122	3.114	3.108
av. c. size [nm]	6.2	5.9	5.6	6.9	4.9	6.8	6.5	7.8	13
wt%	51.3	82.6	70.5	74.2	90.1	80.2	72.7	69.0	74.7
actual comp. *hcp phase*	-	-	0.74	0.74	0.75	0.74	0.75	0.90	1
a,b [nm]	-	-	2.712	2.717	2.718	2.717	2.717	2.713	2.711
c [nm]	-	-	4.317	4.317	4.319	4.317	4.312	4.297	4.287
av. c. size [nm]	-	-	9.0	12	9.3	10.4	17	19	24
wt%	-	-	2.85	7.05	5.52	14.7	27.31		
actual comp. *fcc phase*	0	0.13	0.19	0.20	0.24	0.21	-	-	-
a,b,c [nm]	3.843	3.840	3.834	3.834	3.834	3.834	-	-	-
av. c. size [nm]	10	9.1	8.8	8.1	4.9	4.3	-	-	-
wt%	48.7	17,4	26.6	18.8	4.37	5.17	-	-	-

The main results of the Rietveld refinements of the mixed oxide phase are summarized graphically in **Figure 8.3**. While the lattice constant a and b of rutile do practically not vary with the composition, the c parameter changes linearly with the composition as expected from Vegard's rule (**Figure 8.3a**).[181] The continuous shift in unit cell parameter c in case of rutile oxide phase indicates mixing at the atomic scale throughout the whole composition range. The composition of the mixed oxide is shown in **Figure 8.3b**, clearly indicating a linear correlation between the nominal composition x and the actual composition derived from Rietveld refinement.
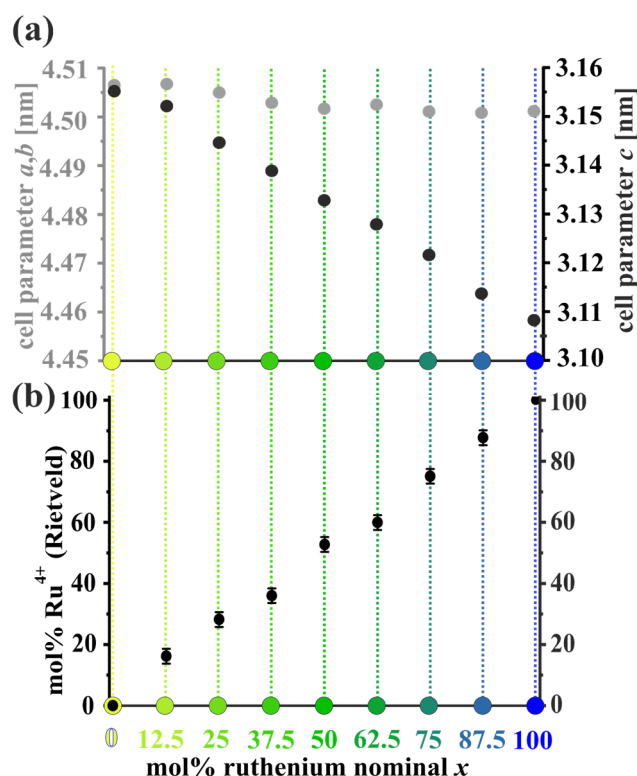
Figure 8.3: Lattice parameters for the rutile phase (a) as a function of the nominal composition x given in mol% of ruthenium as determined by Rietveld refinement. Continuous shift in unit cell parameter c in case of rutile oxide phase indicates mixing at atomic scale throughout the whole composition range. (b) Rietveld-determined composition as a function of the nominal composition x.

In **Figure 8.4**, the Rietveld results for the metallic phases are summarized too. Also the lattice parameters for the Ru-rich hcp metal phase and the Ir-rich fcc metal phase (**Figure 8.4a**) indicate clearly the miscibility gap by their invariant values. The miscibility gap becomes even clearer in the actual compositions of the fcc and hcp phases shown in **Figure 8.4b**. The molar fraction of Ru of the Ru-rich hcp phase and the Ir-rich fcc phase are constant in the nominal composition range x=25 mol% up to 62.5 mol% as expected for a miscibility gap.
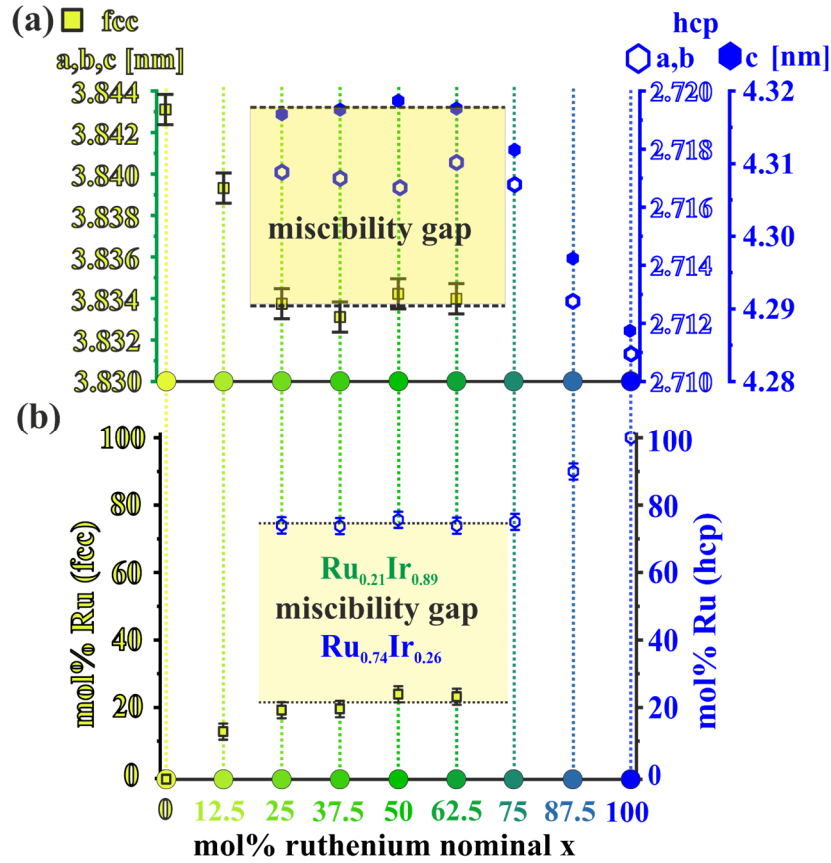
Figure 8.4: Lattice parameters of the Ir-rich fcc and the Ru-rich hcp metallic phases (a) as a function of the nominal composition x given in mol% of ruthenium. (b) Rietveld-determined composition of the Ir-rich fcc and the Ru-rich hcp metallic phases as a function of the nominal composition x.

With Raman spectroscopy (**Figure 8.5**) the non-existence of a miscibility gap of the $Ru_xIr_{1-x}O_2$ is reinforced. The oxide phases can be followed with Raman (although Raman intensities are low due to the metallic character of the oxides) as a function of the nominal composition x. Starting from the pure IrO_2 sample, two Raman active modes are observed, namely E_g and B_{2g} at 550 cm^{-1} and 730 cm^{-1}, respectively. With increasing amount of intermixed ruthenium these modes shift slightly towards lower wavenumbers. Above x=25 mol% the B_{2g} band broadens and another mode (A_{1g}) emerges above 37.5 mol%. These three phonon modes shift with increasing x up to the Raman spectrum of pure RuO_2. Since the Raman spectra continuously vary with the composition x it is concluded that the oxides are solid solutions. In case, the mixed oxides consist of a superposition of RuO_2 and IrO_2, one would expect a superposition of both Raman spectra, however, that is not observed in **Figure 8.5**. For the pure oxide phases RuO_2 and IrO_2[202,203] and for some of the mixed oxides[184] the presented Raman spectra are consistent with those found in literature.

Surprisingly, even the Raman spectra provide some, albeit indirect evidence for the miscibility gap of the metal phase. When the molar stoichiometry is changing from x=12.5 mol% to

25 mol%, the B$_{2g}$ starts to broaden. This is not observed for the variation of x from 0 mol% to 12.5 mol%. Here, only the B$_{2g}$ mode is shifting to lower wavenumbers. On the other side of the miscibility gap, with the change of nominal composition from x=62.5 mol% to 75 mol%, a sudden shift and a well separated Raman A$_{1g}$ mode appear.

Altogether, both XRD and Raman spectroscopy clearly indicate that the mixed Ru$_x$Ir$_{1-x}$O$_2$ oxide phase is not facing a miscibility gap throughout the whole composition range. Secondly, the metal phase reveals a miscibility gap for 75 mol% > x > 25 mol% and only for x < 25 mol% and x > 75 mol% metal alloys in fcc (Ir-rich) and hcp (Ru-rich) structures, respectively, are found to form.
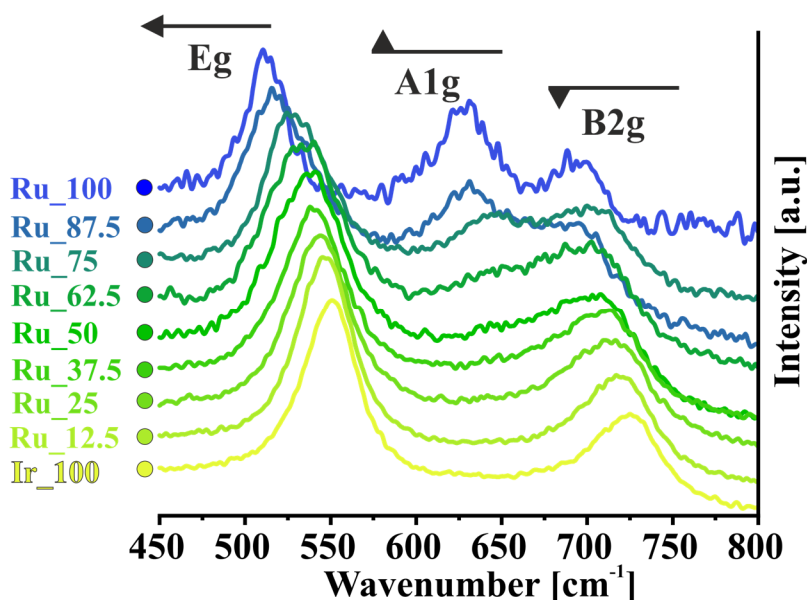
Figure 8.5: Raman spectra of mixed ruthenium-iridium powders for various nominal compositions x (referred to as Ru_x). Raman spectra show vibrational modes E$_g$, A$_{1g}$ and B$_{2g}$, all belonging to the rutile oxide phase. Vibrational modes E$_g$ and B$_{2g}$ experience continuous shifts to lower wavenumbers with increasing Ru^{4+} concentration in the unit cell.

With XPS the actual surface compositions of the mixed ruthenium-iridium powders (Ru_x) for varying nominal composition x (**Figure 8.6**) are investigated. From the Ru 3d spectra it can be clearly seen that ruthenium is always in the Ru^{4+} oxidation state, i.e., RuO$_2$, with no signature of metallic Ru. Already from this series of Ru 3d spectra the conclusion is made that the metallic phase is obviously encapsulated by the oxide phase for all nominal compositions x. In addition, the binding energies of Ru 3d$_{5/2}$ and Ru 3d$_{3/2}$ do not vary with the composition meaning that there is no additional charge transfer between Ru^{4+} and Ir^{4+} in the mixed oxide phase.[204]
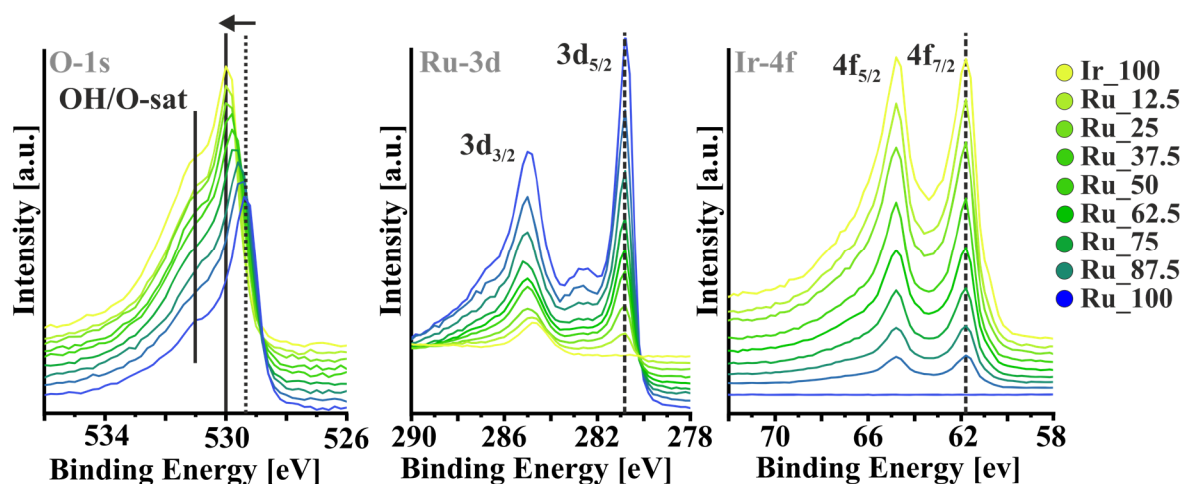
Figure 8.6: XPS spectra of Ir 4f, Ru 3d and O 1s signals of the mixed ruthenium-iridium powder samples as prepared. While the Ir 4f and Ru 3d peaks show unchanged binding energies, the main peak of O 1s shifts continuously to lower binding energies with the ruthenium content.

From the Ir 4f spectra as function of the nominal composition x similar conclusions can be drawn: The binding energies of the dominating emissions (Ir $4f_{7/2}$ and Ir $4f_{5/2}$) are fully consistent with Ir^{4+} and do not vary in the binding energy with the composition. As seen later when fitting quantitatively the XPS data, there is a small metallic Ir component present in the Ir 4f spectrum.

The O 1s spectra indicate two components, one is ascribed to O^{2-} of the oxide and the other is either assigned to OH or to a satellite structure O-sat as proposed in the literature.[205] The binding energy the O^{2-} component linearly shifts from 529.4 eV to 530.0 eV, when the nominal composition is varied from $x=0$ mol% to 100 mol%, respectively. This shift of O^{2-} in the O 1s spectra may be attributed to higher electron density at O^{2-} in the case of RuO$_2$ in comparison to that of IrO$_2$, and can be utilized to define the actual composition in the mixed oxide (**Figure 8.7**). The additional O 1s peak (OH/O-satellite) at the high energy flank does not shift with the nominal composition x. Surprisingly, neither the binding energies of Ir 4f nor that of Ru 3d shift with the composition x. Significant shifts are reported in metallic alloys such as PdAg.[206-208] However, in mixed metal oxides the different metal cations are not directly but rather coordinated via an O species and according to Kötz and Stucki[153,157] this explains why the O 1s binding energy of O^{2-} does shift with composition x, while those of the metal core levels do not.
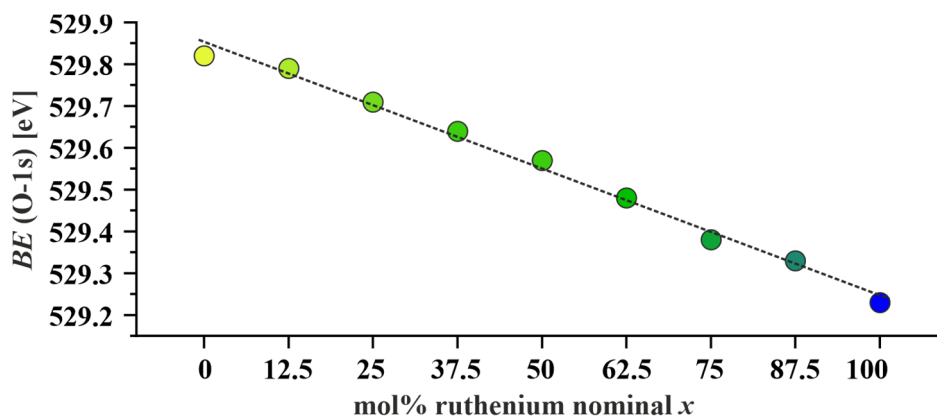
Figure 8.7: Binding energy shift of the O^{2-} component in O 1s spectra of mixed Ru$_x$Ir$_{1-x}$O$_2$ as a function of the composition x.

In **Figure 8.8** the deconvolution for Ru_50 sample of O 1s, Ru 3d and Ir 4f into various components exemplarily is depicted. For O 1s the dominating peak is bulk O^{2-} and in addition there is a component at the high energy flank that can be ascribed to OH or to the satellite (O-sat). For Ru 3d there are three components, one spin orbit split pair related to bulk coordinated Ru^{4+} in rutile structure (280.8/284.9 eV), a spin orbit split pair due to the satellite at (282.5/286.7 eV)[209] and finally the C 1s (284.5 eV) that is ascribed to C in the zero valence state. The C 1s peak is assumed to be due to residual carbon from the Pechini synthesis or also due to carbon from the atmosphere covering the sample during transfer. The Ir 4f region shows a spin-orbit pair for minor metallic Ir species at 60.9/63.9 eV besides the dominant pair of peaks for the Ir^{4+} at 61.7/64.7 eV. Deconvolution of the remaining samples are compiled in **Figure 8.9** and the fitting parameters are collected in **Table 8.2**.
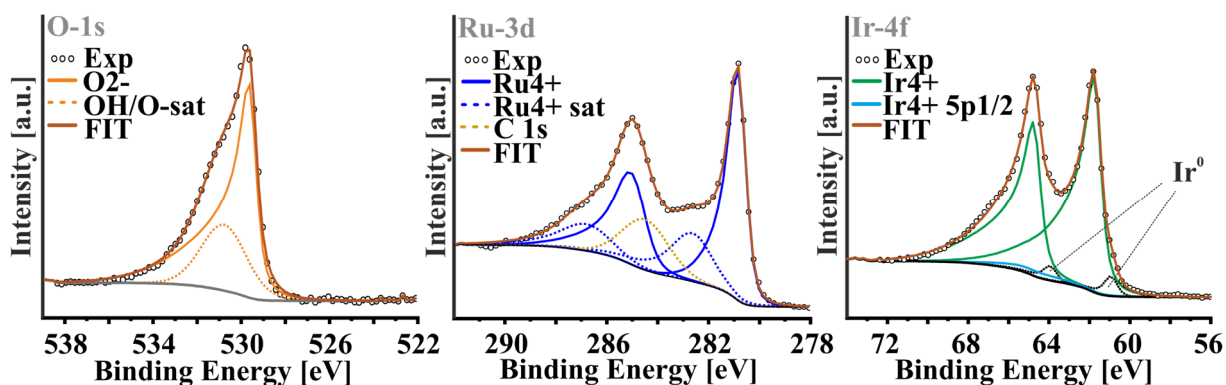
Figure 8.8: Fitting of the Ru 3d-, the O 1s- and the Ir 4f- spectra of the Ru_50 sample. The main components are bulk O^{2-}, Ru^{4+} and Ir^{4+}. There are additional components in spectra: OH or O-satellite in the O 1s, Ru^{4+} satellite and C 1s in Ru 3d, and metallic Ir^0 and 5p1/2 of Ir^{4+} in Ir 4f.
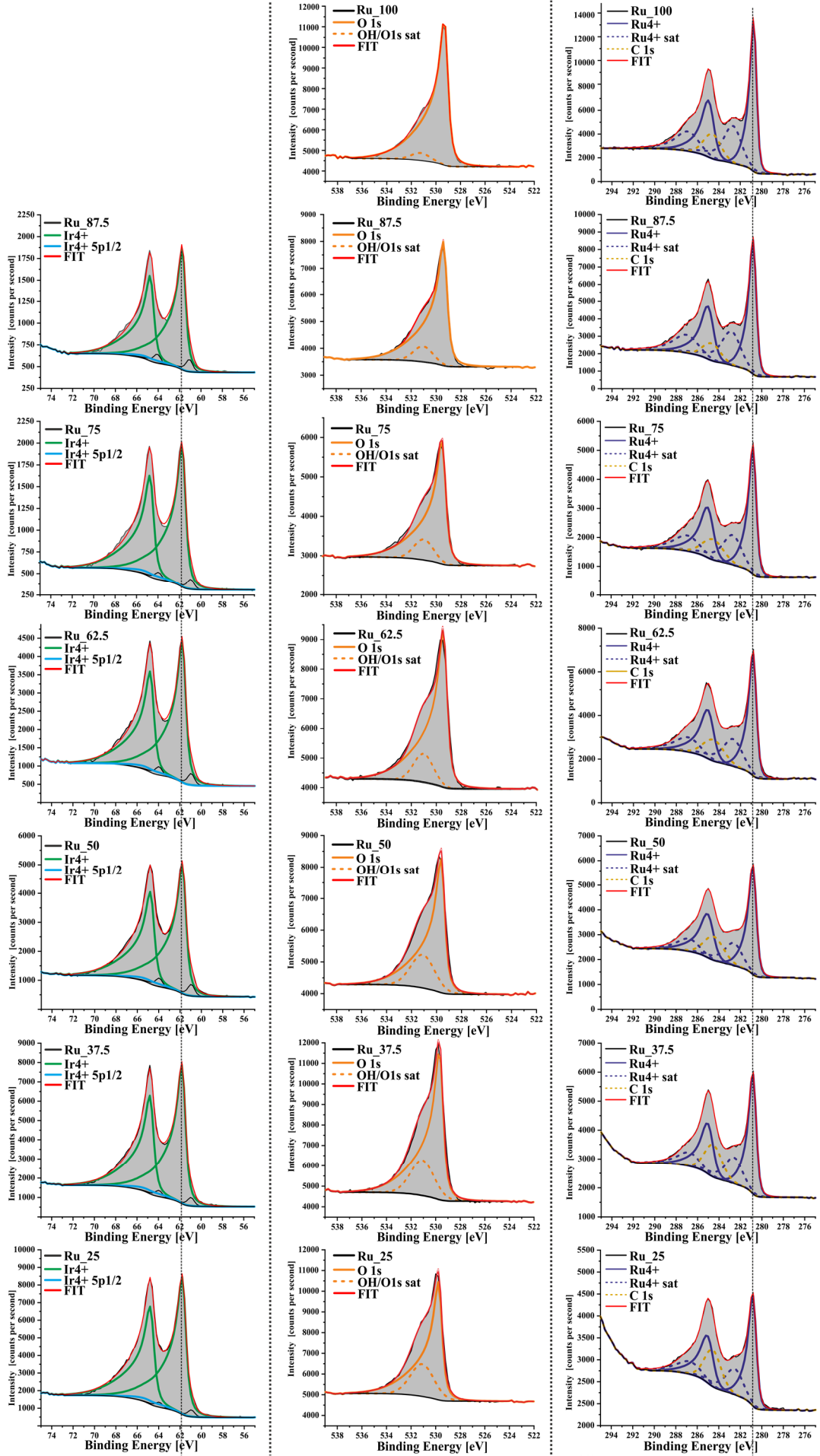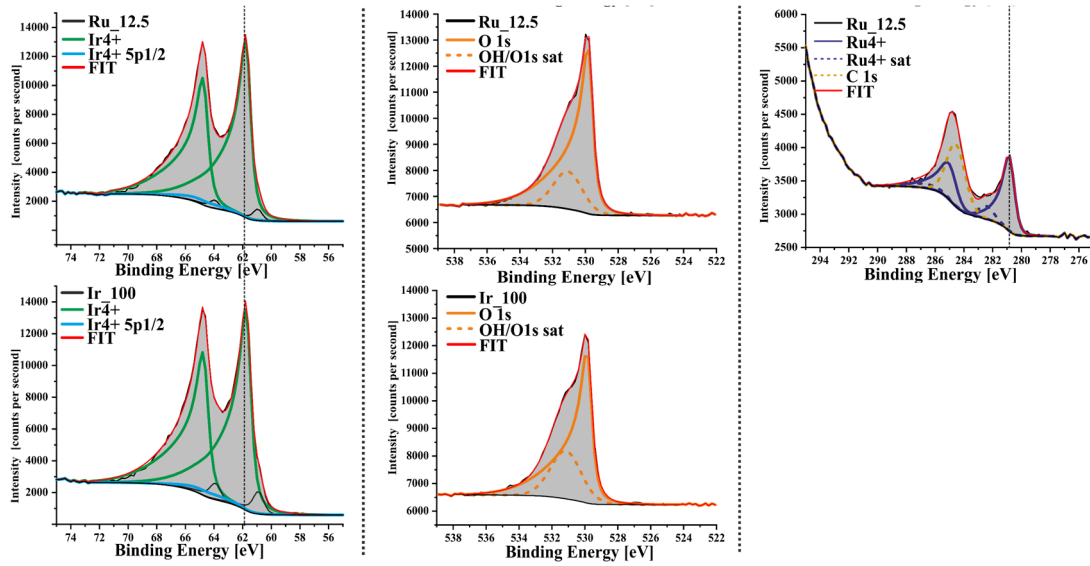
Figure 8.9: Deconvolution of all Ru 3d, Ir 4f and O 1s spectra of the Ru$_x$Ir$_{1-x}$O$_2$ powder samples with varying composition x from x=0 mol% to x=100 mol% in steps of 12.5 mol%.

Table 8.2: Optimized fitting parameters for the deconvolution (Figure 8.9) of the Ru$_x$Ir$_{1-x}$O$_2$ powder samples with varying composition x from x=0 mol% to x=100 mol% in steps of 12.5 mol%.

	Ir_100	Ru_12.5	Ru_25	Ru_37.5	Ru_50	Ru_62.5	Ru_75	Ru_87.5	Ru_100
BE [eV] Ru3d-5/2	-	280.8	280.8	280.8	280.8	280.7	280.7	280.7	280.7
FWHM	-	0.89	0.80	0.77	0.79	0.77	0.76	0.74	0.68
Line shape	LF(0.4,1,45,280)								
BE[eV] Ru3d-3/2	-	284.9	284.9	284.9	284.9	284.9	284.9	284.9	284.9
FWHM	-	1.24	1.26	1.23	1.33	1.30	1.28	1.26	1.22
Line shape	LF(0.4,1,45,280)								
BE [eV] Ru3d-5/2 sat	-	282.3	282.4	282.5	282.5	282.6	282.6	282.7	282.6
FWHM	-	1.90	1.81	1.75	1.84	2.01	1.99	1.99	1.85
Line Shape	LF(0.6,1,45,280)								
BE [eV] Ru3d-3/2 sat	-	286.5	286.6	286.7	286.7	286.8	286.8	286.9	286.8
FWHM	-	2.60	2.51	2.25	2.24	2.55	2.58	2.54	2.39
Line Shape	LF(0.6,1,45,280)								

	Ir_100	Ru_12.5	Ru_25	Ru_37.5	Ru_50	Ru_62.5	Ru_75	Ru_87.5	Ru_100
BE [eV] Ir4f-7/2	61.7	61.7	61.7	61.7	61.7	61.7	61.7	61.7	-
FWHM	0.88	0.85	0.87	0.82	0.85	0.82	0.83	0.79	-
Line shape	LF(0.3,1,60,100)								
BE[eV] Ir4f-5/2	64.7	64.7	64.7	64.7	64.7	64.7	64.7	64.7	-
FWHM	0.93	0.90	0.92	0.87	0.90	0.87	0.89	0.85	-
Line shape	LF(0.3,1,60,100)								
BE [eV] Ir5p-1/2	64.9	64.9	64.9	64.9	64.9	64.9	64.9	64.9	--
FWHM	3.90	3.90	3.90	3.90	3.90	3.90	3.90	3.90	
Line Shape	GL(30)								

	Ir_100	Ru_12.5	Ru_25	Ru_37.5	Ru_50	Ru_62.5	Ru_75	Ru_87.5	Ru_100
BE [eV] O-1s	529.8	529.8	529.7	529.6	529.6	529.5	529.4	529.3	529.2
FWHM	0.76	0.74	0.80	0.82	0.83	0.84	0.82	0.79	0.77
Line shape	LF(0.3,1,65,100)								
BE [eV] OH/ O-1s sat	531.2	531.1	531.0	531.0	531.0	531.1	531.0	531.0	531.2
FWHM	2.09	2.20	2.38	2.40	2.43	2.44	2.40	2.33	2.0
Line shape	GL(30)								

From the integral O 1s, Ir 4f, and Ru 3d intensities the actual stoichiometry of the mixed oxide Ru$_x$Ir$_{1-x}$O$_2$ can be derived. This analysis procedure is pictorially exemplified with the Ru_50 sample in **Figure 8.10** and will be briefly described in the following. The integral O 1s intensity serves as the internal standard among the various Ru 3d spectra, assuming that the O 1s spectrum originates only from O in oxide environment (O^{2-}), regardless of the nominal composition x. This means that also the satellite (O-sat) or the OH feature of O 1s originates from lattice O of Ru$_x$Ir$_{1-x}$O$_2$. It is started with the pure ruthenium sample (Ru_x) for which all ruthenium atoms exposed to XPS are in the Ru^{4+} state. The integral C 1s intensity need to be subtracted first from the integral intensity of Ru 3d. This integrated Ru 3d signal corresponds then to 100 mol% of Ru^{4+}. Next, the O 1s and Ru 3d spectra of a ruthenium-iridium mixed oxide sample are considered. The corresponding integral of the O 1s spectrum needs to be the same as that of the pure ruthenium sample (Ru_100). With this scaling factor the integral of the Ru 3d spectrum (after subtraction of the C 1s signal) can be normalized. With reference to the integral of Ru 3d of Ru_100 the actual stoichiometry factors of Ru4$^+$ are obtained and summarized in **Table 8.3**.
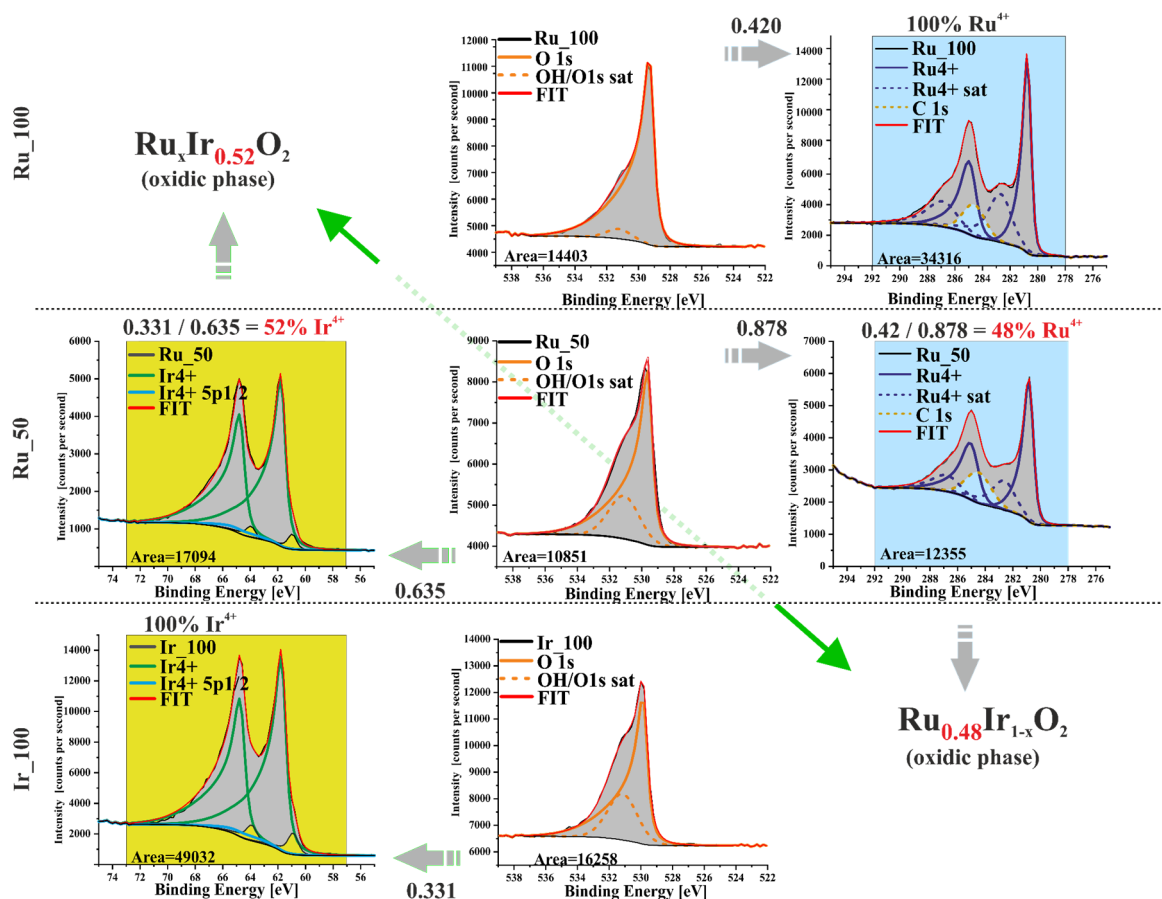
Figure 8.10: Quantification of the mol% of Ir^{4+} and Ru^{4+} of the mixed $Ru_xIr_{1-x}O_2$ oxide phase with x=50 mol% based on the O 1s signal being the reference for all spectra.

The very same procedure can be carried out starting from pure iridium powder sample (Ir_100). The O 1s spectrum serves again as internal standard among the various Ir 4f spectra. From the integral of the Ir 4f spectrum the metallic component (Ir^0) needs to be subtracted. Next, the O 1s and Ir 4f spectra of a mixed ruthenium-iridium oxide are considered. The corresponding integral of the O 1s spectrum needs to be the same as that of Ir_100. With this internal standard the integral of the Ir 4f spectrum (after subtraction of the metallic Ir signal) can be normalized. With reference to the integral of Ir 4f spectrum of Ir_100 the actual stoichiometry factors of Ir^{4+} of the $Ru_xIr_{1-x}O_2$ powders are obtained and compiled in **Table 8.3**. The actual stoichiometry factors of Ru^{4+} and Ir^{4+} are independently determined, but these values require to sum up to 100 mol%. This allows for a consistency check as summarized in **Table 8.3**. Indeed, this sum is virtually unity for all powder samples, confirming nicely the assumption that all O 1s emission stems from O^{2-} derived components in the mixed $Ru_xIr_{1-x}O_2$ oxide. Recall that this procedure is only valid for unsupported powder samples, where the integral intensity of O originates only from the ruthenium-iridium mixed oxide. In case of supported materials such as the ruthenium-iridium mixed oxides, presented in chapter 8.2, the oxygen from the carrier material (TiO_2)

strongly contributes to the measured intensity of O in O 1s, which is why this method cannot be used anymore. For comparison reasons also the stoichiometry values based on the fitting of the XP spectra with CASA-XPS and utilizing element specific cross section for the photoelectron emission process are shown (Quantification with CASAXPS software) in **Table 8.3**. These values agree well with the stoichiometry factors determined based on the internal standard method.

Table 8.3: Determination of Ru^{4+} and Ir^{4+} stoichiometry in $Ru_xIr_{1-x}O_2$ by utilizing the O 1s signal as internal standard. The results of this method are compared with the quantification procedure of the CASA-XPS software.

x [mol%]	Ru^{4+} [mol%] (CASA-XPS)	Ir^{4+} [mol%] (CASA-XPS)	Ru^{4+} [mol%] internal standardization	Ir^{4+} [mol%] internal standardization	$Ru^{4+} + Ir^{4+}$ [mol%]
0	0	100	0	100	100
12.5	8±1	92±1	8±2	95±2	103±2
25	23±1	77±1	24±2	76±2	100±2
37.5	34±1	66±1	35±2	65±2	100±2
50	47±1	53±1	48±2	52±2	100±2
62.5	58±1	42±1	59±2	41±2	100±2
75	72±1	28±1	73±2	27±2	100±2
87.5	85±1	15±1	88±2	15±2	103±2
100	100	0	100	0	100

Besides structure and composition of the mixed ruthenium-iridium catalyst materials, also the morphology is an important characteristic. Morphology can be studied by microscopy (TEM and SEM) together with physisorption experiments to obtain specific surface area and the porosity. SEM micrographs in **Figure 8.11** reveal clearly a macroporous morphology for the Ru_100 sample, while the other samples may be additionally mesoporous due to significantly lower particle/agglomeration size. However, no microporous structure is achieved which is very important as already discussed in chapter 7.2. Micropores lead to additional and undesired transport limitations within the pores during heterogeneous catalysis. TEM images verify the porosity by showing a clear network of particles/agglomeration (insets in **Figure 8.11**). With EDS-SEM also the average composition is quantified and compared with the nominal compositions in **Table 8.4**. The agreement of the compositions is surprisingly good.

Table 8.4: Actual composition given in mol% with regard to ruthenium derived by SEM-EDS in comparison with the nominal composition *x* derived from the employed ratios of the metal precursors. In addition, the BET surface areas of the samples are given determined by Kr-physisorption. *BET** values are surface area per volume and per mass as for *BET*. *BET** values are calculated by multiplying *BET* with averaged density of the samples based on the lattice parameters given by Rietveld refinements.

x nominal [mol%]	0	12.5	25	37.5	50	62.5	75	87.5	100
$Ru^0 + Ru^{4+}$ (EDS) [mol%]	0	9±3	21±3	32±3	53±3	60±3	74±3	87±3	100
BET [$m^2 \cdot g^{-1}$]	11	22	24	23	41	36	27	24	10
BET* [$m^2 \cdot cm^{-3}$]	189	286	314	288	414	369	264	228	81
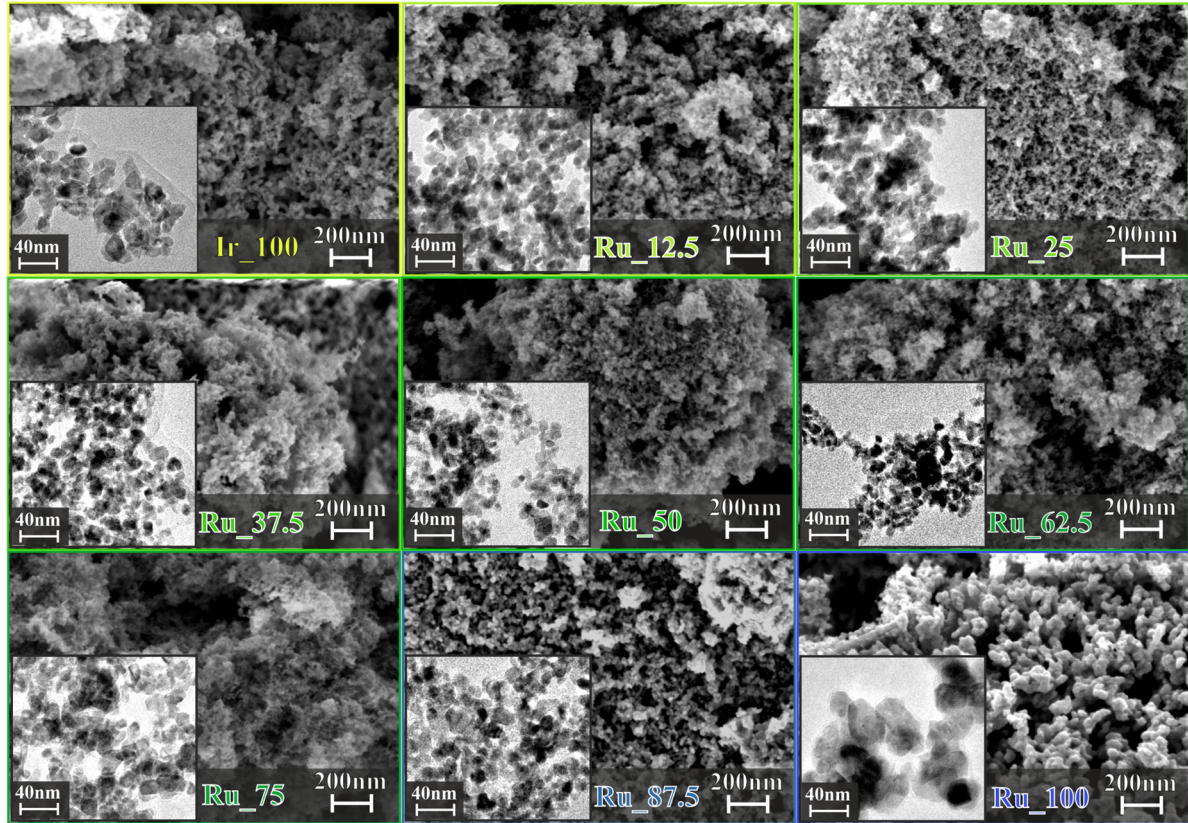
Figure 8.11: SEM and TEM micrographs of ruthenium-iridium mixed powders Ru_*x* for various nominal compositions *x* given in mol% of ruthenium.

Using high-resolution STEM and selected area electron diffraction (SAED) the morphology and structure of the mixed ruthenium-iridium powder catalysts can be investigated. Especially, it is of great interest where the metallic component is located in the secondary particle. In **Figure 8.12** the pure iridium sample (Ir_100) is presented. In the high-resolution bright-field (BF) STEM image (**Figure 8.12a**) oxide particles at the periphery of agglomerates can be assigned based on the observed lattice fringes shown in **Figure 8.12b**. In the agglomerate the transmitted electrons are strongly attenuated and mostly no fringes are observed. The diffraction pattern (in transmission) of a selected area of the sample (typical size about 100 nm diameter) is dominated by diffraction spots distributed on rings belonging to IrO_2 (**Figure 8.12c**),

characteristic for powder samples, while only very few isolated diffraction spots of Ir metal are observed. This observation is in apparent contradiction to the XRD experiments shown in **Figure 8.2** and **Figure 8.4**, which indicate 49% metallic Ir and 51% IrO$_2$ as summarized in **Table 8.1**.

Figure 8.12: a) BF/STEM image showing nanoparticles in Ir_100 sample where lattice fringes corresponding to IrO$_2$(110) can be seen. b) Inverse FFT image where (110) diffraction spots of IrO$_2$ were used for image formation and outline of particles from image a). c) Selected area diffraction pattern (SAED) characteristic for "powder" sample where diffraction spots are forming "powder" rings, it can be indexed as IrO$_2$. There are some isolated spots, labelled with arrows, belonging to Ir(002).

However, the SAED experiment can be rationalized by the morphology where the Ir metal particle is encapsulated by IrO$_2$ particles as concluded from XPS experiments in **Figure 8.6**. Since STEM measures in transmission, the diffraction from the metal particle will be substantially attenuated compared to that of IrO$_2$. This would explain the dominance of IrO$_2$ in the SAED experiments. But this interpretation is also compatible with the high-resolution STEM micrograph, that evidences oxide particles at the periphery of agglomerates. Similar experiments were carried out with the pure ruthenium sample (Ru_100) as shown in **Figure 8.13**. Also for the pure ruthenium powder sample, the SAED pattern (**Figure 8.13c**) is dominated by oxide reflections located in powder rings, while the metallic phase is hardly discernible in this diffraction pattern.
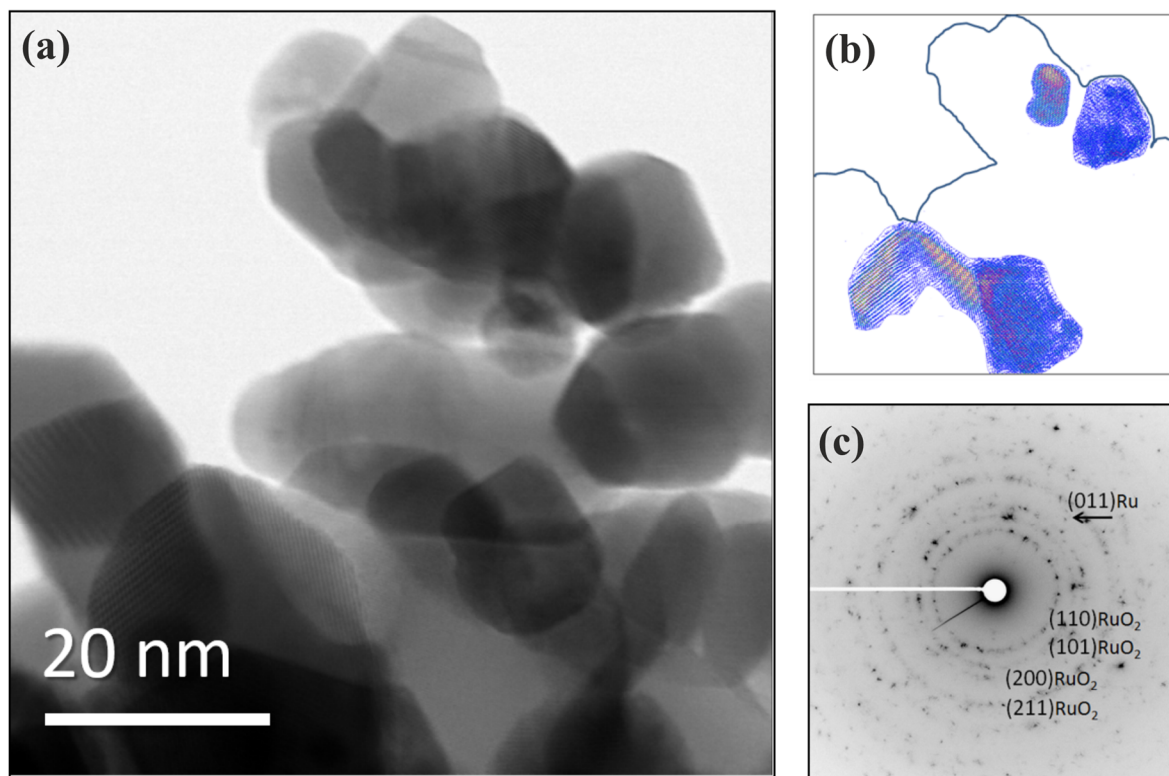
Figure 8.13: a) BF/STEM image showing nanoparticles in Ru_100 sample where lattice fringes corresponding to RuO$_2$ (110) can be seen. b) Inverse FFT image where (110) diffraction spots of RuO$_2$ were used for image formation and outline of particles from image a). c) Selected area diffraction pattern (SAED) characteristic for "powder" sample where diffraction spots are forming circles, it can be indexed as RuO$_2$. There are isolated spots, labelled with arrow, belonging to Ru(011).

For the Ru_50 sample with 50 mol% ruthenium and 50 mol% iridium, high resolution TEM micrographs were taken and element mapping with EDS was performed. In the high-resolution bright-field (BF) STEM image (**Figure 8.14a**) oxide particles clearly can be assigned at the periphery of agglomerates based on the observed lattice fringes (**Figure 8.14b**). The SAED pattern is dominated by the mixed oxide consistent with corresponding XRD data (**Table 8.1**). The element mapping in **Figure 8.14d** reveals an inhomogeneous distribution of iridium and ruthenium across the considered sample area (**Figure 8.14c**). If only mixed oxides contributed to the element mapping, a homogenous distribution of iridium and ruthenium would be expected. According to the XPS experiments in **Figure 8.6,** showing a continuous shift of the O^{2-} component in O 1s with the composition x, the surface consists only of mixed oxide. However, as seen in the XRD experiments a bulk metallic phase in the Ru_50 sample is present as well, which explains the inhomogeneous element distribution in **Figure 8.14d** due to the miscibility gap of Ru-Ir metal alloy. About 50% of the metal particles are iridium-enriched while 50% are ruthenium-enriched according to the XRD experiments shown in **Figure 8.2**. **Figure 8.14d** indeed reveals regions that are highly iridium-rich and ruthenium-rich. The found

compositions of 30 mol% ruthenium and 70 mol% ruthenium are broadly consistent with the compositions of the Ir-rich (21 mol% Ru) and Ru-rich (74 mol% Ru) metal alloy particles in the miscibility gap (**Figure 8.4**).

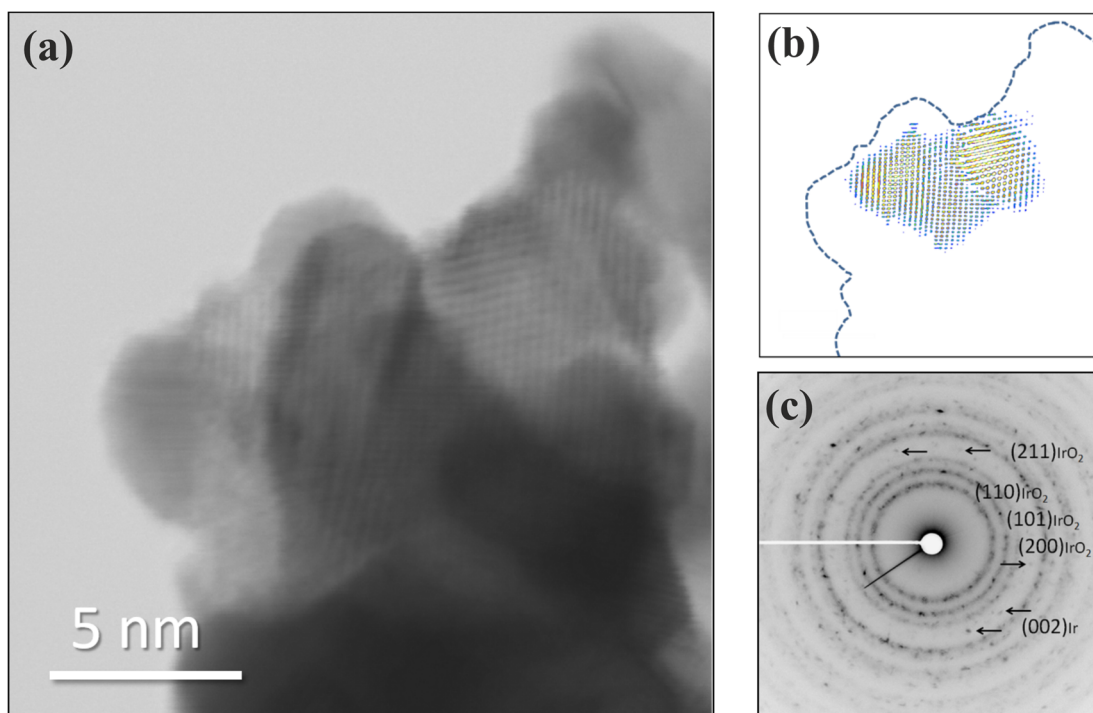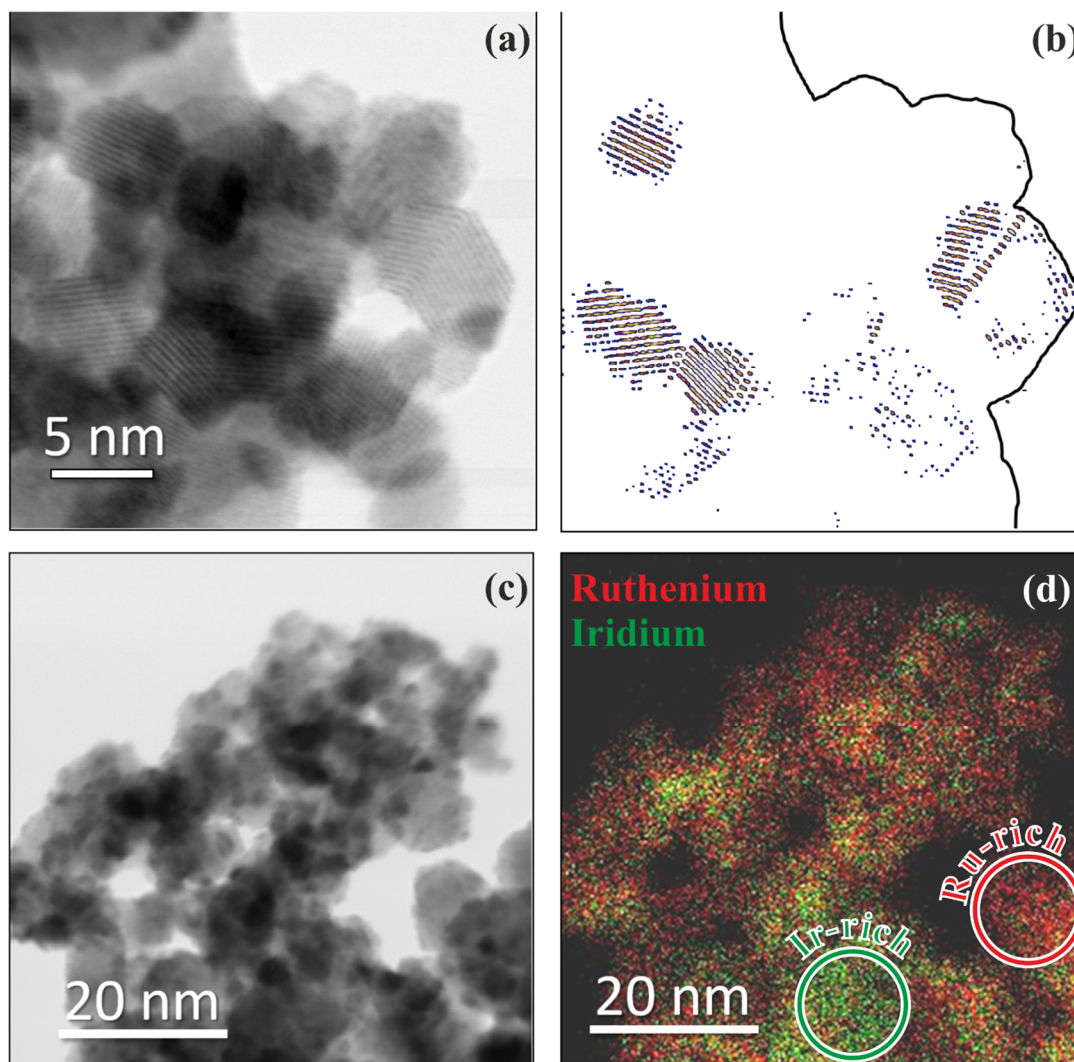**Figure 8.14**: a) BF/STEM image showing nanoparticles in Ru_50 sample where lattice fringes corresponding to oxides. b) Inverse FFT image where (110) and (101) diffraction spots of oxides were used for image formation and outline of particles from image a). c) BF/STEM image of nanoparticles, d) corresponding EDS elemental mapping of the same area. Ruthenium is shown in red and iridium is shown in green. For clarity oxygen is not mapped.

With Kr-physisorption experiments the BET surface areas of the samples are determined and referred to as *BET*, summarized in **Table 8.4**. *BET** values are surface areas per volume that is suitable for visual comparison with particle/agglomeration observed in TEM and the morphology shown in SEM in **Figure 8.11**. *BET** values are in good agreement with SEM and TEM micrographs. For instance, Ru_100 shows biggest particle/agglomerate network that is correlated to the smallest *BET** value of 81 m^2·cm^{-3}. The particle/agglomeration network seen

in TEM for Ir_100 also shows slightly bigger particle than the other samples which is also reflected by the lower *BET** value of 189 $m^2 \cdot cm^{-3}$.

In order to improve the sensitivity to the specific BET surface area Kr instead of N_2 is employed with the trade-off being not able to quantify the porosity of the samples. Therefore, a second batch of five samples (Ru_100_2, Ru_75_2, Ru_50_2, Ru_25_2 and Ir_100_2) is prepared and examined in physisorption experiments with N_2 to focus on the porosity as shown in **Figure 8.15**). All samples show an increase of the cummulative pore volume above 50 nm pore width evidencing that all samples are macroporos in a comparable way as the slopes in **Figure 8.15b** are very similar. However, the meso porosity is different among the samples. Although all samples also show a rising curve in the pore width region of 5 nm to 50 nm the slopes are different. The mixed ruthenium-iridium powders, especially Ru_75_2 and Ru_50_2 reveal a significantly higher amount of meso porosity than the remaining samples. This is in good agreement with the BET surface area of those five samples summarized in the inset of **Figure 8.15a**. However, the resulting *BET* values are significantly different from those of the first/main batch (**Table 8.4**). Obviously, the morphology is less reproducible in Pechini method while the desired chemical composition is well controlled as evidenced by the Rietveld results of the second/additional batch (**Table 8.5**).
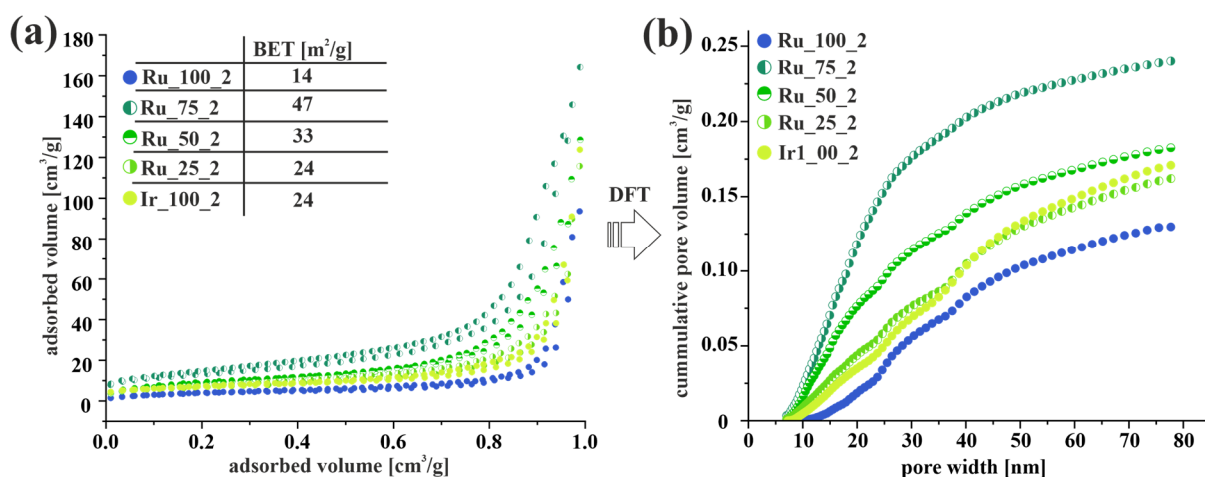
Figure 8.15: Physisorption experiments with N_2 of supplemetary batch_2 with measured isotherms and *BET* values given in a) and calculated pore size distribution by DFT in b).

Table 8.5: Rietveld Refinement of the additional and supporting batch_2.

	Ir_100_2	Ru_25_2	Ru_50_2	Ru_75_2	Ru_100_2
actual comp. **(rutile phase)**	0	0.25	0.48	0.72	1
a,b **[nm]**	4.5090	4.5046	4.502	4.4980	4.5027
c **[nm]**	3.156	3.1462	3.1318	3.1173	3.1050
av. c. size **[nm]**	5.3	7.4	7.3	6.5	11.1
wt%	54.2	59.9	81.5	78.2	95.2
actual comp. **(hcp phase)**	-	0.73	0.76	0.75	1
a,b **[nm]**	-	2.7325	2.7065	2.7116	2.7266
c **[nm]**	-	4.4953	4.4264	4.3062	4.1514
av. c. size **[nm]**	-	1.4	8.3	11.3	8.9
wt%	-	6.6	7.0	21.8	4.8
actual comp. **(fcc phase)**	0	0.19	0.25	-	-
a,b,c **[nm]**	3.862	3.8447	3.8622	-	-
av. c. size **[nm]**	7.2	9.8	2.8	-	-
wt%	45.9	33.5	11.5	-	-

8.1.3 Catalytic CO Oxidation

Since the specific BET surface areas vary quite substantially among the various samples, with Ru_100 and Ir_100 having the lowest *BET* values of 10 $m^2 \cdot g^{-1}$ and 11 $m^2 \cdot g^{-1}$, respectively, the *STY* given in $mol(CO_2) \cdot h^{-1} \cdot kg_{cat}^{-1}$ are normalized to the *BET* values. The normalized *STY*, given in $mol(CO_2) \cdot h^{-1} \cdot m^{-2}$, as a function of the (sample) temperature for the catalytic CO oxidation reaction over unsupported ruthenium-iridium mixed oxides and referred to as Ru_*x* with varying composition *x* are presented in **Figure 8.16**. In this approach it is assumed that the size of the active site does not vary with the composition *x*, and the *BET* is proportional to the number of active sites. According to the XPS experiments, the Ru_*x* samples expose exclusively the oxide phase so that the presented activity data will be regarded as those of mixed $Ru_xIr_{1-x}O_2$ oxides only. The *STY* values are measured during increasing the catalyst temperature with 1 $K \cdot min^{-1}$ for two reaction conditions, i.e., stoichiometric $CO:O_2=2:1$ conditions and oxidizing $CO:O_2=1:2$ conditions (volumetric ratios).

The overall activity declines when switching from oxidizing (**Figure 8.16b**) to stoichiometric (**Figure 8.16a**) reaction conditions as can be seen by the shift of the light-off curves towards lower temperatures in case of the oxidizing reaction condition. The pure IrO_2 (Ir_100) is the least active catalyst among the studied mixtures. With increasing nominal composition *x* up to 62.5 mol% the activity increases as also reflected by the temperatures required to reach a specific *STY* (1 $mmol(CO_2) \cdot h^{-1} \cdot m^{-2}$ or 2 $mmol(CO_2) \cdot h^{-1} \cdot m^{-2}$ for oxidizing or stoichiometric reaction conditions, respectively). However, the pure RuO_2 system is not the most active catalyst, at least not for stoichiometric reaction conditions. Instead, the mixed oxide $Ru_{0.875}Ir_{0.125}O_2$ (Ru_87.5) turns out to be the most active catalyst, while the $Ru_{0.75}Ir_{0.25}O_2$

(Ru_75) is less active than expected from general trend of activity. At higher reaction temperatures and under stoichiometric reaction conditions (**Figure 8.16a**) even $Ru_{0.625}Ir_{0.375}O_2$ (Ru_62.5) is more active than pure RuO_2 (Ru_100). However, the temperature behavior of the normalized *STY* of RuO_2 is quite different from all the other samples. The slope is flatter so that the low temperature activity of RuO_2 is highest among the samples but the activity curve of RuO_2 intersects at higher reaction temperatures those of other oxides with lower nominal ruthenium composition *x*. This explains why RuO_2 is not in all cases the most active catalyst.

Figure 8.16: *BET*-normalized *STY* curves as a function of temperature (light-off experiments) for the catalytic CO oxidation reaction over mixed ruthenium-iridium powder samples under a) stoichiometric $CO:O_2=2:1$ and b) oxidative $CO:O_2=1:2$ conditions.

The overall activity declines when switching from oxidizing (**Figure 8.16b**) to stoichiometric (**Figure 8.16a**) reaction conditions as can be seen by the shift of the light-off curves towards lower temperatures in case of the oxidizing reaction condition. The pure IrO_2 (Ir_100) is the least active catalyst among the studied mixtures. With increasing nominal composition *x* up to 62.5 mol% the activity increases as also reflected by the temperatures required to reach a specific *STY* (1 $mmol(CO_2) \cdot h^{-1} \cdot m^{-2}$ or 2 $mmol(CO_2) \cdot h^{-1} \cdot m^{-2}$ for oxidizing or stoichiometric reaction conditions, respectively). However, the pure RuO_2 system is not the most active catalyst, at least not for stoichiometric reaction conditions. Instead, the mixed oxide $Ru_{0.875}Ir_{0.125}O_2$ (Ru_87.5) turns out to be the most active catalyst, while the $Ru_{0.75}Ir_{0.25}O_2$ (Ru_75) is less active than expected from general trend of activity. At higher reaction temperatures and under stoichiometric reaction conditions (**Figure 8.16a**) even $Ru_{0.625}Ir_{0.375}O_2$

(Ru_62.5) is more active than pure RuO$_2$ (Ru_100). However, the temperature behavior of the normalized *STY* of RuO$_2$ is quite different from all the other samples. The slope is flatter so that the low temperature activity of RuO$_2$ is highest among the samples but the activity curve of RuO$_2$ intersects at higher reaction temperatures those of other oxides with lower nominal ruthenium composition *x*. This explains why RuO$_2$ is not in all cases the most active catalyst.

In **Figure 8.17** Arrhenius-like plots are shown with the activity given as a function of the (sample) temperature. In general, the Arrhenius plot is defined as the ln(*k*) (with *k* being the rate constant) as a function of 1/*T*. However, this plot requires the determination of the reaction order. For the determination of the apparent activation energy E_{act}, the very same information is already provided by ln(*STY*) as a function of the 1/*T* as previously pointed out in **equation 7.7**.
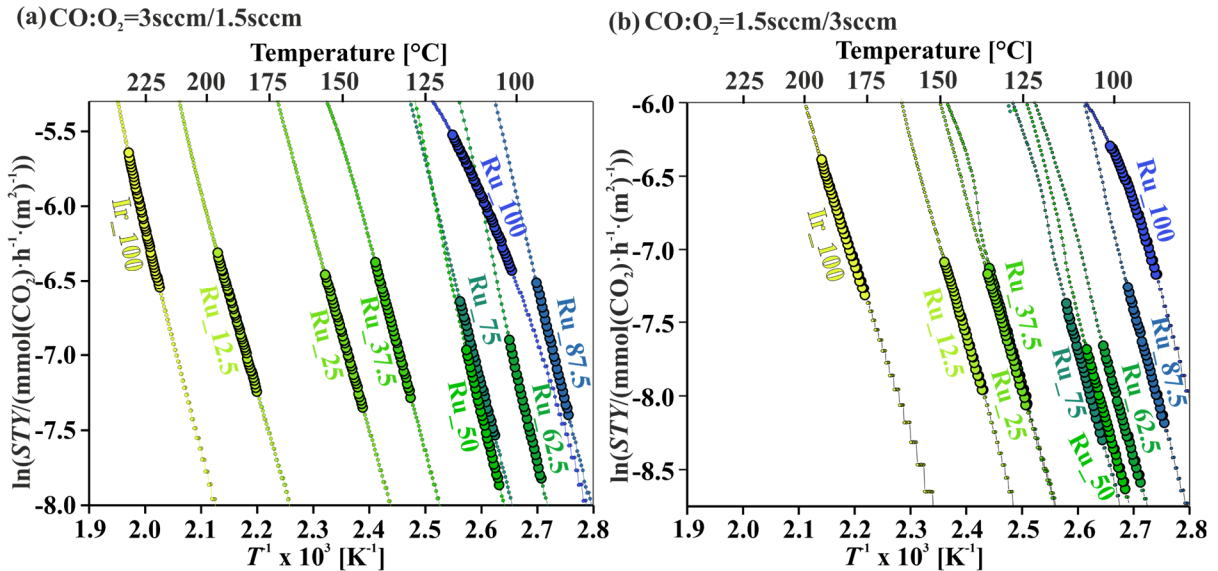
Figure 8.17: Arrhenius plots in terms of *STY* normalized to the *BET* from Figure 8.16 of CO oxidation over various mixed ruthenium-iridium oxide powder samples for two reaction conditions: a) oxidative (CO:O$_2$=1:2) condition and b) stoichiometric (CO:O$_2$=2:1) condition. For each sample, the Arrhenius parameters are taken from those parts (big circles) of the plots where the conversion *X* varies from 2% to 5%.

From the Arrhenius plots in **Figure 8.17** the apparent activation energies are derived, which are summarized in **Table 8.6**. The apparent activation energy E_{act} defines the temperature behavior of the activity, but is not necessarily indicative of the height of an activation barrier nor of the actual activity. For the actual activity the pre-factor STY_0 needs to be considered in addition ($STY=STY_0 \cdot e^{-E_{act}/RT}$).

In principle, a low apparent activation energy is beneficial for low temperature activity, but higher apparent activation energies allow for a steeper increase in activity with rising

temperatures that will eventually surpass the activity of a catalyst with lower apparent activation energy. The prefactor STY_0 depends on the concentrations of CO and O_2 in the reaction mixture via the reaction order (**equation 7.7**), the number of active sites and maybe other parameters such as the temperature in case of diffusion limitations. Assuming that identical reaction conditions and conversions are employed, then the variation in STY_0 should essentially reflect the change in the number of active sites among the catalysts.

For a stoichiometric reaction mixture, the apparent activation energies are 71 kJ·mol^{-1} for pure RuO_2 and 135 kJ·mol^{-1} for pure IrO_2. In between these antipodes the activation energy of $Ru_xIr_{1-x}O_2$ does not reveal a clear pattern. Already a substitution of approximately 12.5 mol% of Ru^{4+} with Ir^{4+} ($Ru_{0.875}Ir_{0.125}O_2$) increases the apparent activation energy to 130 kJ·mol^{-1}, while the substitution of 12.5 mol% of Ir^{4+} with Ru^{4+} ($Ru_{0.125}Ir_{0.875}O_2$) decreases the apparent activation energy to 109 kJ·mol^{-1}. The prefactors STY_0 vary by eight orders of magnitude among the various mixed oxides. However, there is a general pattern, the higher the apparent activation the higher the prefactor, indicating the Cremer-Constable compensation effect. Based on the low apparent energy one could have expected that the RuO_2 catalyst is also the most active one. However, the prefactor STY_0 of RuO_2 is the lowest among the mixed oxide catalyst. Consequently, RuO_2 is less active than $Ru_{0.875}Ir_{0.125}O_2$, in the considered temperature range.

Table 8.6: Apparent activation energies E_{act} and prefactors STY_0 derived from the Arrhenius plots in Figure 8.17.

x [mol%]	0	12.5	25	37.5	50	62.5	75	87.5	100
E_{act} (stoich.)	135	109	110	118	127	135	120	130	71
STY_0 (stoich.)	$3·10^{11}$	$2·10^9$	$4·10^{10}$	$1·10^{12}$	$1·10^{14}$	$5·10^{15}$	$2·10^{13}$	$3·10^{15}$	$1·10^7$
E_{act} (oxid.)	97	107	107	114	114	113	116	117	90
STY_0 (oxid.)	$1·10^9$	$1·10^{10}$	$4·10^{10}$	$2·10^{11}$	$2·10^{12}$	$3·10^{12}$	$3·10^{12}$	$2·10^{13}$	$5·10^9$

For the oxidizing reaction mixture, the apparent activation energy is 112±5 kJ·mol^{-1} and hardly varies with the nominal composition x among the mixed $Ru_xIr_{1-x}O_2$ oxides. Also the prefactors do not vary as much as for stoichiometric reaction conditions. Only the apparent activation energies of pure IrO_2 with 97 kJ·mol^{-1} and that of pure RuO_2 sample with 90 kJ·mol^{-1} are substantially lower albeit partly compensated by lower prefactors.

To a first approximation, the apparent activation energy should not depend on the reaction mixture. However, the derived apparent activation energies in **Table 8.6** vary among the Ru_x

powder samples and depend on the employed reaction mixture. On the average, the apparent activation energies for the stoichiometric mixture are higher than those for the oxidizing reaction mixture. Of course, this behavior in apparent activation energy cannot be reconciled with an activation barrier that is expected to be independent on the reaction order. However, a different activation energy may point towards different populations of reaction intermediates at the catalyst's surface and therefore towards a different critical (rate-limiting) reaction step.

Several models exist that relate the apparent activation energy to specific energy levels of the reaction intermediates, such as the model by Campbell et al. which states that the apparent activation energy is given as the weighted average of all activation barrier of every reaction step involved.[210] Another reasonable model for heterogeneously catalysed reactions, derived from the transition state theory, is given by the pre-equilibrium approximation[211] where the apparent activation energy E_a is the sum of the rate-limiting activation barrier and the reaction enthalpy of the preceded equilibrium reaction(s) according to **equation 8.1**.

$$E_a = E_{rds} + \Delta_r H^0 \qquad (8.1)$$

If a Langmuir-Hinshelwood mechanism is assumed, as reported for CO oxidation over single-crystalline RuO$_2$(110),[212,213] with the recombination of the adsorbed on-top CO and O (CO$_{ot}$+O$_{ot}$→CO$_2$)[214] as the *TOF*-limiting step and the adsorption of CO and dissociative adsorption of O$_2$ represented each by a chemical equilibrium, then **equation 8.2** may be established. Note, that this is an assumption, kinetic Monte-Carlo simulations at 350 K actually showed that the adsorption of CO, the diffusion of adsorbed O and the recombination of CO$_{ot}$ and O$_{ot}$ can have similar activation energies.[215]

$$E_a = E_{(CO,ads+O,ads \to CO2,ads)} + \Delta_{CO \to CO,ads} H^0 + \Delta_{O2 \to 2O,ads} H^0 \qquad (8.2)$$

The reaction enthalpies $\Delta_{CO \to CO,ads} H^0$ and $\Delta_{O2 \to 2O,ads} H^0$ according to Hess's law ($\Delta_r H^0 = \sum \Delta_f H_i^0$) depend on the standard enthalpy of formation ($\Delta_f H_i^0$) of the involved species, here CO, CO$_{ads}$ and O$_2$, O$_{ads}$. Furthermore, the surface coverage θ is a function of the corresponding partial pressure ($\theta = f(p,T)$), which is why the different reactant concentrations (partial pressures) under stoichiometric and oxidizing conditions lead to dissimilar surface populations. That in turn affects the adsorption enthalpy of the associated species according to the Freundlich-equation,[216] which is reasonable for a real catalytic surface with energetically differing adsorption sites. To conclude, the partial pressure of a reactant influences the adsorption

enthalpy and by that also the enthalpy of formation ($\Delta_{CO,ads}H^0$ and $\Delta_{O2,ads}H^0$) and ultimately the apparent activation energy E_a (**equation 8.2**).

The presented ruthenium-iridium mixed oxides (except for pure RuO$_2$) show lower apparent activation energies for oxidizing reaction conditions than for stoichiometric conditions (**Table 8.6**), which may indicate that the dissociation and population of oxygen is much more crucial and mandatory. Therefore, a Mars-van-Krevelen mechanism is unlikely for the iridium-containing materials. This molecular picture is strongly supported by a computational study from Yeh et al. who report that a Mars-van-Krevelen mechanism is energetically unfavoured and either Langmuir-Hinshelwood or Eley-Rideal are reasonable mechanisms.[217] Considering that the lower partial pressure of CO under oxidizing conditions (1.5sccm) compared to the stoichiometric conditions (3 sccm) does not increase the activation energy, it is concluded that IrO$_2$ and the ruthenium-iridium mixed oxides follow rather a Eley-Rideal mechanism, where the CO does not adsorb on the noble metal site, than a Langmuir-Hinshelwood mechanism. Only for RuO$_2$, a lower activation energy under stoichiometric conditions was observed, which may suggest that the population of adsorbed CO molecules is essential, whereas the dissociative adsorption of gaseous oxygen is seemingly less influential. Therefore, a Mars-van Krevelen mechanism is suggested for RuO$_2$ as also reported by Over, Ertl et al. over single-crystalline RuO$_2$(110).[218]

8.1.4 Post-catalytic Characterization of Ru$_x$Ir$_{1-x}$O$_2$

The X-ray diffractograms after reaction (**Figure 8.18**) are identical to those before the CO oxidation reaction (**Figures 8.2**), implying that the bulk structures and compositions of the mixed oxide and the metallic phases with fcc and hcp structure are not changed under oxidizing and stoichiometric CO oxidation reaction conditions, namely CO:O$_2$=1:2 and CO:O$_2$=2:1, up to a maximum reaction temperature of 230 °C.
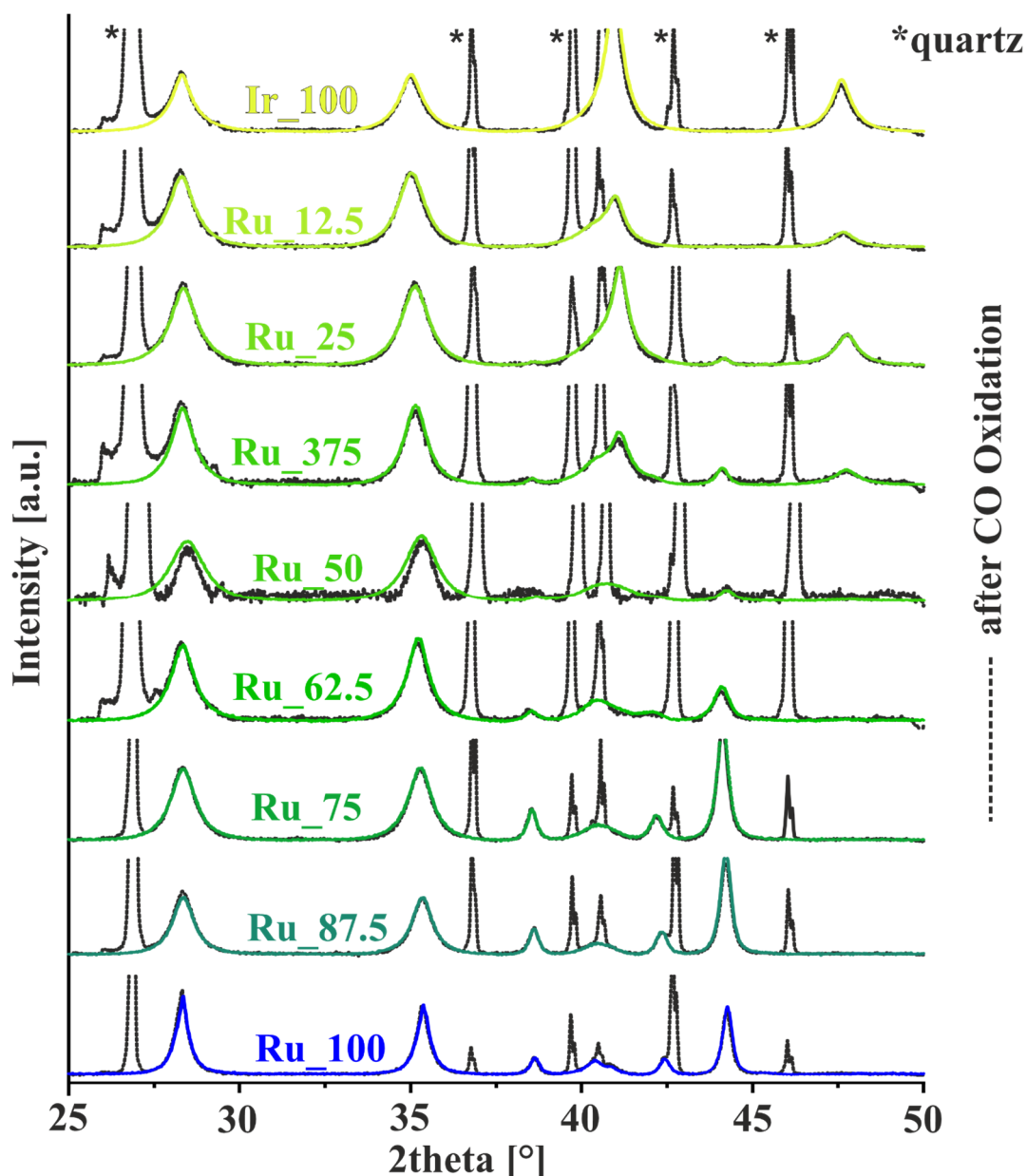
Figure 8.18: X-ray diffractograms of unsupported Ru$_x$Ir$_{1-x}$O$_2$ powder samples before and after (black) stoichiometric and oxidative CO catalysis showing no observable/significant bulk changes.

The surface regions of the mixed oxides are also stable against reduction as indicated by the XP spectra shown in **Figures 8.19** for the samples after oxidative CO oxidation and **Figure 8.20** for the sample after stoichiometric CO oxidation. The fitting parameters of the deconvolution are compiled in **Table 8.7** and **Table 8.8**.

Ir-4f
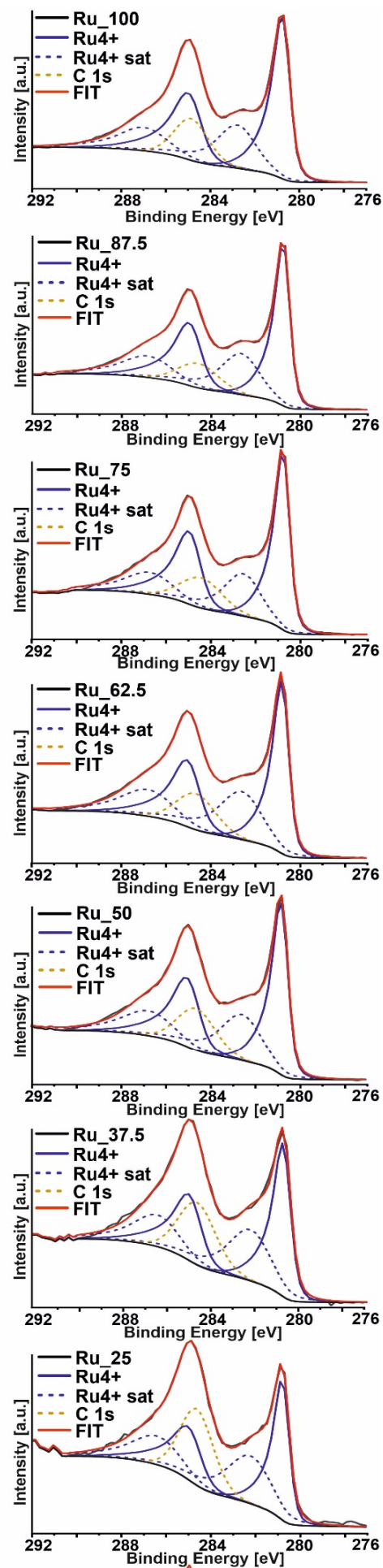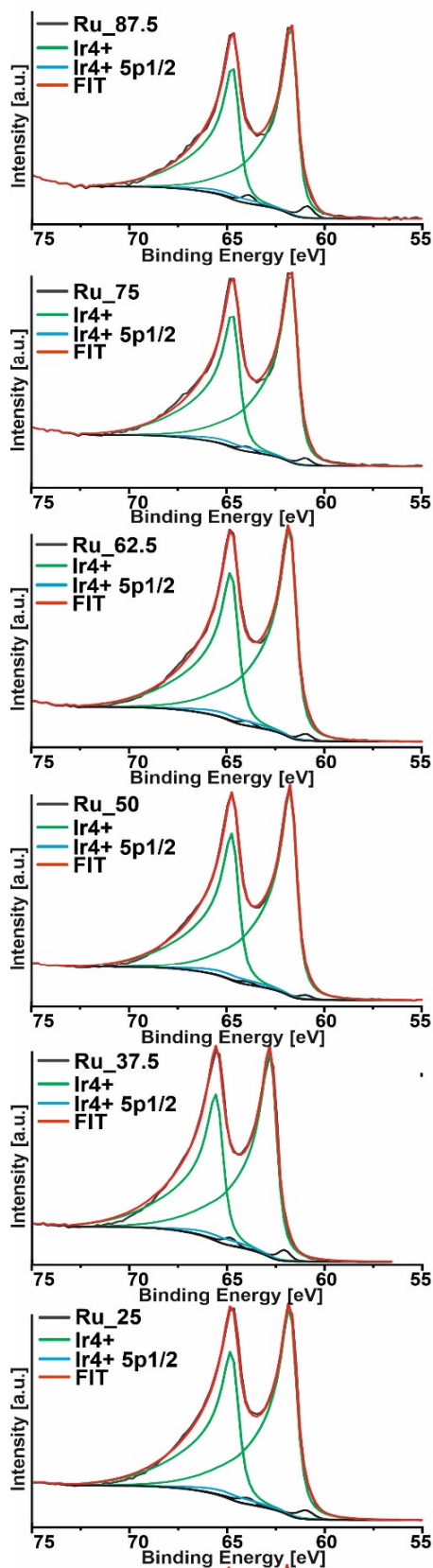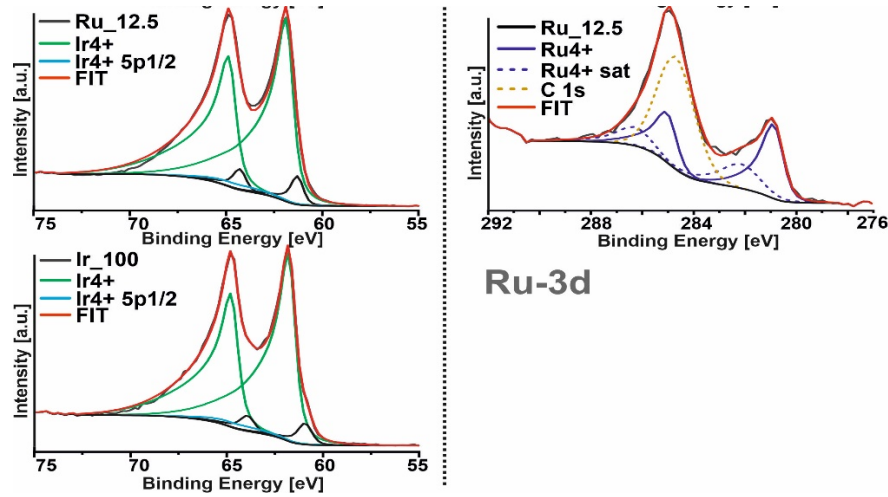
Figure 8.19: Deconvolution of all Ru 3d and Ir 4f spectra of unsupported Ru$_x$Ir$_{1-x}$O$_2$ powder samples after oxidative CO catalysis.

Table 8.7: Optimized fitting parameters for the deconvolution of Ru 3d and Ir 4f of Ru$_x$Ir$_{1-x}$O$_2$ powder samples after oxidative CO catalysis.

	Ir_100	Ru_12.5	Ru_25	Ru_37.5	Ru_50	Ru_62.5	Ru_75	Ru_87.5	Ru_100
BE [eV] Ru3d-5/2	-	280.8	280.7	280.7	280.7	280.7	280.7	280.7	280.7
FWHM	-	0.90	0.79	0.79	0.77	0.76	0.75	0.73	0.70
Line shape	LF(0.4,1,45,280)								
BE[eV] Ru3d-3/2	-	284.9	284.8	284.8	284.9	284.9	284.8	284.8	284.8
FWHM	-	1.20	1.30	1.24	1.27	1.31	1.26	1.26	1.27
Line shape	LF(0.4,1,45,280)								
BE [eV] Ru3d-5/2 sat	-	282.3	282.1	282.0	282.4	282.5	282.4	282.5	282.4
FWHM	-	1.90	1.85	1.90	1.90	2.15	1.95	1.95	1.90
Line Shape	LF(0.6,1,45,280)								
BE [eV] Ru3d-3/2 sat	-	286.3	286.6	286.2	286.6	286.7	286.6	286.7	286.6
FWHM	-	2.59	2.40	2.15	2.31	2.60	2.65	2.50	2.39
Line Shape	LF(0.6,1,45,280)								

	Ir_100	Ru_12.5	Ru_25	Ru_37.5	Ru_50	Ru_62.5	Ru_75	Ru_87.5	Ru_100
BE [eV] Ir4f-7/2	61.7	61.8	61.7	61.7	61.7	61.7	61.7	61.7	-
FWHM	0.88	0.87	0.91	0.90	0.84	0.87	0.82	0.79	-
Line shape	LF(0.3,1,60,100)								
BE[eV] Ir4f-5/2	64.7	64.8	64.7	64.7	64.7	64.7	64.7	64.7	-
FWHM	0.93	0.92	0.96	0.95	0.89	0.92	0.87	0.84	-
Line shape	LF(0.3,1,60,100)								
BE [eV] Ir5p-1/2	64.8	64.9	64.9	64.9	64.8	64.8	64.8	64.8	--
FWHM	3.90	3.90	3.90	3.90	3.90	3.90	3.90	3.90	
Line Shape	GL(30)								
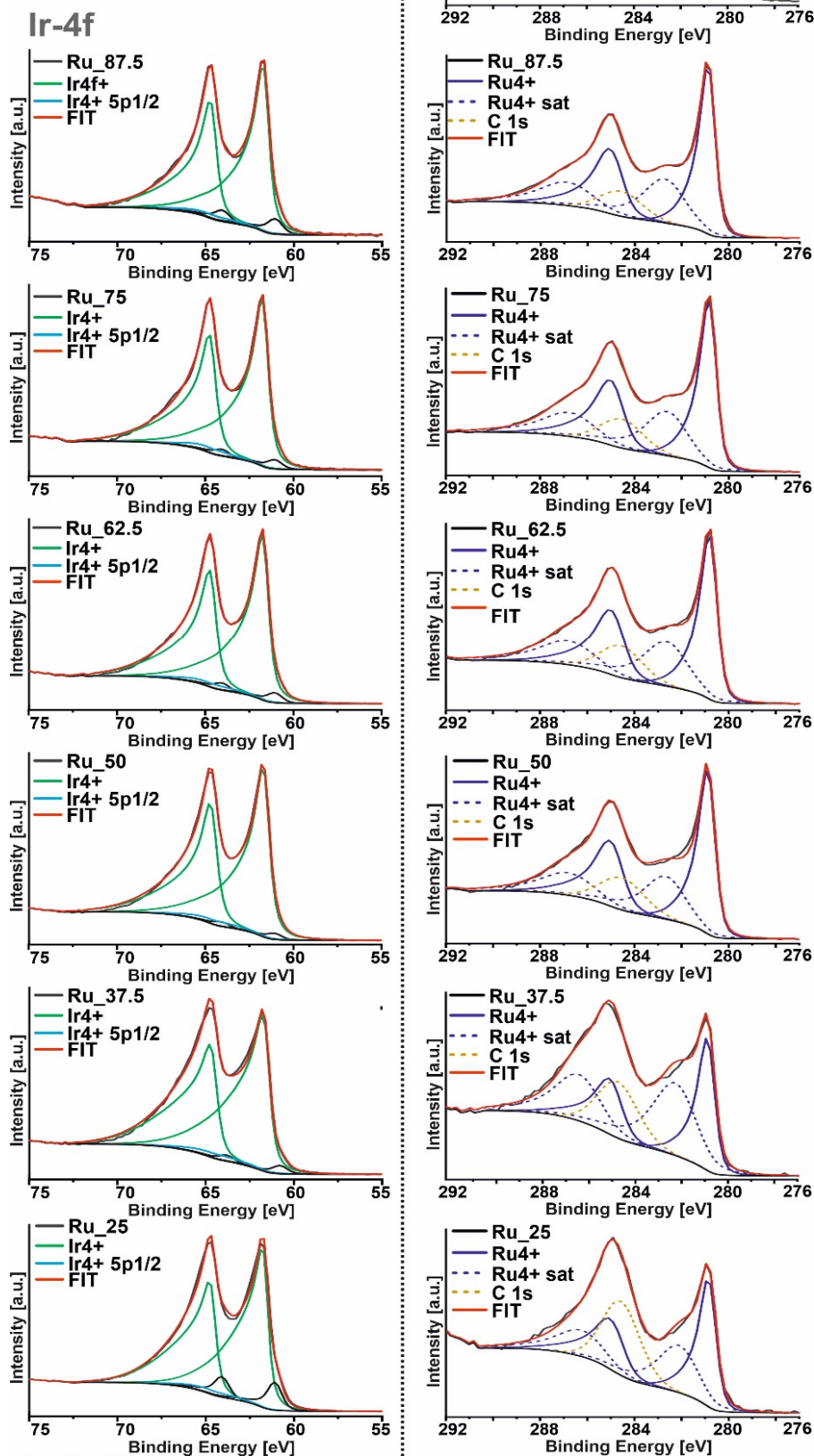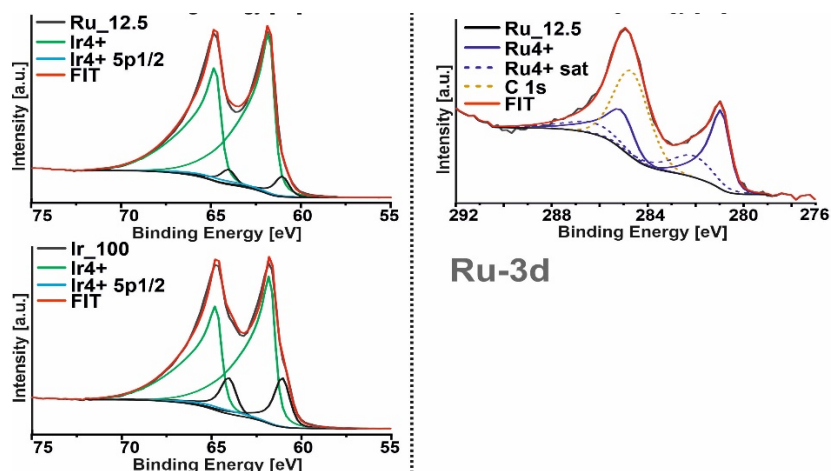
Figure 8.20: Deconvolution of all Ru 3d and Ir 4f spectra of unsupported Ru$_x$Ir$_{1-x}$O$_2$ powder samples after stoichiometric CO catalysis.

Table 8.8: Optimized fitting parameters for the deconvolution of Ru 3d and Ir 4f of Ru$_x$Ir$_{1-x}$O$_2$ powder samples after stoichiometric CO catalysis.

	Ir_100	Ru_12.5	Ru_25	Ru_37.5	Ru_50	Ru_62.5	Ru_75	Ru_87.5	Ru_100
BE [eV] Ru3d-5/2	-	280.8	280.7	280.7	280.7	280.7	280.7	280.7	-
FWHM	-	0.88	0.79	0.78	0.77	0.76	0.75	0.73	-
Line shape	LF(0.4,1,45,280)								
BE[eV] Ru3d-3/2	-	284.9	284.8	284.8	284.9	284.9	284.9	284.9	-
FWHM	-	1.21	1.35	1.25	1.30	1.32	1.30	1.28	-
Line shape	LF(0.4,1,45,280)								
BE [eV] Ru3d-5/2 sat	-	281.9	281.9	282.0	282.4	282.5	282.4	282.5	-
FWHM	-	1.90	1.90	2.10	2.01	2.10	1.99	2.00	-
Line Shape	LF(0.6,1,45,280)								
BE [eV] Ru3d-3/2 sat	-	286.1	286.1	286.1	286.6	286.7	286.6	286.7	-
FWHM	-	2.50	2.30	2.20	2.57	2.62	2.45	2.53	-
Line Shape	LF(0.6,1,45,280)								

	Ir_100	Ru_12.5	Ru_25	Ru_37.5	Ru_50	Ru_62.5	Ru_75	Ru_87.5	Ru_100
BE [eV] Ir4f-7/2	61.6	61.7	61.7	61.7	61.6	61.7	61.7	61.7	-
FWHM	0.75	0.75	0.77	0.88	0.88	0.86	0.84	0.82	-
Line shape	LF(0.3,1,60,100)/ LF(0.3,1,55,100)								
BE[eV] Ir4f-5/2	64.6	64.7	64.7	64.6	64.6	64.7	64.7	64.7	-
FWHM	0.80	0.80	0.82	0.94	0.93	0.91	0.89	0.87	-
Line shape	LF(0.3,1,60,100)								
BE [eV] Ir5p-1/2	64.8	64.8	64.8	64.8	64.8	64.9	64.8	64.8	--
FWHM	3.90	3.90	3.90	3.90	3.90	3.90	3.90	3.90	
Line Shape	GL(30)								

In particular, the Ru 3d spectra indicate only oxidic Ru^{4+}; metallic Ru is not discernible in XPS. However, the actual composition of $Ru_xIr_{1-x}O_2$ decreases by 5-10 mol% with regard to Ru^{4+} after CO oxidation reaction (corresponds to an $Ir4^+$ enrichment), regardless of the chosen reaction mixture (**Figure 8.21, Table 8.9**). This systematic change in the near surface composition of the mixed oxides is likely a temperature effect when the reaction temperature is 230 °C for several hours. From the viewpoint of oxygen affinity one would have expected an enrichment of Ru^{4+} at the surface. Exemplarily, in **Figure 8.22** the XP spectra of Ru 3d and Ir 4f before and after oxidative and stoichiometric CO oxidation are shown for the Ru_50 sample, clearly indicating the relative increase of the iridium concentration at the surface.
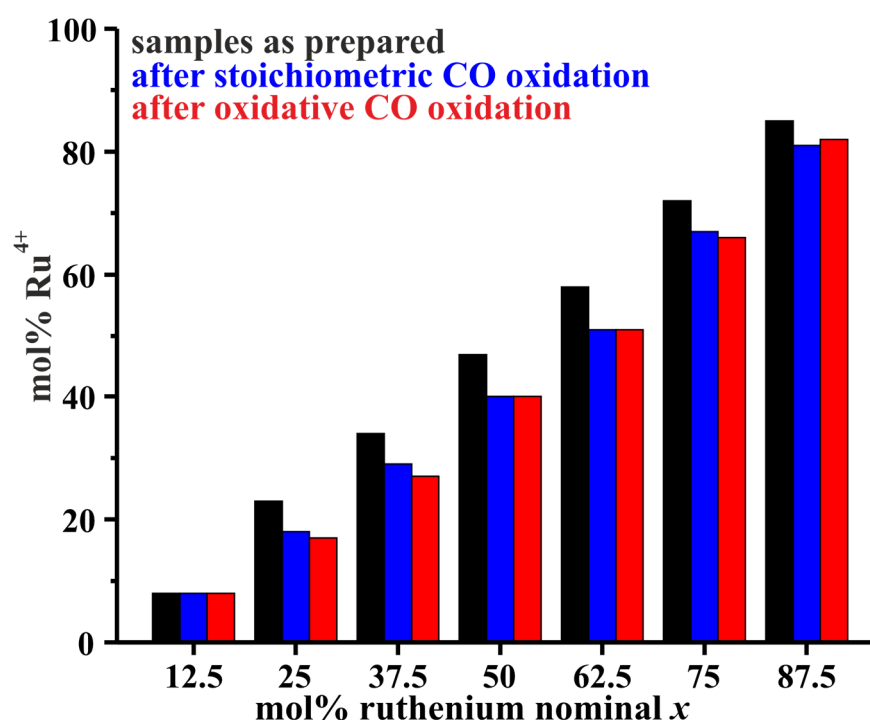
Figure 8.21: Change in oxidic Ru^{4+} signal in XPS of unsupported mixed ruthenium-iridium powder samples before and after CO oxidation catalysis indicating a systematic decrease of the actual Ru^{4+} concentration after the reaction.
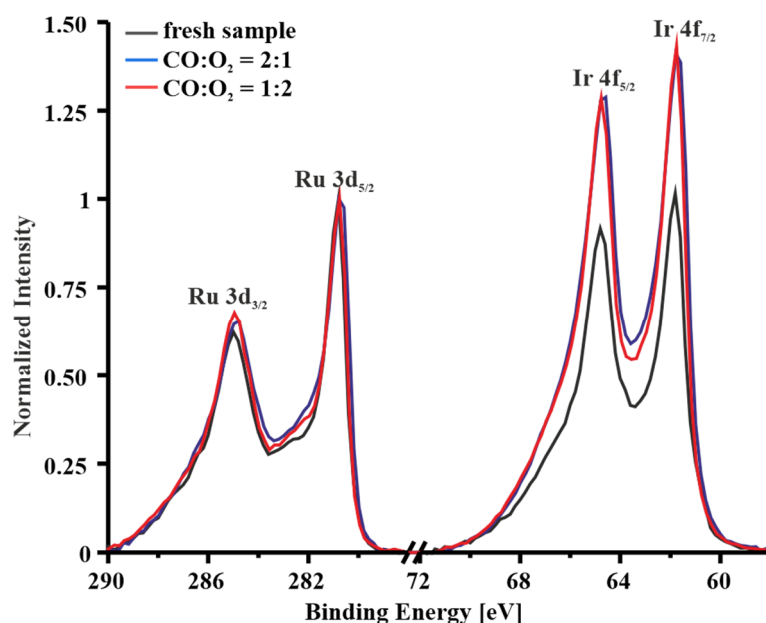
Figure 8.22: Ru 3d and Ir 4f spectra of $Ru_{0.5}Ir_{0.5}O_2$ before CO oxidation and after CO oxidation under oxidizing and stoichiometric reaction condition.

Table 8.9: XPS-Quantification by CASA-XPS of $Ru_xIr_{1-x}O_2$ powder samples after oxidative and stoichiometric CO oxidation by CASA-XPS.

x [mol%]	Ru^{4+} [mol%] (CASA-XPS) before catalysis	Ru^{4+} [mol%] (CASA-XPS) after oxidative catalysis	Ru^{4+} [mol%] (CASA-XPS) after stoichiometric catalysis
0	0	0	0
12.5	8±1	8±1	8±1
25	23±1	18±1	17±1
37.5	34±1	29±1	27±1
50	**41±1**	**40±1**	**40±1**
62.5	58±1	51±1	51±1
75	72±1	67±1	66±1
87.5	85±1	81±1	82±1
100	100	100	100

According to the XPS experiments after CO oxidation reaction, the metallic Ir content varies (**Figure 8.23, Table 8.10**) in the surface-near region of the mixed $Ru_xIr_{1-x}O_2$ oxide. This variation depends on the employed reaction mixture. For a stoichiometric mixture, $CO:O_2=2:1$, the metallic surface Ir component increases for the iridium-rich mixed oxides, while the metallic surface Ir component remains constant for other compositions. Only $Ru_{0.5}Ir_{0.5}O_2$ indicates a slight decrease in the metallic Ir component. For the pure IrO_2 sample the increase in the metallic surface Ir component is most prominent, namely from 6 mol% (before) to 19 mol% (after reaction). For oxidizing reaction conditions, $CO:O_2=1:2$, the metallic surface Ir component decreases for most nominal compositions x of the $Ru_xIr_{1-x}O_2$. Only the pure IrO_2

and the $Ru_{0.125}Ir_{0.875}O_2$ samples reveal an increase of the metallic Ir surface component. It needs to be emphasized that the Ru 3d does not show any sign of metallic Ru in the Ru 3d spectra, evidencing that the exposed ruthenium is always completely oxidized (Ru^{4+}).
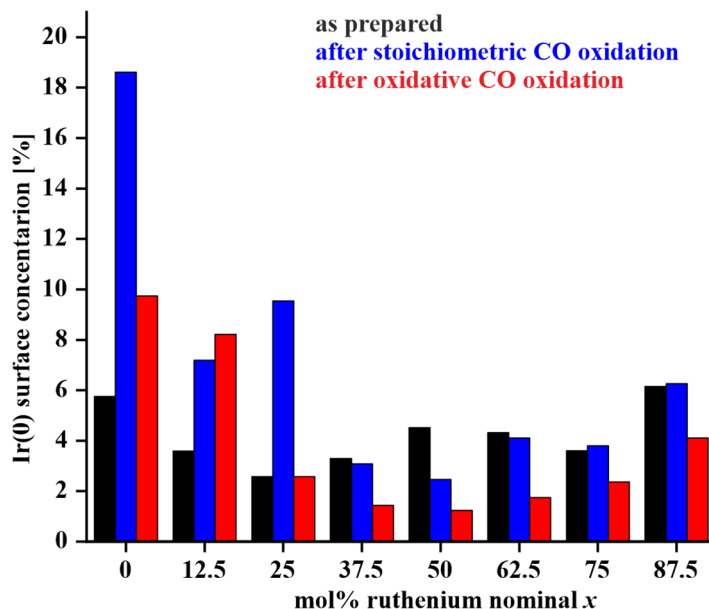
Figure 8.23: Surface-near concentrations of metallic iridium before and after CO oxidation reaction for various unsupported $Ru_xIr_{1-x}O_2$ powder samples.

Table 8.10: XPS-Quantification by CASA-XPS of metallic iridium Ir(0) in $Ru_xIr_{1-x}O_2$ powder samples before and after CO catalysis.

x [mol%]	Ir(0) [mol%] (CASA-XPS) before catalysis	Ir(0) [mol%] (CASA-XPS) after stoichiometric catalysis	Ir(0) [mol%] (CASA-XPS) after oxidative catalysis
0	6±1	19±1	10±1
12.5	4±1	7±1	8±1
25	3±1	10±1	3±1
37.5	3±1	3±1	1±1
50	5±1	2±1	1±1
62.5	4±1	4±1	2±1
75	4±1	4±1	2±1
87.5	6±1	6±1	4±1
100	0	0	0

Altogether, the post-reaction characterization experiments indicate that the bulk structure and bulk composition is not affected by the CO oxidation reaction, while the Ir^{4+} surface concentration of the mixed oxides is enriched due likely to a temperature effect, rather than due to the actual reaction conditions. Quite in contrast the amount of metallic Ir in the surface-near region of $Ru_xIr_{1-x}O_2$ depends on the actual reaction conditions.

8.1.5 Discussion

From exhaustive bulk and surface characterization the following mechanistic steps in the Pechini synthesis of unsupported ruthenium-iridium mixed oxide particles (**Figure 8.24**) are implied: First the metal particles nucleate during the initial stage of the calcination step, since O$_2$ cannot permeate the polymer network, thus producing a net reducing environment for the growing particle where the metal cations Ir^{4+} and Ru^{3+} are reduced to Ir^0 and Ru^0 and the C backbone is oxidized to CO$_2$. Accordingly, a mixed Ru-Ir metal phase is formed, whose mean composition is defined by the local concentrations of the metal ions. Depending on the nominal composition *x* either a single alloy is formed or the alloy disproportionates into an Ir-enriched fcc phase and a Ru-enriched hcp phase owing to the miscibility gap of the Ru-Ir metal system.
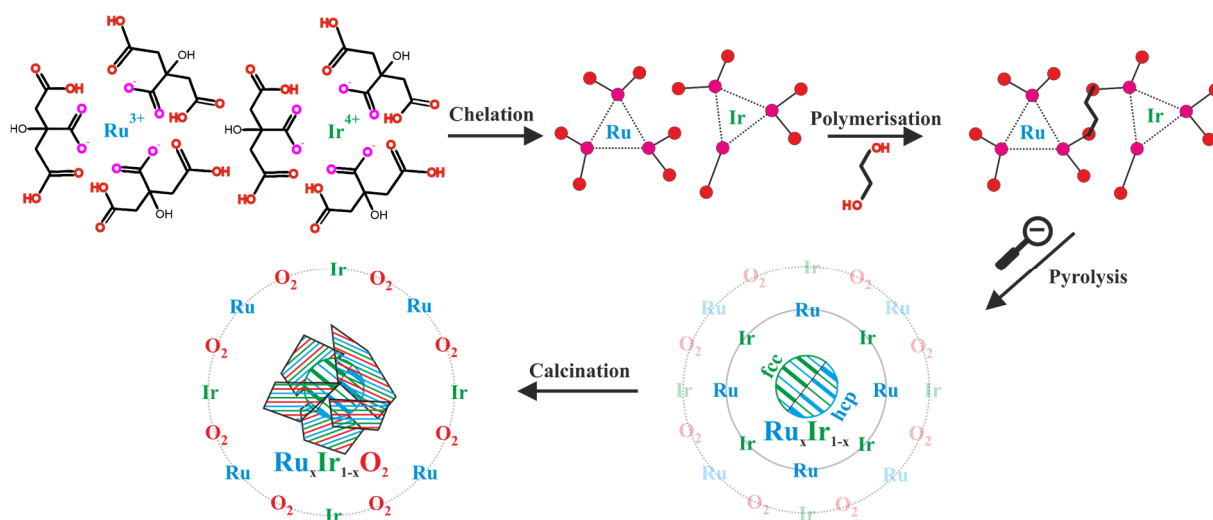
Figure 8.24: Reaction scheme that is based on ex-situ XRD, XPS, SEM, and TEM characterization. In the first step complexation of the metal cations takes place. Afterwards, polymerization is induced by adding ethylene glycol. The resulting resin is calcined at higher temperature (450 °C). In the beginning of the calcination step the reaction condition is reductive forming metallic cores of hcp or fcc structure depending on the metal concentrations. As soon as the environment of the metal cations is oxidizing, the oxide phase (rutile structure) grows on and encapsulates the metal particles.

At a later stage of the calcination, oxygen is able to permeate the polymer network and then the (mixed) oxide is formed in a net oxidizing atmosphere. Iridium is already in the correct oxidation state, but ruthenium needs to be oxidized formally from +3 to +4. The carbon backbone is oxidized to CO$_2$ and O$_2$ is reduced to form O^{2-} that is needed in the metal oxide formation. In this oxidation process, the previously formed metal particle serves as a nucleus for the preferential growth of the oxide so that finally the oxide particles encapsulate the metal core. The composition of the adhering Ru$_x$Ir$_{1-x}$O$_2$ particles is given by the local cation Ir^{4+} and Ru^{3+} concentrations. This agglomeration is clearly evidenced by the XPS (surface) and XRD

(bulk) experiments (**Figures 8.2, 8.6**) and the morphology is visualized by high-resolution TEM and SAED experiments (**Figures 8.12, 8.13, 8.14**).

The nominal composition x (given by employed weights of the precursors in the synthesis) is changed in 12.5 mol% steps from 0 mol% to 100 mol% with regard to Ru. The actual composition is quantified by various experimental methods including XRD-Vegard's rule, EDS-SEM, XPS and XRD-Rietveld that is summarized in **Figure 8.25**.
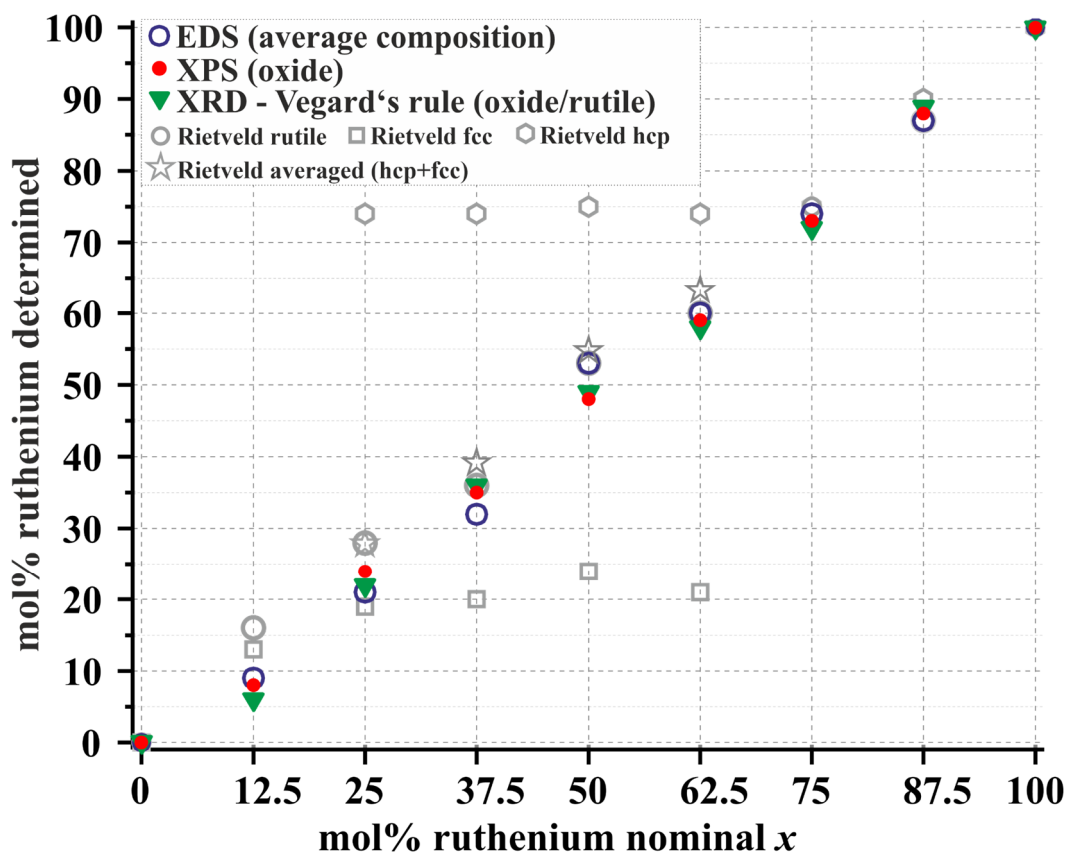
Figure 8.25: Summary of the derived Ru^{4+} content of the oxide phases by experimental data (XPS, EDS, Vegard's rule) and by Rietveld refinement. Furthermore, Rietveld refinement provide averaged metallic Ru content in alloy phases to check for the mass balance according to the level rule in the miscibility gap.

The mixed ruthenium-iridium powder samples form core shell agglomerates where the metal alloy core is encapsulated by mixed oxide particles. In principle, the composition can be different in the metal core and in the mixed oxide shell. However, this is not observed in the experiments due to mixing of the metal precursors on the microscopic scale in the Pechini method. With EDS the averaged composition in the powder is obtained. It turns out that the nominal composition x agrees remarkably well (**Figure 8.25**) with the actual mean compositions as derived by EDS, signifying the high degree of control during synthesis and that no material loss during same is observed. Furthermore, by this observation an accurate

determination of the amount of crystal water in the precursors (RuCl$_3 \cdot x$H$_2$O and IrCl$_4 \cdot x$H$_2$O) by thermogravimetric analyses (TGA experiments) can be confirmed, namely x=1 for IrCl$_4 \cdot x$H2O and x=3.5 for RuCl$_3 \cdot x$H$_2$O. The composition of the mixed oxide shell was determined by XPS. Again the derived compositions agree remarkably well with the nominal composition *x* (**Figure 8.25**), indicating the high degree of control on the surface composition. From these findings the averaged composition of the mixed metal core needs also to agree with the nominal composition *x*.

It is important that the metallic particles are encapsulated by oxide particles and not exposed to the reaction mixture. Otherwise, either the metal particles would also contribute to the reactivity, or these particles would oxidize under reaction conditions and thereby forming a mixed oxide surface with various compositions (the latter applies to the samples Ru_*x* with *x*=12.5 mol% up to 87.5 mol%). Altogether, this would blur a clear structure/activity correlation.

The composition of the mixed oxide phase can also be determined from Vegard's law that assumes that (at least) one cell parameter changes linearly with the composition when starting from pure RuO$_2$ to pure IrO$_2$. This may help experimentalist to check and quantify their actual composition of the sample, employing XRD data only. In the case of RuO$_2$ and IrO$_2$ only the lattice parameter *c* differs substantially, while the other two parameters *a* and *b* are virtually identical: *a=b*=4.5051, *c*=3.1586 for IrO$_2$ and *a=b*=4.4968, *c*=3.1049 for RuO$_2$.[131] The change in the *c* parameter affects the positions of the (101) reflections as can be seen in **Figure 8.26**.
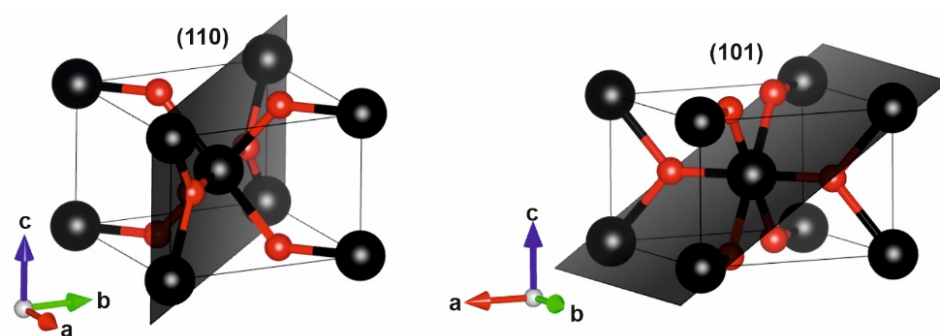
Figure 8.26: Visualization of (110) and (101) planes of the rutile structure. Since the (110) plane is parallel to the cell vector c, a variation of the unit cell parameter *c* does not alter the position of the (110) reflection in XRD. In contrast, a variation of the unit cell parameter *c* changes the position of (101) reflection.

Assuming the Vegard's law is fulfilled, the compositions can directly be derived from the experimentally observed shift of the (101) reflection in **Figure 8.27**. These Vegard-derived

composition values are also overlaid in **Figure 8.25** revealing a remarkable agreement with the EDS and the XPS-derived values, thus providing a high level of confidence to Vegard-derived composition values.
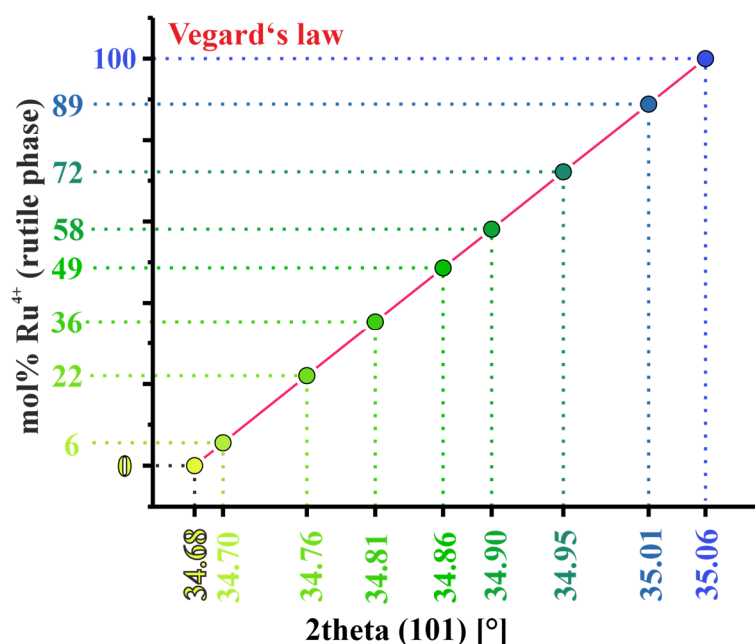
Figure 8.27: Determination of chemical composition of the mixed $Ru_xIr_{1-x}O_2$ oxides employing Vegard's law. Assuming a linear correlation of the Ru content and the position of (101) reflex, the actual chemical composition of the mixed $Ru_xIr_{1-x}O_2$ oxides can be quantified.

In a last step, the miscibility gap of the mixed Ru-Ir metal phase in the core of the secondary particle was subject to a Rietveld refinement based on the experimental XRD data in **Figure 8.2**. From Rietveld both the phase composition and the molar composition in the Ir-rich fcc and the Ru-rich hcp phase can be determined. These values are summarized in **Figures 8.3, 8.4**. For the mixed metal in the miscibility gap the composition of the Ir-rich phase and that of the Ru-rich phase is constant, namely hcp-$Ru_{0.74}Ir_{0.26}$ and fcc-$Ru_{0.21}Ir_{0.79}$. However, Rietveld analysis is also able to provide the weight% of hcp-$Ru_{0.74}Ir_{0.26}$ and fcc-$Ru_{0.21}Ir_{0.79}$ for each nominal composition x. As shown in **Figure 8.25** these weight% values translated into mol% values fulfill the level rule almost quantitatively.

For the mixed Ru_x samples metallic Ir is found in the XP spectra in the surface near region of the $Ru_xIr_{1-x}O_2$ samples and the concentration varies with the nominal composition x (**Figure 8.23**). The total amount of surface near metallic Ir is small, but significant and may be important for the catalytic performance since the concentration varies under reaction conditions (**Figure 8.23**).

For the (unsupported) mixed Ru_x powder samples we assume that the activity scales with the BET surface area. Therefore, the *STY* is normalized to the *BET* surface area, providing a kind of intrinsic activity. Since the *BET* values vary quite substantially among the ruthenium-iridium mixed oxide samples, the conversion *X* or the temperature at specific conversion values are not appropriate to assess the activity among the various mixed oxides. Rather, the temperature is considered at which a specific normalized *STY* is achieved, namely $1 \text{mmol·h}^{-1}\text{·m}^{-2}$ for oxidizing reaction conditions and $2 \text{mmol·h}^{-1}\text{·m}^{-2}$ for stoichiometric reaction conditions, as summarized in **Figure 8.28**; the lower the temperature value the higher the activity. Here a systematic variation among the various oxide compositions can be recognized. In the XPS experiments the Ru_x samples expose almost exclusively $Ru_xIr_{1-x}O_2$ mixed oxide (while the metallic core is encapsulated) so that all activity data can be considered as being from the mixed oxide only.

Pure RuO_2 is expected to be the best and IrO_2 to be the least active oxidation catalysts among the various mixed $Ru_xIr_{1-x}O_2$ oxides in the CO oxidation reaction. Indeed, pure IrO_2 is the least active catalyst. However, for the stoichiometric reaction mixture the most active oxidation catalyst turns out to be $Ru_{0.875}Ir_{0.125}O_2$ that is more active than pure RuO_2.

In **Figure 8.28** the apparent activation energies as a function of the nominal composition *x* are overlaid. In case of oxidizing conditions the apparent activation energies are around 112 ± 5 kJ·mol^{-1}, only pure RuO_2 indicates a substantially lower activation of about 90 kJ·mol^{-1}. In case of stoichiometric reaction conditions the gap between pure RuO_2 (71 kJ·mol^{-1}) and the mixed oxides (about 120 kJ·mol^{-1}) is even more pronounced. However, no systematics of the apparent activation energies is recognized, indicating that the apparent activation energy is not able to reflect the actual activity of a catalyst. In particular, the most active catalysts do not reveal the lowest apparent activation energy. In some cases ($CO:O_2 = 2:1$; composition region: x=50 mol% up to 87.5 mol%) even the opposite trend is observed. With a low apparent activation energy one has less control on the reaction rate by varying the temperature (Cremer-Constable compensation).

The presented unsupported $Ru_xIr_{1-x}O_2$ oxides for various compositions *x* are stable against chemical reduction as evidenced with XRD and XPS experiments after catalytic reaction, meaning that neither the bulk- nor the surface structure of the mixed oxides alters considerably. However, the surface composition of the mixed oxides is systematically enriched by Ir^{4+} of 5-10 mol% independent of the employed reaction condition (**Figure 8.21**). Obviously, the higher temperature during reaction drives the enrichment of Ir^{4+} in the near surface region.
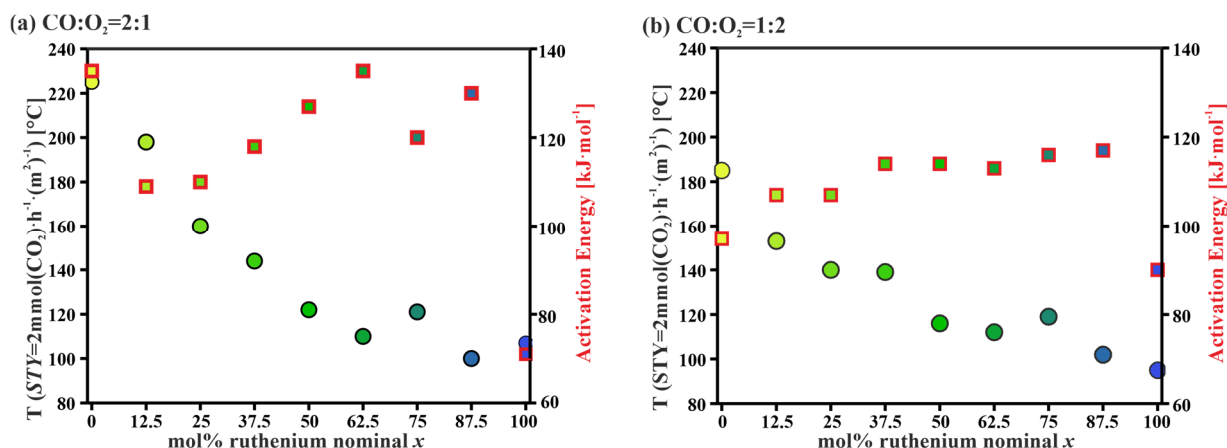
Figure 8.28: "Activity" versus nominal composition x of mixed $Ru_xIr_{1-x}O_2$ oxide catalyst in terms of apparent activation energy (squares) and temperature where the normalized *STY* (disks) is 2 mmol(CO_2)·h^{-1}·m^{-2}) and 1 mmol(CO_2)·h^{-1}·m^{-2} for a) CO:O_2=2:1 and b) CO:O_2=1:2, respectively.

Moreover, the amount of metallic Ir in the surface-near region is affected by the reaction mixture (**Figure 8.23**). Under oxidizing reaction conditions the amount of metallic surface Ir is significantly reduced and likely to be transformed to IrO_2. But this variation in metallic surface Ir is not able to explain the overall variation in oxidic Ir^{4+} in the surface near region. Under stoichiometric reaction conditions the amount of metallic surface Ir varies only little. In surface science experiments of pure single crystalline IrO_2(110) films the formation of metallic Ir islands on the IrO_2(110) surface is observed. These Ir metal islands are formed when the freshly prepared IrO_2(110) is annealed to 600 K under ultrahigh vacuum conditions.[219,220]

Up to date, no activity experiments for the $Ru_xIr_{1-x}O_2$ mixed oxide catalysts including pure IrO_2 have yet been reported in the literature. However, for RuO_2-based catalysts there are various kinetic studies for the CO oxidation reaction over RuO_2 powder[221,222] and supported RuO_2 catalysts[223-225] with which our data can be compared. The apparent activation energy reported in the literature is about 85 kJ·mol^{-1} independent of the reaction mixture and the used catalyst, while the apparent activation energies for RuO_2 found in this thesis are 71 kJ·mol^{-1} and 90 kJ·mol^{-1} for stoichiometric and oxidizing reaction conditions, respectively. However, the preparation of the catalysts presented in this work is different. In the mentioned literature, prior to the catalytic tests both RuO_2 powder and supported RuO_2 samples are first chemically reduced by hydrogen treatment and subsequently mildly re-oxidized so that a thin RuO_2 covering the Ru metal core is assumed be the catalytically active phase. This difference in catalyst formation may be the reason for the observed differences in apparent activation energies. Additionally, the intermediate population may depend on the partial pressures and therefore affect the apparent activation energies differently, which is why the activation barriers during experiments with differing gas mixtures may not be directly comparable.

8.2 Ru$_x$Ir$_{1-x}$O$_2$ & Ru$_x$Ir$_{1-x}$O$_2$@TiO$_2$ Applied to Methane Combustion

8.2.1 Synthesis of Ru$_x$Ir$_{1-x}$O$_2$@TiO$_2$

The supported Ru$_x$Ir$_{1-x}$O$_2$@TiO$_2$ were synthesized with a little modification of the Pechini route,[176] adding pure rutile-TiO$_2$ (<100nm) before complexation of the ruthenium- and iridium-cations by citric acid. Based on surface studies of RuO$_2$ and IrO$_2$ on rutile TiO$_2$(110) rutile TiO$_2$ is chosen as the carrier as a high dispersion of Ru$_x$Ir$_{1-x}$O$_2$ is expected.[219,226] The added rutile-TiO$_2$ support particles are trapped in the carbon network after polymerization of citric acid and ethylene glycol. The ruthenium and iridium cations either nucleate directly on the support surface or mixed ruthenium-iridium particles nucleate first and adhere then to the support, forming highly dispersed supported ruthenium-iridium mixed particles after final calcination.

Analogous to the unsupported materials, which are referred to as Ru_x, the supported samples are referred to as Ru_x@TiO$_2$ with x being the nominal composition of ruthenium in mol% changing from 0 mol% to 100 mol% in steps of 25 mol% (pure iridium sample is referred to as Ir_100@TiO$_2$ instead of Ru_0@TiO$_2$). The relative amount of active component with respect to the support is chosen to be 5 mol%. This amount represents a reasonable compromise for having enough active component for in-depth characterization and catalytic measurements, while being low enough to ensure that most of the active component is supported on rutile TiO$_2$.

The preparation of Ru_x@TiO$_2$ with a nominal composition of x=50 mol% is explained by way of example: 0.3125 mmol of RuCl$_3$·3.5H$_2$O precursor and 0.3125 mmol of IrCl$_4$·H$_2$O precursor are dissolved in water. Subsequently, 12.5 mmol (1 g) of TiO$_2$ are added and the resulting suspension is stirred vigorously. 31 mmol of citric acid monohydrate are added to the solution, the mixture is stirred for another 30 min to ensure complete dissolution of the acid and then is mildly heated up to 60 °C to accomplish the complete complexation of the metal cations. Afterwards 94 mmol ethylene glycol are added and the mixture is heated to 100 °C with maximum heating power to induce sudden polymerization/polycondensation. As soon as most of the solvent is evaporated, the resulting black resin is transferred to a crucible and is subjected to a high temperature treatment at 450 °C for 12 h with a heating rate of 1 K·min^{-1} under atmospheric condition. The obtained supported ruthenium-iridium mixed oxide samples are grinded for the analytics and catalytic experiments.

8.2.2 Characterization of $Ru_xIr_{1-x}O_2@TiO_2$

With XPS the actual surface-near composition of the supported ruthenium-iridium catalysts ($Ru\_x@TiO_2$) for varying nominal composition x is investigated and shown in **Figure 8.29**. In the given spectra the background and the C 1s component are subtracted for clarity reasons. From the energetic positions of the main components in the Ru 3d spectra (**Figure 8.29a**) it can be clearly concluded that ruthenium is always in the 4+ oxidation state with no sign of metallic Ru (**Figure 8.29c**). The Ir 4f spectra are dominated by Ir^{4+} (**Figure 8.29b**) but exhibit some minor contribution of metallic Ir (**Figure 8.29c**) similar to the results of the unsupported ruthenium-iridium mixed oxides (**Figures 8.8, 8.9**) interpreted in terms of core-shell particles with a mixed oxide shell fully covering a mixed metal core. Therefore, the observed methane combustion activity is solely ascribed to the mixed oxide phase. In **Figure 8.29c** detailed deconvolutions of experimental Ru 3d and Ir 4f XP spectra are shown exemplarily for the $Ru\_25@TiO_2$ sample; the deconvolution of the remaining samples can be found in **Figure 8.30** with the corresponding fitting parameters compiled in **Table 8.11**.
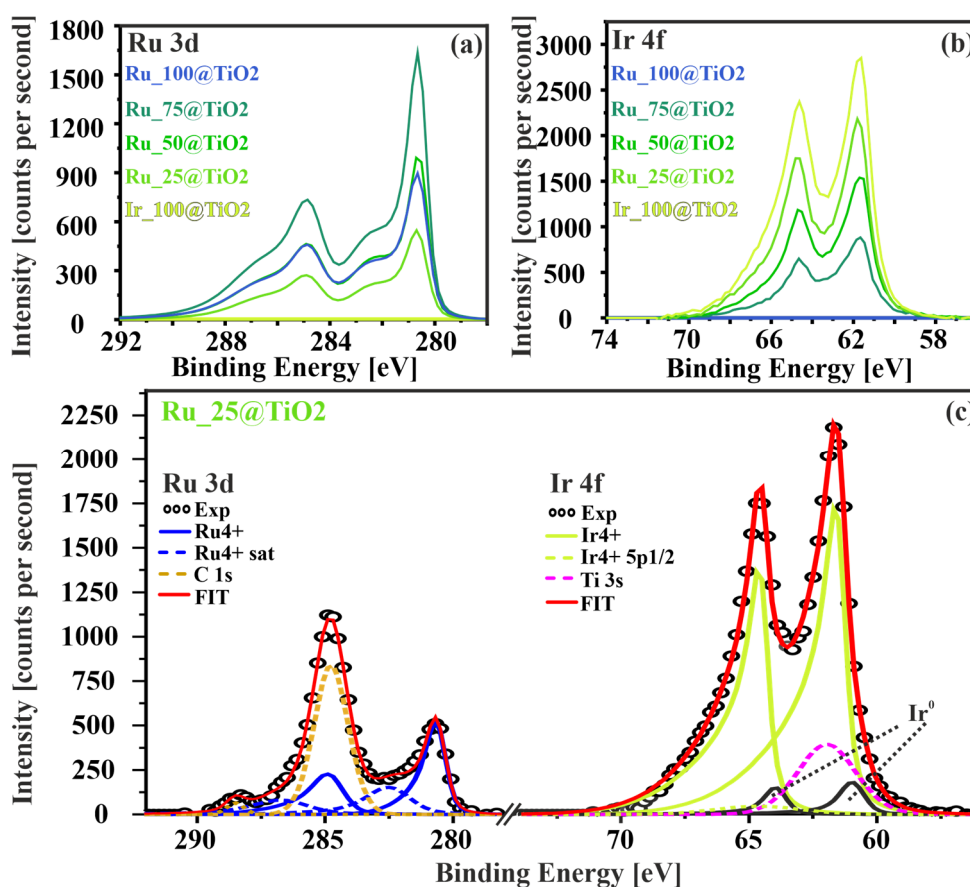
Figure 8.29: XP spectra of $Ru\_x@TiO_2$ samples in the spectral region of Ru 3d (a) and Ir 4f (b). The Ru 3d spectra shown are derived by subtracting the background as well as the C 1s signal derived by deconvolution using the CASAXPS software. The Ir 4f spectra have been derived by subtracting the background. c) Deconvolution of the Ru 3d and Ir 4f spectra exemplified with the $Ru\_25@TiO_2$ sample. Both spectra have identical intensity axis, thus emphasizing the relative intensity of Ru 3d and Ir 4f.
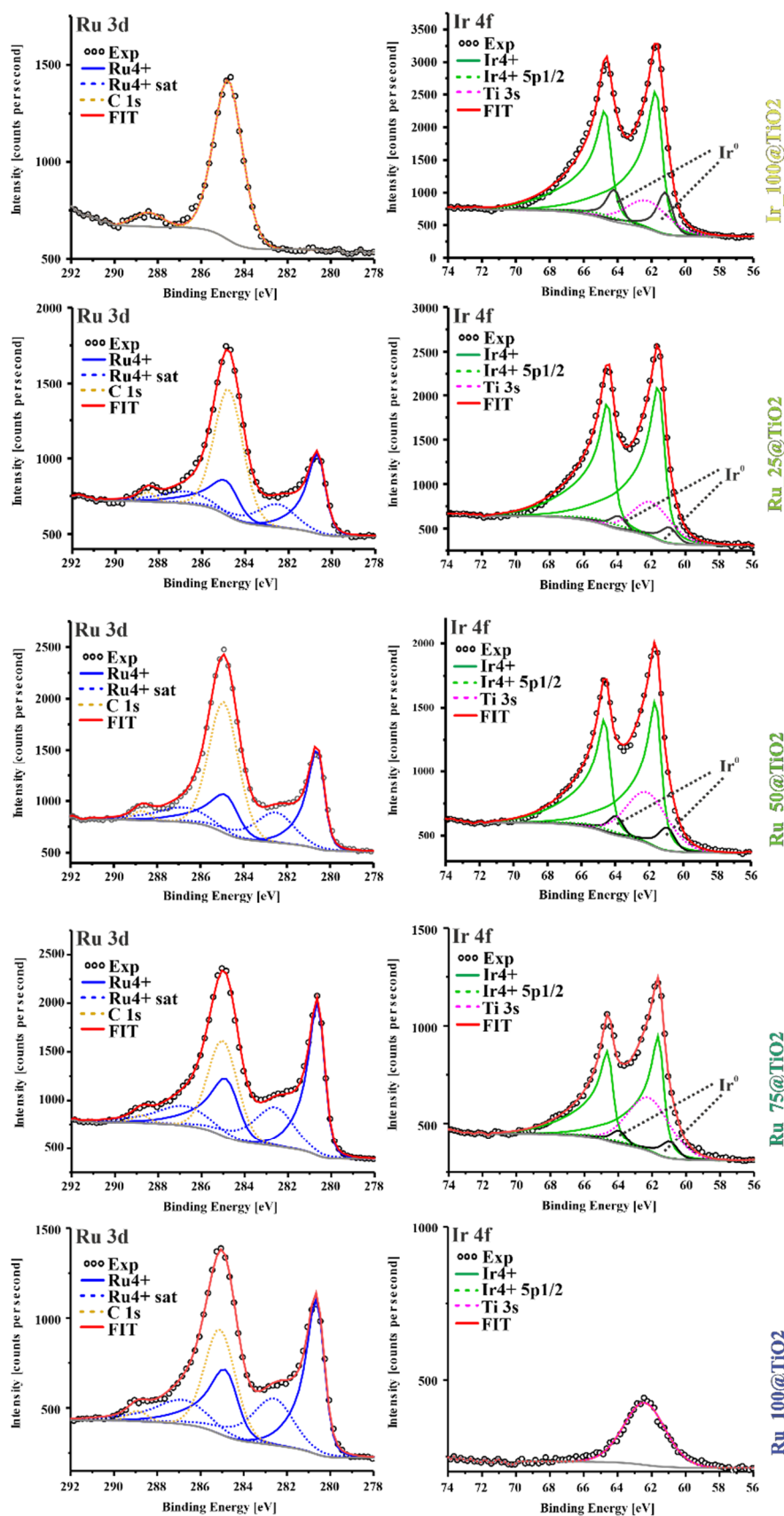
Figure 8.30: Deconvolution of XP spectra of supported ruthenium-iridium mixed oxide samples as prepared, showing Ru 3d on the left and Ir 4f spectra on the right. The deconvolution reveals Ru^{4+} and Ir^{4+} as the main components. While the Ir 4f spectra reveal metallic Ir as a minor component the Ru 3d spectra indicate no sign of metallic Ru similar to the unsupported samples (Figure 8.9).

Table 8.11: CASAXPS fitting parameters for supported ruthenium-iridium mixed oxide samples referred to as Ru_x@TiO$_2$.

Ru3d	Ir_100@TiO₂	Ir_25@TiO₂	Ir_50@TiO₂	Ir_75@TiO₂	Ru_100@TiO₂
BE [ev] Ru3d-5/2	-	280.6	280.5	280.6	280.5
FWHM	-	0.9	0.8	0.8	0.9
Line Shape	LF(0.4,1,45,280)				
BE [ev] Ru3d-3/2	-	284.7	284.7	284.7	284.7
FWHM	-	1.4	1.4	1.4	1.4
Line Shape	LF(0.4,1,45,280)				
BE [ev] Ru3d-5/2 sat	-	282.4	282.4	282.5	282.5
FWHM	-	2.0	2.0	2.0	2.1
Line Shape	LF(0.6,1,45,280)				
BE [ev] Ru3d-3/2 sat	-	286.6	286.6	286.6	286.7
FWHM	-	2.5	2.6	2.7	2.7
Line Shape	LF(0.6,1,45,280)				
BE [ev] C1s (C-C)	284.8	284.8	285.0	285.0	285.0
FWHM	1.6	1.6	1.6	1.6	1.7
Line Shape	GL(30)				

Ir4f	Ir_100@TiO₂	Ir_25@TiO₂	Ir_50@TiO₂	Ir_75@TiO₂	Ru_100@TiO₂
BE [eV] Ir4f-7/2	61.7	61.5	61.6	61.6	-
FWHM	0.9	0.9	0.8	0.8	-
Line shape	LF(0.3,1,60,100)				
BE [eV] Ir4f-5/2	64.6	64.5	64.6	64.6	-
FWHM	0.9	0.9	0.8	0.8	-
Line shape	LF(0.3,1,60,100)				
BE [eV] Ir5p-1/2	64.8	64.6	64.7	64.8	-
FWHM	3.9	3.9	3.9	3.9	-
Line Shape	GL(30)				
BE [eV] Ti3s	62.2	62.0	62.1	62.1	62.4
FWHM	2.9	2.7	2.8	2.9	2.9
Line shape	GL(30)				

Within the XP spectra of a single sample, the intensities of Ru 3d and Ir 4f are strictly correlated so that from these spectra the mean ruthenium and iridium composition as well as the composition x of the mixed oxide component $Ru_xIr_{1-x}O_2@TiO_2$ of each sample can be determined quite accurately with the CASAXPS software, recalling that the active components form solid solutions as for the unsupported system. For determining the mean composition, the integral intensity of Ru 3d and Ir 4f (without C 1s in case of Ru 3d and without Ti 3s in case of Ir 4f as well as without the background in both cases) are used, while for determining the composition x of the mixed oxide, only the integral intensity of Ru^{4+} 3d and Ir^{4+} 4f are taken.

The thus estimated compositions remarkably agree with the nominal composition as given by the molar ratio of the used precursors in the synthesis (**Table 8.12**), emphasizing the high level of control of the composition of the supported mixed oxides.

However, the intensities among the Ru 3d and Ir 4f of different samples are not strictly correlated due to slightly varying experimental conditions and to varying dispersion of the active component supported on the rutile-TiO_2. Yet, a comparison among the experimental Ru 3d and Ir 4f spectra in **Figure 8.29a**,**b** reveals that the intensity variation among the Ru 3d (Ir 4f) spectra qualitatively reflects the concentration of the nominal ruthenium (iridium) of all samples, but the pure Ru_100@TiO_2, whose intensity is close to that of Ru_50@TiO_2.

Table 8.12: XPS analysis: Mean composition (independent of oxidation state) of the Ru_x@TiO_2 samples, composition of the oxide component ($Ru_xIr_{1-x}O_2$@TiO_2), and the overall noble metal (ruthenium + iridium) content given in mol% with respect to the support material TiO_2. Exemplarily, a detailed quantification procedure for the Ru_50@TiO_2 sample is given in Table 8.13.

nominal	mean composition (independent of oxidation state)			mixed rutile oxide composition	
x (Ru_x@TiO_2) [mol%]	Ir/(Ir+Ru) [mol%]	Ru/(Ir+Ru) [mol%]	(Ru+Ir)/ (Ru+Ir+Ti) [mol%]	$Ir^{4+}/(Ir^{4+}+Ru^{4+})$ [mol%]	$Ru^{4+}/(Ir^{4+}+Ru^{4+})$ [mol%]
0	100	0	24	100	0
25	78	22	23	76	24
50	56	44	17	54	46
75	28	72	19	24	76
100	0	100	14	0	100

Table 8.13: Exemplified CASAXPS quantification values for Ru_50@TiO_2 sample.

peak	Position	Area	R.S.F	Atom%	mean comp.	oxide comp.
Ir4+ 4f 7/2	61.7	135.75	6.365	0.9	**iridium/(iridium+ruthenium)** =0.56	$Ir^{4+}/(Ir^{4+}+Ru^{4+})$ =0.54
Ir4+ 4f 5/2	64.7	101.72	6.365	0.6		
Ir0 4f 5/2	61.0	17.26	6.365	0.1		-----------------
Ir0 4f 5/2	64.0	12.93	6.365	0.1		-----------------
Ru4+ 3d 5/2	280.5	63.41	5.139	0.5	**ruthenium/(iridium+ruthenium)** =0.44	$Ru^{4+}/(Ir^{4+}+Ru^{4+})$ =0.46
Ru4+ 3d 3/2	284.7	42.40	5.139	0.3		
Ru4+ 3d 5/2 sat.	282.4	41.40	5.139	0.3		
Ru4+ 3d 3/2 sat.	286.6	27.70	5.139	0.2		

The experimental spectra can, however, be normalized to the integral Ti 2p (**Figure 8.31a,b**) intensity and additionally to the actual concentration of iridium and ruthenium as shown in **Figure 8.31c,d**. From these normalized spectra one can determine the relative near-surface amount of the active component (Ru+Ir)/(Ru+Ir+Ti) that nominally should be 5 mol%. In

Table 8.14 it can be clearly seen that these values are several times higher than 5 mol%, thus indicating substantial dispersion of the active component. Also obvious from these values is that the dispersion of pure Ru_100@TiO$_2$ is the lowest among the other mixed samples Ru_x@TiO$_2$. In **Table 8.15** the individual dispersion values of ruthenium (Ru/(Ru+Ti)/(Ru/(Ir+Ru))) and iridium (Ir/(Ir+Ti)/(Ru/(Ir+Ru))) are calculated which correspond to the normalized spectra shown in **Figure 8.31c,d**. The values in **Table 8.15** show that the ruthenium and iridium dispersion are nearly identical within the same sample, indicating strong evidence for solid solutions.
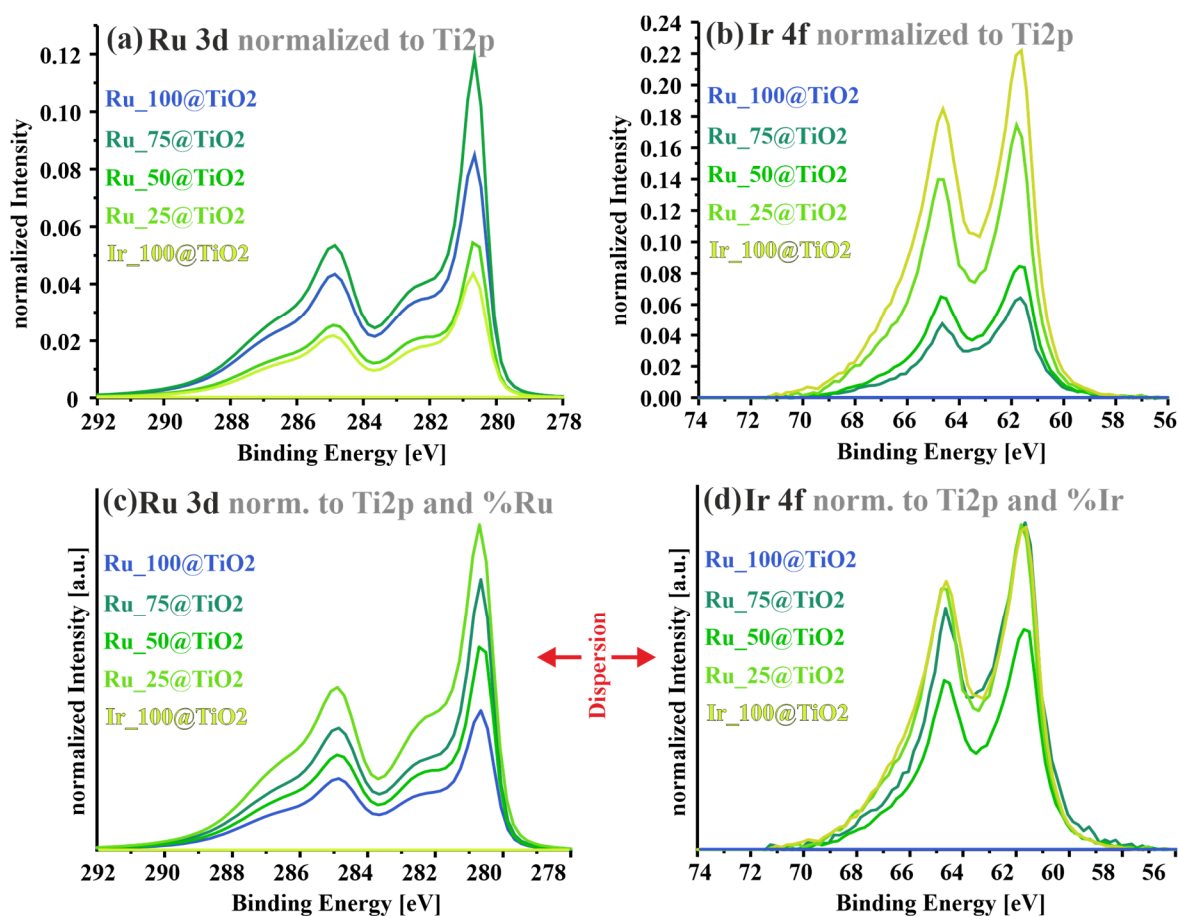
Figure 8.31: Ru 3d (left) and Ir 4f (right) XP spectra of Ru_x@TiO$_2$ samples normalized to integral intensity of Ti 2p (**Figure 8.31a,b**) and to the actual relative ruthenium (iridium) concentration (revealed by deconvolution) given in **Figure 8.31c,d**. The Ru 3d spectra are derived by subtracting the C 1s signal as well as the background (including only the Ru 3d main peaks and Ru 3d satellite peaks) before normalization, while in the Ir 4f spectra only the background needed to be subtracted (including only Ir 4f, Ir 5p1/2 and Ti 3s features). Since the signals shown in **Figure 8.31c,d** are not only normalized to the support but also to the noble metal concentration they include only information about the dispersion of the corresponding noble metal ruthenium (iridium). The revealed relative dispersion is in good agreement with the CO uptake results given in Table 8.17 with highest dispersion for Ir_100@TiO$_2$ and Ru_25@TiO$_2$ followed by the Ru_75@TiO$_2$ sample. The Ru_50@TiO$_2$ sample turns out to have a lower dispersion, but still higher than that of pure Ru_100@TiO$_2$.

Table 8.14: Loadings of ruthenium and iridium of Ru_x@TiO$_2$ samples relative to the support material TiO$_2$ as quantified by CASAXPS. The expected nominal values are shown in brackets. All values are several times higher than the nominal values, thus indicating high dispersion.

nominal	loading (nominal loading)		
x (Ru_x@TiO$_2$) [mol%]	Ru/(Ru+Ti) [mol%]	Ir/(Ir+Ti) [mol%]	(Ru+Ir)/(Ru+Ir+Ti) [mol%]
0	-	24 (5)	24 (5)
25	7 (1.25)	19 (3.75)	23 (5)
50	8 (2.5)	10 (2.5)	17 (5)
75	14 (3.75)	6 (1.25)	19 (5)
100	14 (5)	-	14 (5)

Table 8.15: Ruthenium (iridium) dispersion quantified by normalizing the data from **Table 8.14** to the relative amount of ruthenium (iridium) as determined by deconvolution (**Table 8.12**). Within the error bars ruthenium and iridium dispersions are identical, providing strong evidence for the formation of mixed ruthenium-iridium solid solutions.

nominal	ruthenium dispersion	iridium dispersion
x (Ru_x@TiO$_2$) [mol%]	Ru/(Ru+Ti) / Ru/(Ir+Ru)	Ir/(Ir+Ti) / Ir/(Ir+Ru)
0	-	0.24±0.02
25	0.29±0.02	0.24±0.02
50	0.18±0.02	0.17±0.02
75	0.20±0.02	0.21±0.02
100	0.14±0.02	-

With powder XRD the structure of the supported catalysts (**Figure 8.32a**) is examined. The XRD scans are governed by the rutile-TiO$_2$ support, but there is also a faint but clearly visible (101) reflection of mixed ruthenium-iridium oxide that shifts with increasing ruthenium concentration to higher diffraction angles. In order to be able to quantify this shift, LaB$_6$ with its sharp reflections to calibrate the 2-theta axis is employed. This allows to determine the chemical composition of the mixed ruthenium-iridium oxide utilizing a Vegard plot as shown in **Figure 8.32b**.
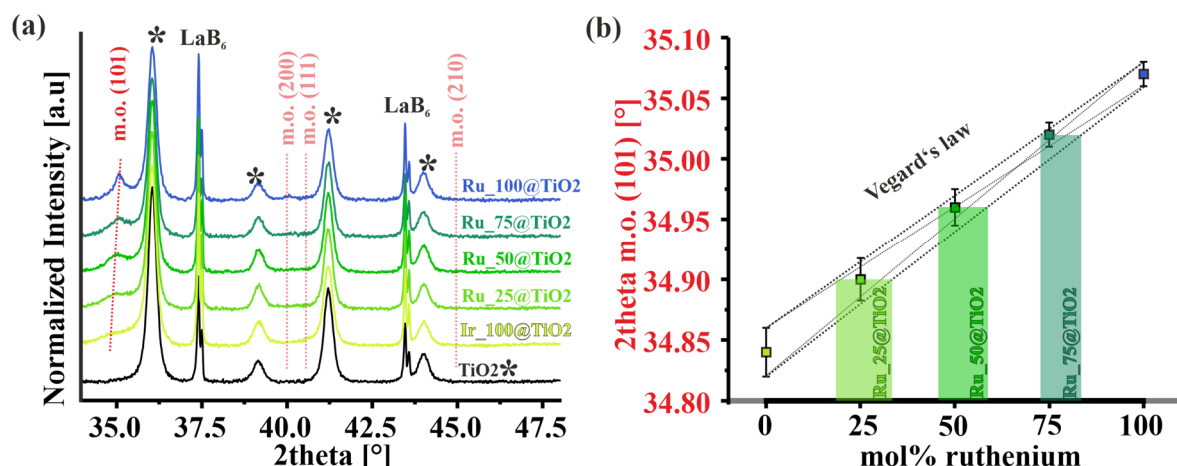
Figure 8.32: XRD patterns of supported Ru_x@TiO$_2$ samples normalized to TiO$_2$(101) reflection. LaB$_6$ is added for calibrating the 2theta axis. The (101) reflection of ruthenium-iridium mixed oxide is indicated. Growth and sharpening of the (101) reflection with higher amount of ruthenium evidence that the particle size increases with higher ruthenium content. All reflections which are marked with * belong to the pure support material rutile TiO$_2$. The (101) diffraction line is the only clearly visible one for the mixed $Ru_xIr_{1-x}O_2$ oxide (m.o) component in the shown 2theta range. The (200) at about 40.0°, the (111) at about 40.5° and the (210) at about 45.0° of the mixed $Ru_xIr_{1-x}O_2$ oxide are buried in the background noise since all these diffraction lines have one to three orders of magnitude lower intensities.

Table 8.16: XRD analysis: Composition of the oxide component ($Ru_xIr_{1-x}O_2@TiO_2$) of the supported ruthenium-iridium mixed oxide materials derived by Vegard's law as well as the full width half maximum (*FWHM*) indicating bigger crystallites (Scherrer equation) with higher content of ruthenium. The XRD results are compared to the average particle size as obtained from TEM pictures.

@TiO$_2$	Ir_100@	Ru_25@	Ru_50@	Ru_75@	Ru_100@
x ($Ru_xIr_{1-x}O_2@TiO_2$)	0	0.28±0.07	0.53±0.06	0.79±0.05	1
FWHM [°2Theta]	1.2	1.1	0.9	0.8	0.4
XRD: Crystallite size [nm]	7	8	10	11	22
TEM: Particle size [nm]	4	5	6	6	11

The composition values derived by the Vegard plot together with the full width half maximum (*FWHM*) of the (101) reflection of the mixed oxide and the particle sizes derived from the Scherrer equation are collected in **Table 8.16**. The *FWHM* decreases considerably with the chemical composition x ($Ru_xIr_{1-x}O_2@TiO_2$), that is associated with an increase of the size of the ruthenium-iridium mixed oxide particles. For Ir_100@TiO$_2$ the crystallite size is the smallest with 7 nm, while with increasing ruthenium concentration the crystallite size steadily increases to 11 nm for Ru_75@TiO$_2$. This size effect is most prominent with the pure RuO$_2$@TiO$_2$ system (referred to as Ru_100@TiO$_2$) with a crystallite size of 22 nm. However, XRD overestimates the size of particles in that already small concentrations of large particles may dominate the XRD scans, while diffraction from small particles contribute mainly to the background intensity. Therefore, a microscopic technique, such as TEM is needed to countercheck for the size of supported particles (**Figures 8.33**, **8.34**).
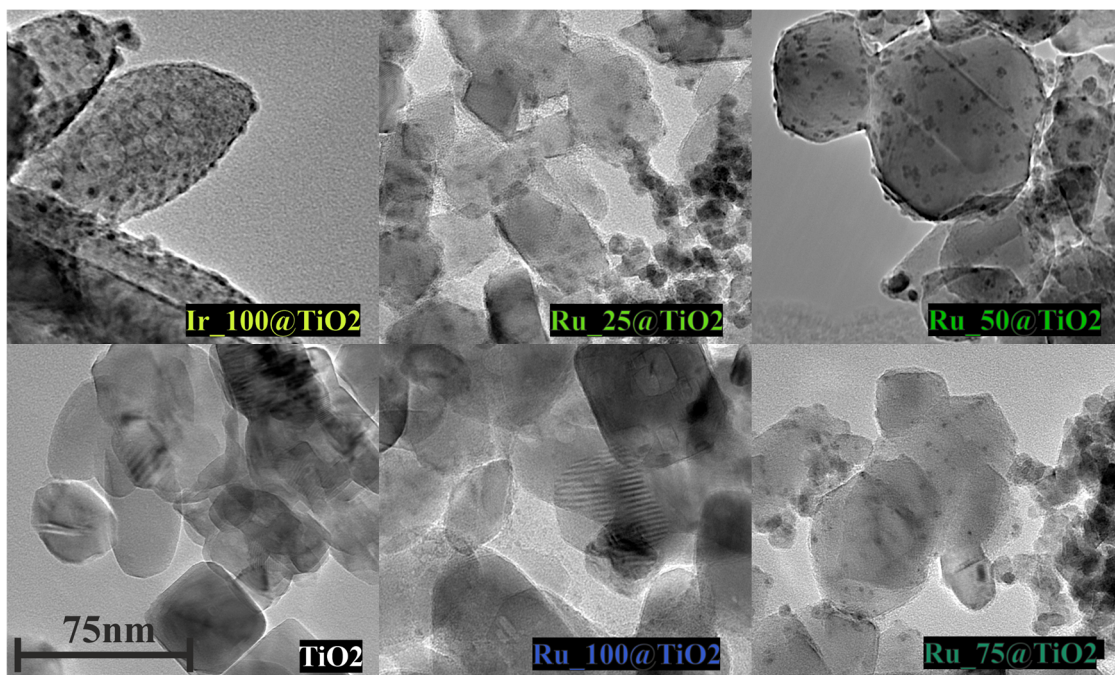
Figure 8.33: TEM images of as prepared Ru_x@TiO$_2$ samples at a magnification of 110,000 revealing high dispersion with a narrow size distribution for pure Ir_100@TiO$_2$. In the pure Ru_100@TiO$_2$ sample hardly any supported material can be discerned. The mixed supported oxides show a high dispersion of the active component on the support surface with a trend of increasing dispersion with higher amount of iridium. Overview TEM micrographs of lower magnification are presented in **Figure 8.34**.
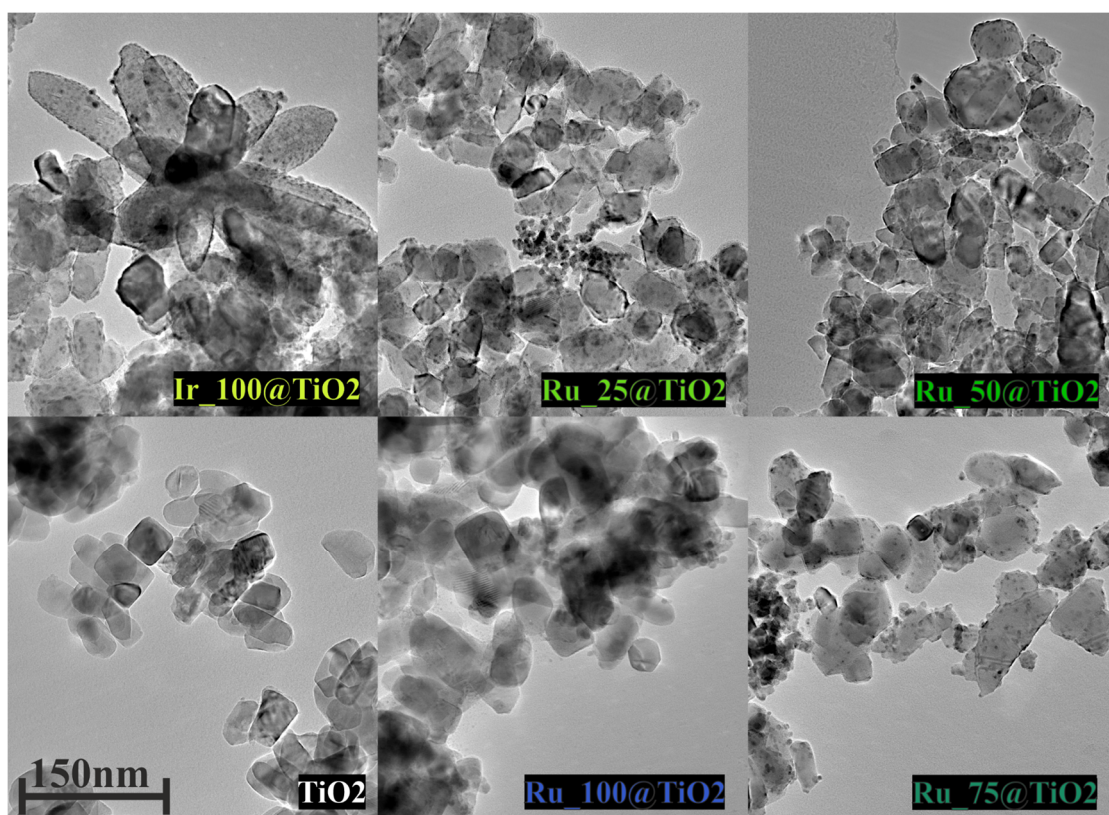
Figure 8.34: TEM images of as prepared Ru_x@TiO$_2$ samples at a magnification of 43,000. Pure Ru_100@TiO$_2$ sample does not show any supported RuO$_2$ particles. The RuO$_2$ seem to form own larger and separated particles/agglomerates.

In the TEM images shown in **Figure 8.33**, it can be seen that the dispersion of the supported mixed ruthenium-iridium particles varies with composition. For the case of Ir_100@TiO$_2$, clearly many supported particles are discernible with a narrow size distribution. Quite in contrast, pure Ru_100@TiO$_2$ does not show any sign of supported particles. Instead, most of RuO$_2$ forms unsupported particles as shown with element mapping (**Figure 8.35**) In between these extremes supported particles are clearly visible, but it is also obvious that its concentration decreases with increasing ruthenium content. In **Table 8.16** the average particle sizes derived from TEM images in **Figure 8.33** are summarized. The particles size from TEM is systematically smaller than the XRD-derived ones that is explainable since XRD intensities are dominated by the bigger particles.
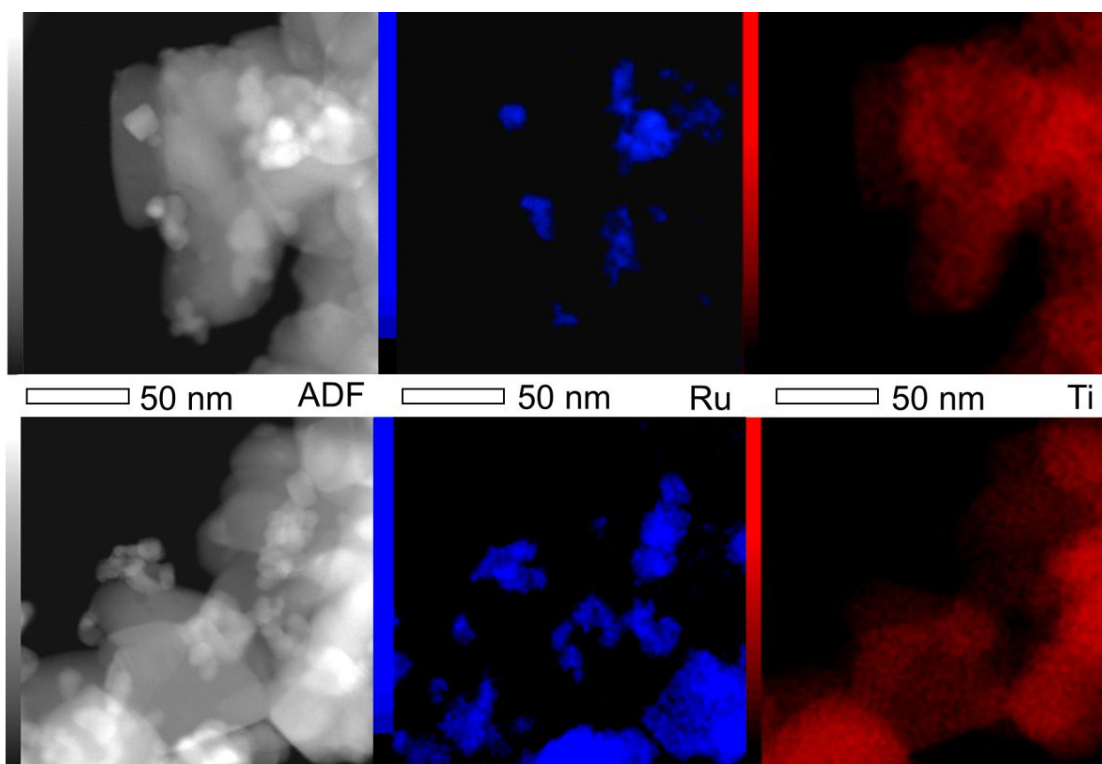
Figure 8.35: ADF-STEM images and corresponding EDS-elemental mapping of the Ru_100@TiO$_2$ sample revealing that most of ruthenium forms unsupported agglomerates.

High resolution STEM together with element mapping supports this view. For pure Ir_100@TiO$_2$ there is no indication that unsupported IrO$_2$ particles are formed, while already for the Ru_25@TiO$_2$ agglomeration of mixed ruthenium-iridium particles is apparent (**Figure 8.36**), although most of the particles adhere to the rutile TiO$_2$ support particles. Element mapping in **Figure 8.36** reveals that all supported particles comprise a mixture of ruthenium and iridium; with 30±10 mol% ruthenium that is reconciled with the nominal concentration of 25 mol% ruthenium. A segregation of ruthenium and iridium into RuO$_2$ and IrO$_2$ can be ruled

out since XRD reveals an average crystallite size of 8 nm (**Table 8.16**) for the active component in Ru_25@TiO$_2$ and such big particles of pure RuO_2 and IrO_2 conflicts with the identical intensity distribution of ruthenium and iridium in the EDS mappings.
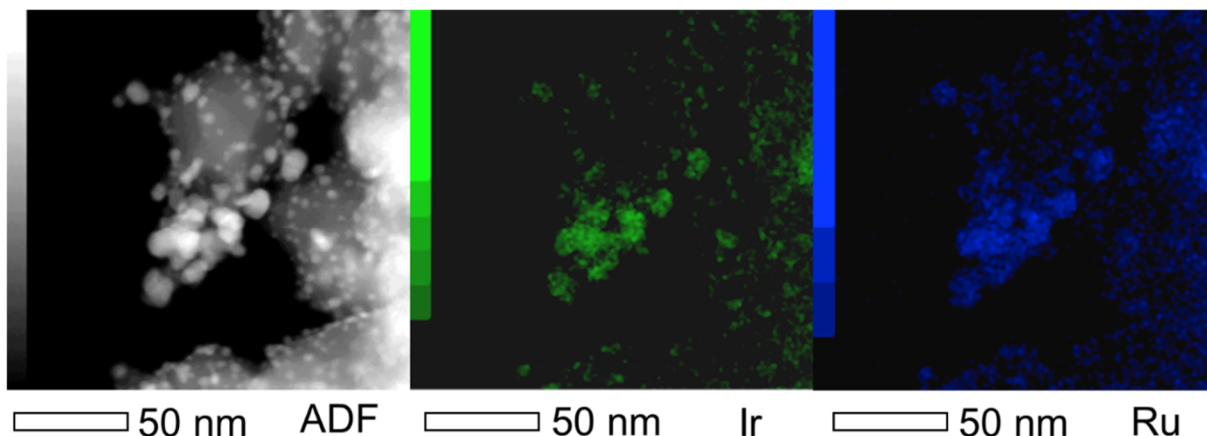
Figure 8.36: Annular dark field image and EDS-elemental mapping of the Ru_25@TiO$_2$ sample, indicating that the small particle on the surface of TiO$_2$ support consist of a mixture of ruthenium and iridium with 30±10 mol% ruthenium, roughly in agreement with the nominal composition (25 mol% ruthenium).

For the comparison of activity data among various supported Ru_x@TiO$_2$ samples it is required that the space time yield *STY* is normalized to the active surface area. For the unsupported ruthenium-iridium mixed oxide samples this is accomplished by measuring the *BET* surface area. However, for supported catalysts this approach is not reasonable since the catalytically inactive support dominates the *BET* values. Therefore, the relative active surface area is measured by CO-uptake experiments, assuming that the number of adsorbed CO molecules is strictly correlated with the number of active sites (#*a.s.*) of the active component and independent of the actual composition of the mixed oxide catalyst. In **Table 8.17** these experimental results are summarized.

Table 8.17: Number of active sites (#*a.s.*) of supported Ru_*x*@TiO$_2$ derived by CO-pulse experiments normalized to the catalyst's mass and to the amount of active component given in mol. In addition, the *BET* surface areas are provided.

sample	#*a.s.*/m_{cat} [μmol·g^{-1}]	#*a.s.*/$n_{a.c.}$ [mmol·mol^{-1}]	*BET* [m^2·g^{-1}]
Ir_100@TiO$_2$	103±1	164	19
Ru_25@TiO$_2$	82±1	130	12
Ru_50@TiO$_2$	54±4	86	23
Ru_75@TiO$_2$	60±3	96	17
Ru_100@TiO$_2$	82±6	131	17

As suggested by HRTEM and XRD, the active surface areas of Ir_100@TiO$_2$ and Ru_25@TiO$_2$ are the highest, while the ones of Ru_50@TiO$_2$ and Ru_75@TiO$_2$ are the lowest. Quite surprisingly, the active surface area of Ru_100@TiO$_2$ is quite high and apparently conflicts with the large average RuO$_2$ particle size of 22 nm as derived from XRD. However, advanced HRTEM experiments reveal that the TiO$_2$ particles are partly covered by a thin RuO$_2$ layer of 1-2 nm thickness shown in **Figure 8.37**. These layers are likely to be responsible for the observed high active surface area, but do not contribute to XRD pattern. However, most of the RuO$_2$ agglomerates, forming larger particles that do not adhere to the TiO$_2$ support (**Figure 8.35**). These larger RuO$_2$ agglomerates are responsible for the sharp (101) reflection in XRD (**Figure 8.32a**) that corresponds to an averaged single crystalline particle size in the agglomerate of 22 nm (**Table 8.16**).
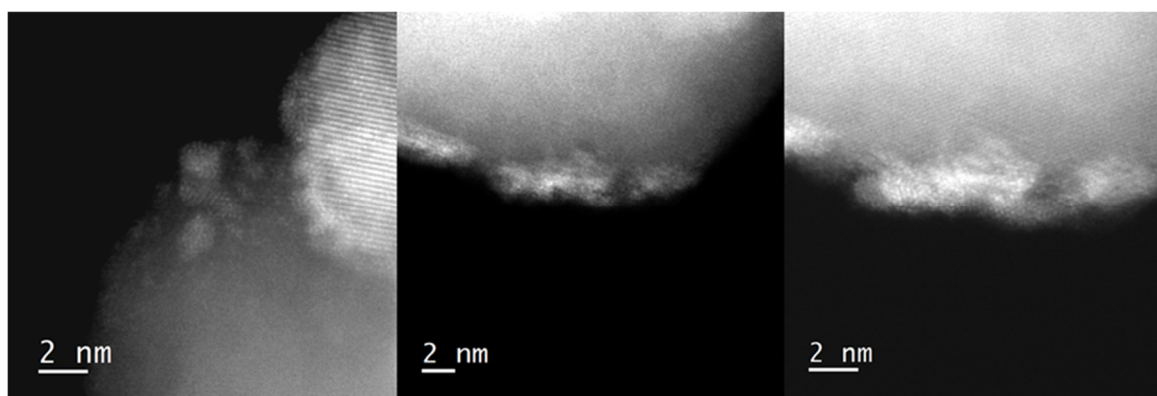
Figure 8.37: ADF-STEM pictures of the Ru_100@TiO$_2$ sample showing thin (1-2 nm thick) layers of RuO$_2$ on the support material.

8.2.3 Catalytic Methane Combustion

Figure 8.38 summarizes the light-off curves of methane combustion over supported catalysts Ru_x@TiO$_2$ with varying composition x; in **Figure 8.38a** the original experimental data are shown, while in **Figure 8.38b** the light-off curves are normalized to the number of active sites from **Table 8.17**. In the light-off experiments the temperature is linearly ramped with 1 K·min^{-1} up to *T10* where the conversion *X* of the methane combustion reaction reaches 10% with a reaction feed of 2 sccm methane and 8 sccm O$_2$ balanced by 90 sccm N$_2$; generally the temperature sweep needs to be low enough to maintain steady state conditions during the temperature ramp. These light-off temperatures *T10* as well as *T2* (*X*=2%) and *T5* (*X*=5%) values are collected in **Table 8.18**. Ru_100@TiO$_2$ with RuO$_2$ as the active component clearly reveals the lowest activity in methane combustion. However, it is equally evident that not the pure Ir_100@TiO$_2$ (with IrO$_2$ as the active component) but rather Ru_25@TiO$_2$ is the most

active catalyst in methane combustion for conversions lower than 10%. When normalizing the activity data to the number of active sites (**Figure 8.38b**), $Ir\_100@TiO_2$, $Ru\_50@TiO_2$, and $Ru\_75@TiO_2$ show similar activity that is substantially higher than pure $Ru\_100@TiO_2$, but still significantly lower than that of $Ru\_25@TiO_2$.
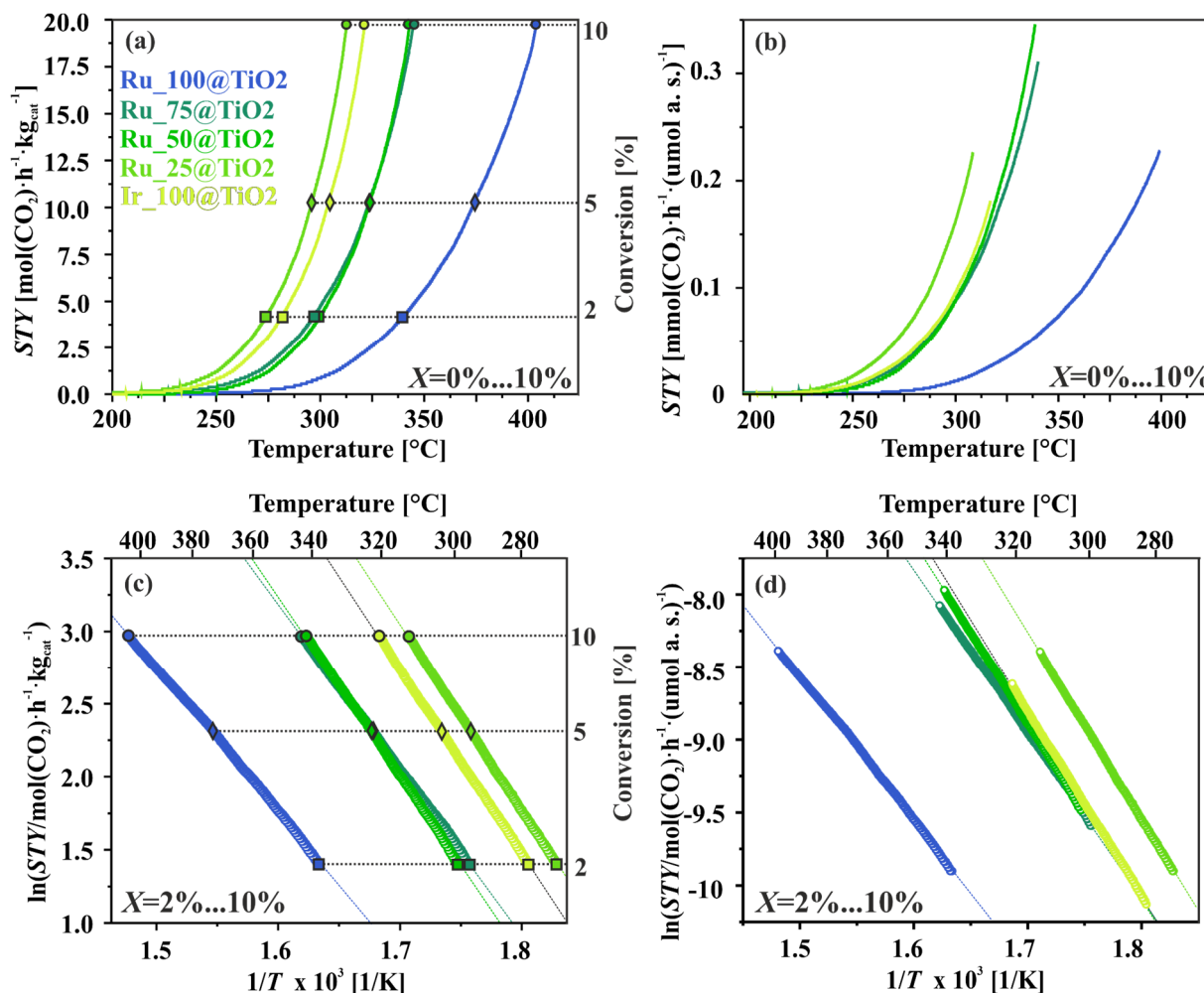
Figure 8.38: Light-off experiments for the catalytic CH_4 combustion reaction over supported mixed $Ru_xIr_{1-x}O_2@TiO_2$ samples normalized to a) the mass of the catalyst and b) to the number of active sites. In all *STY* curves the conversion ranges from 0% to 10%, the total flow rate was 100 sccm with $Vol\%(CH_4):Vol\%(O_2)=2:8$. Corresponding Arrhenius plots are shown for c) *STY* and d) *STY* normalized to the number of active sites.

The activity data shown in **Figure 8.38a,b** can also be represented as Arrhenius plots (**Figure 8.38c,d**) in order to extract kinetic data such as the apparent activation energies E_{act} and the pre-factors STY_0 which are compiled in **Table 8.18**. The apparent activation energies are independent of the normalization procedure, but the STY_0 values depend on the normalization. The highest activity is paralleled by the highest values of the pre-factors, while the apparent activation energies counteract these values by high apparent activation energies for the active catalysts and lower values for the less active catalyst, known as Cremer-Constable

compensation. The pre-factor for Ru_100@TiO_2 is three order of magnitude lower than that of Ru_25@TiO_2, making Ru_100@TiO_2 substantially less active than Ru_25@TiO_2. A similar pattern in the apparent activation energies and pre-factors is encountered for the CO oxidation over the unsupported ruthenium-iridium mixed oxide catalysts (**Table 8.6**).

Table 8.18: Light-off temperatures $T2$ ($X=2\%$), $T5$ ($X=5\%$) and $T10$ ($X=10\%$) for supported mixed Ru_x@TiO_2 materials applied to methane combustion reaction. Kinetic parameters: Apparent activation energies E_{act} and pre-factors STY_0 (normalized to the mass of the catalysts and normalized to the number of active sites) as well as the reaction orders $R.O.$ in oxygen and methane.

sample@TiO_2	Ir_100	Ru_25	Ru_50	Ru_75	Ru_100
$T2$ [°C]	281	274	299	296	339
$T5$ [°C]	304	296	324	323	374
$T10$ [°C]	322	313	344	346	403
E_{act} [kJ·mol^{-1}]	105	107	104	93	82
STY_0 [mol(CO_2)·h^{-1}·kg$_{cat}^{-1}$]	$3 \cdot 10^{10}$	$6 \cdot 10^{10}$	$1 \cdot 10^{10}$	$1 \cdot 10^{9}$	$4 \cdot 10^{7}$
STY_0 [mol(CO_2)·h^{-1}·µmol #($a.s.$)$^{-1}$]	$3 \cdot 10^{5}$	$8 \cdot 10^{5}$	$2 \cdot 10^{5}$	$2 \cdot 10^{4}$	$5 \cdot 10^{2}$
$R.O.$ in O_2	0.0	0.0	0.0	0.0	0.0
$R.O.$ in CH_4	1.0	0.9	0.8	0.9	0.9

To conclude the kinetic study additional experiments were performed to determine the reaction order $R.O.$ (**Figure 8.39**). The reaction temperature is chosen for each sample in a way that the conversion is $X=10\%$ for a reaction mixture of 8 sccm O_2 and 2 sccm methane. After reaching $T10$ the reaction order is determined by changing the volumetric concentration of oxygen from 8 sccm to 2 sccm in steps of 2 sccm while keeping the methane concentration constant at 2 sccm. Subsequently, the oxygen concentration is kept constant at 2 sccm and the methane concentration is decreased in steps of 0.5 sccm from 2 sccm to 1 sccm. The oxygen concentration is then increased in steps of 2 sccm back from 2 sccm to 8 sccm while the methane concentration is fixed at 1 sccm. Finally, the methane concentration is raised from 1 sccm to 1.5 sccm to 2 sccm, thereby returning to the starting gas composition. This protocol enables an investigation of the reaction order of oxygen and methane over a wide range of reaction conditions from oxidizing ($Vol\%$(O_2)=8 %, $Vol\%$(CH_4)=2%), stoichiometric ($Vol\%$(O_2)=4%, $Vol\%$(CH_4)=2%) to reducing ($Vol\%$(O_2)=2%, $Vol\%$(CH_4)=2%) conditions. The reaction orders are summarized in **Table 8.18**. It turns out that the reaction order in O_2 in all cases is zero, while the reaction order in methane is close to unity. From these values it is inferred that the oxygen supply on the catalyst's surface is not rate limiting, while CH_4 activation seems to dominate the reaction kinetics.
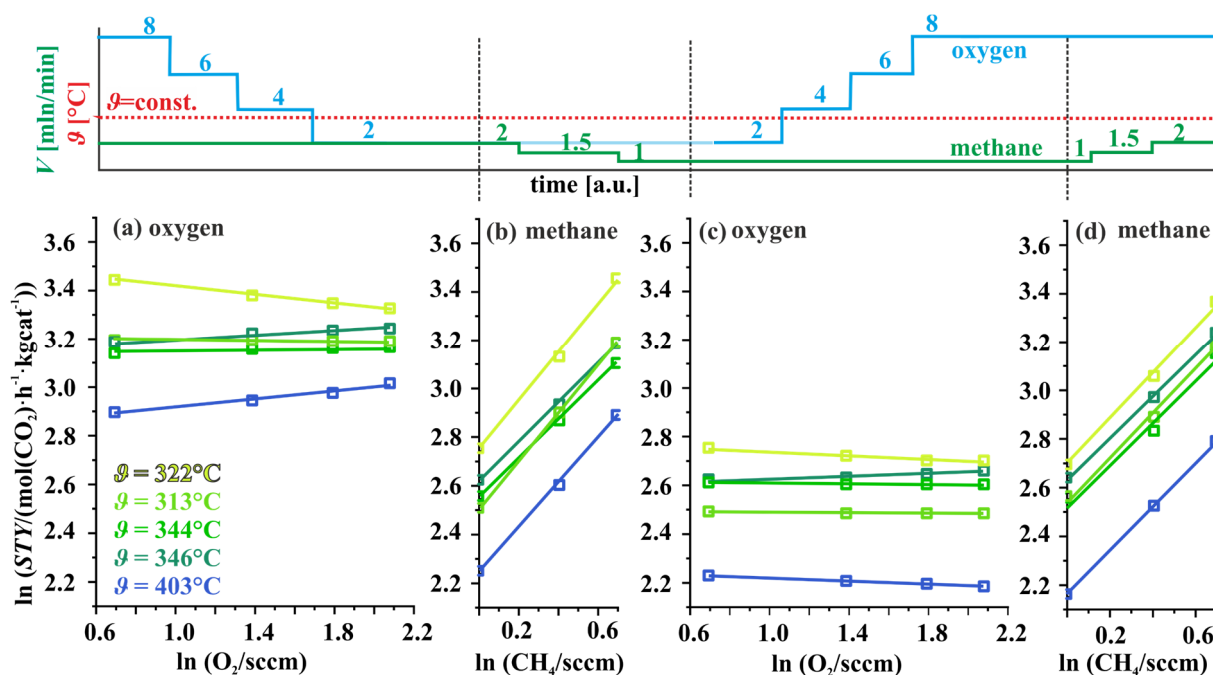
Figure 8.39: Reaction order for oxygen and methane in the methane combustion reaction over supported Ru$_x$Ir$_{1-x}$O2@TiO$_2$ oxide samples with total flow rate of 100 sccm at a reaction temperature where the conversion is 10% (for 2 sccm methane and 8 sccm O$_2$ balanced by 90 sccm N$_2$). The methane concentration is kept constant at a) 2 sccm and c) 1 sccm, while the oxygen concentration varies between 2 sccm to 8 sccm in steps of 2 sccm. To obtain the reaction in methane the oxygen concentration is kept fixed at b) 2 sccm and d) 8 sccm and the methane concentration is varied between 1 sccm to 2 sccm in steps of 0.5 sccm.

For comparison reason similar kinetics experiments for the unsupported ruthenium-iridium mixed oxide catalysts were carried out. The light-off curves as well as the Arrhenius-like plots of methane combustion reaction over the unsupported Ru_x samples are shown in **Figure 8.40**. The data are normalized to the BET surface area (**Figure 8.40b**) assuming that the number of active sites scales with the surface area.[89] A linear temperature ramp of 2 K·min^{-1} is used to increase the conversion X of the methane combustion reaction to a maximum of 10%. The light off temperatures $T2$, $T5$ and $T10$ are summarized in **Table 8.19**, revealing a similar trend as for the supported material (**Figure 8.38**, **Table 8.18**). RuO$_2$ as the active component of the Ru_100 sample shows the highest light off temperatures and therefore the lowest activity in this context. The Ru_25 catalyst reveals the highest activity followed by the Ru_75 sample both surpassing the pure iridium Ir_100 sample. The Ru_50 catalyst shows a slightly lower activity then the Ir_100 sample but still significantly better than the pure Ru_100.
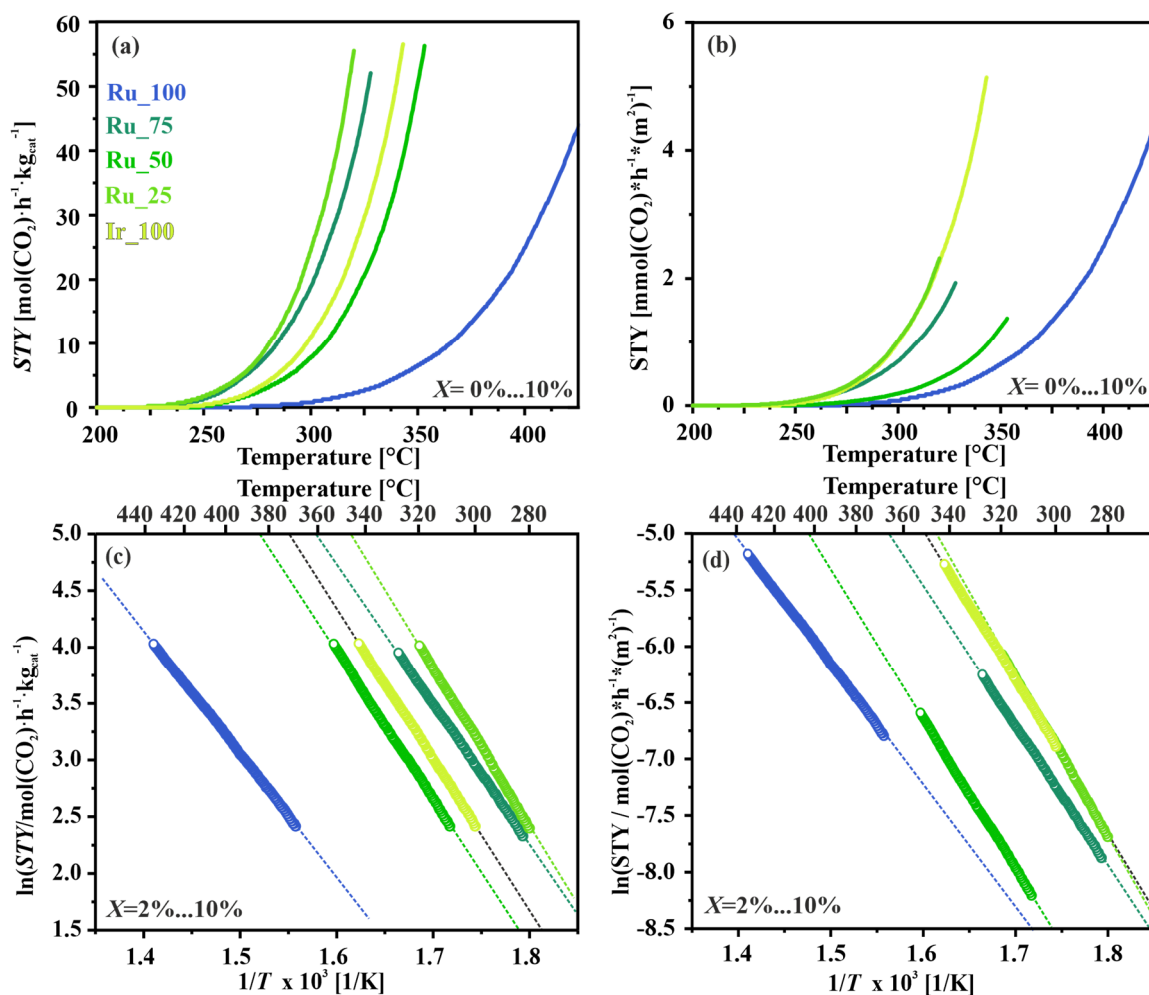
Figure 8.40: Light-off experiments for the catalytic methane combustion reaction over unsupported Ru$_x$Ir$_{1-x}$O$_2$ powder samples normalized to a) mass of the catalyst and b) to the BET surface area. In all *STY* curves the conversion ranges from 0% to 10%, the total flow rate is 100 sccm with *Vol%*(CH$_4$):*Vol%*(O$_2$)=2:8. Corresponding Arrhenius plots are shown for a) *STY* normalized to mass of catalyst and d) *STY* normalized to the *BET* values.

In order to obtain kinetic data in terms of apparent activation energy and the pre-factor *STY$_0$*, the activity data are shown in Arrhenius-like plots (**Figure 8.40c,d**). The normalization has no impact on the activation energies, but it has an impact on the pre-factors given in **Table 8.19**. The activity trend parallels the values of the pre-factors while the apparent activation energies counteract, revealing higher apparent activation energies for the more active catalysts and lower values for the less active catalysts (Cremer-Constable compensation).

In a further experiment shown in **Figure 8.41**, the reaction orders in methane and oxygen are determined at constant temperatures where the conversion is 10%, adapting the *T10* values as given in **Table 8.19**. To reveal the reaction order of oxygen, first the methane concentration was kept constant at 1 sccm while changing the oxygen concentration stepwise from 2 sccm to 8 sccm in steps of 2 sccm. Afterwards, the methane concentration is been varied from 1 sccm to 2 sccm in steps of 0.5 sccm. The results are summarized in **Table 8.19** indicating a reaction

order of zero in oxygen for all catalysts and a reaction order of close to one in methane also for all catalysts. Altogether, the overall catalytic results of the unsupported materials are similar to those of the supported materials.
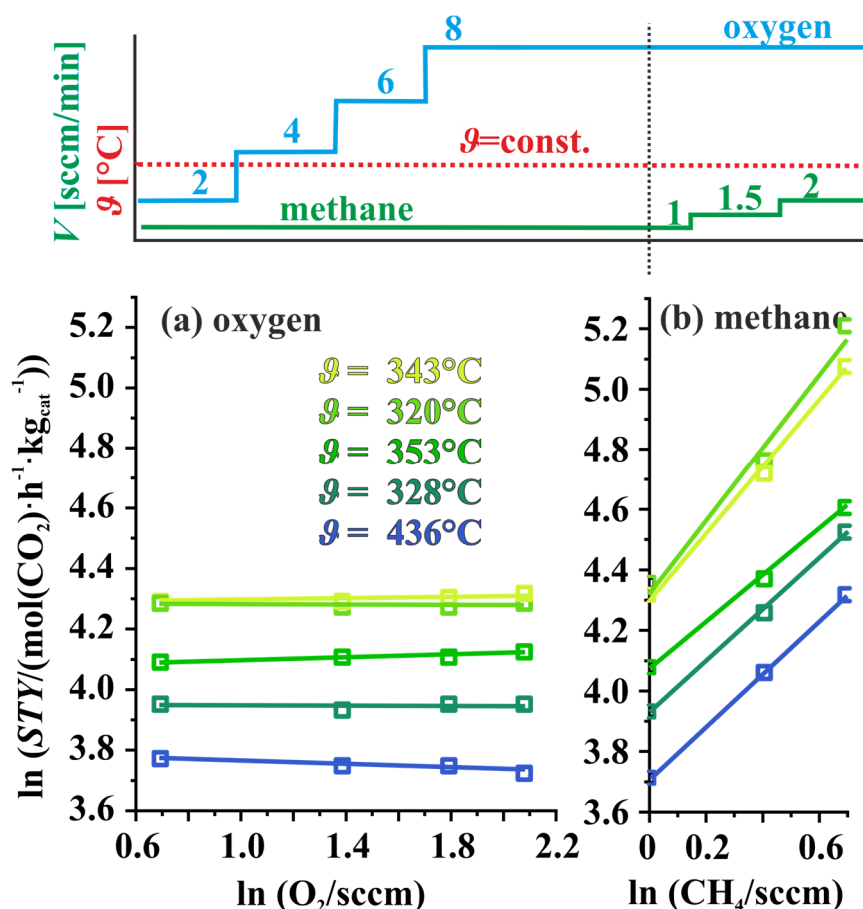
Figure 8.41: Reaction order for oxygen and methane for methane combustion reaction over unsupported mixed Ru$_x$Ir$_{1-x}$O$_2$ oxide catalysts with total flow rate of 100 sccm at a reaction temperature where the conversion is 10% (for 2 sccm methane and 8 sccm O$_2$ balanced by 90 sccm N$_2$). The methane concentration is kept constant at 1 sccm while the oxygen concentration varies between 2 sccm to 8 sccm in steps of 2 sccm. Subsequently the oxygen concentration was kept fixed at 8 sccm and the methane concentration is varied between 1 sccm to 2 sccm in steps of 0.5 sccm.

Table 8.19: Light-off temperatures $T2$, $T5$ and $T10$ for unsupported mixed ruthenium-iridium materials referred to as Ru_x applied to methane combustion reaction. Kinetic parameters: Apparent activation energies E_{act} and pre-factors STY_0 (normalized to the mass of the catalysts and normalized to the BET surface area) as well as the reaction orders $R.O.$ in oxygen and methane.

sample	Ir_100	Ru_25	Ru_50	Ru_75	Ru_100
$T2$ [°C]	300	282	309	285	369
$T5$ [°C]	323	303	334	308	404
$T10$ [°C]	343	320	353	328	436
E_{act} [kJ·mol^{-1}]	110	117	110	103	90
STY_0 [mol(CO$_2$)·h^{-1}·m$_{cat}^{-1}$]	$1 \cdot 10^{11}$	$1 \cdot 10^{12}$	$8 \cdot 10^{10}$	$5 \cdot 10^{10}$	$2 \cdot 10^{8}$
STY_0 [mol(CO$_2$)·h^{-1}·m^{-2}]	$1 \cdot 10^{7}$	$5 \cdot 10^{7}$	$6 \cdot 10^{6}$	$2 \cdot 10^{6}$	$2 \cdot 10^{4}$
$R.O.$ in O$_2$	0.0	0.0	0.0	0.0	0.0
$R.O.$ in CH$_4$	1.1	1.2	0.8	0.9	0.9

In **Figure 8.42** high conversion light off experiments for both the unsupported and supported material are depicted. While for low conversion mainly the intrinsic activity (micro-kinetics) is reflected, the performance of the catalysts at higher conversion is increasingly more governed by heat and mass transfer. From the complete light-off curves *T50*, *T70* and *T90* values (temperature for 50%, 70% and 90% conversion) can be extracted for the various catalyst's compositions. Up to the conversion *T10* the light off curves shown in **Figure 8.42** correspond to the previous kinetic light off experiments of both unsupported (**Figure 8.40**) and supported (**Figure 8.38**) materials. For the unsupported material the light off curves at higher conversions are in line with the expectations as given by extrapolation with the corresponding activation energies from **Table 8.19**. Possible side reactions or product inhibition do not seem to play important roles and transport limitations occur quite late allowing Ru_25, Ru_75 and Ir_100 to reach 90% conversion at temperatures lower than 475 °C. In the case of the supported materials, the trend of the light-off curves changes. **Table 8.20** summarizes the light off temperatures *T50*, *T70* and *T90* for both unsupported and supported materials.
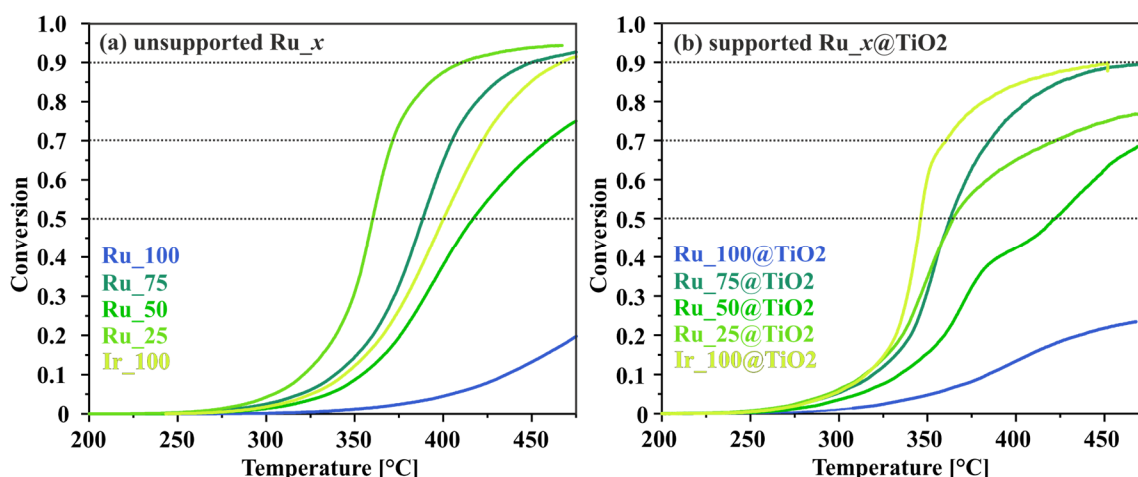
Figure 8.42: Light-off experiments for the catalytic CH_4 combustion reaction over a) unsupported mixed $Ru_xIr_{1-x}O_2$ oxides and b) supported mixed $Ru_xIr_{1-x}O_2@TiO_2$ oxides, showing the conversion *X* as a function of the temperature. The total flow rate is 100 sccm with *Vol%*(CH_4):*Vol%*(O_2)=2:8. The oven temperature cannot exceed 500 °C for experimental limitations.

Table 8.20: Light-off temperatures *T50, T70 and T90* for both unsupported mixed Ru_*x* and supported mixed Ru_*x*@TiO_2 samples applied to the methane combustion reaction derived from Figure 8.42. The reproducibility of the light-off temperatures is ±5 °C.

sample	*T50* [°C]	*T70* [°C]	*T90* [°C]	sample	*T50* [°C]	*T70* [°C]	*T90* [°C]
Ir_100	400	422	465	**Ir_100@TiO₂**	346	359	447
Ru_25	360	371	408	**Ru_25@TiO₂**	364	420	-
Ru_50	416	458	-	**Ru_50@TiO₂**	421	473	-
Ru_75	388	405	447	**Ru_75@TiO₂**	363	385	469
Ru_100	-	-	-	**Ru_100@TiO₂**	-	-	-

The lowest *T90* value is revealed for the unsupported Ru_25 catalyst which underlines its high catalytic activity throughout the whole conversion range, while Ru_75 is the second best performing catalyst. For the supported materials the catalytic performance of Ru_25@TiO₂ becomes inferior compared to the pure Ir_100@TiO₂ but also to the Ru_75@TiO₂ sample above a conversion of 10%. Altogether, $Ru_{0.75}Ir_{0.25}O_2$ reveals a surprisingly good catalytic performance for both supported and unsupported materials.
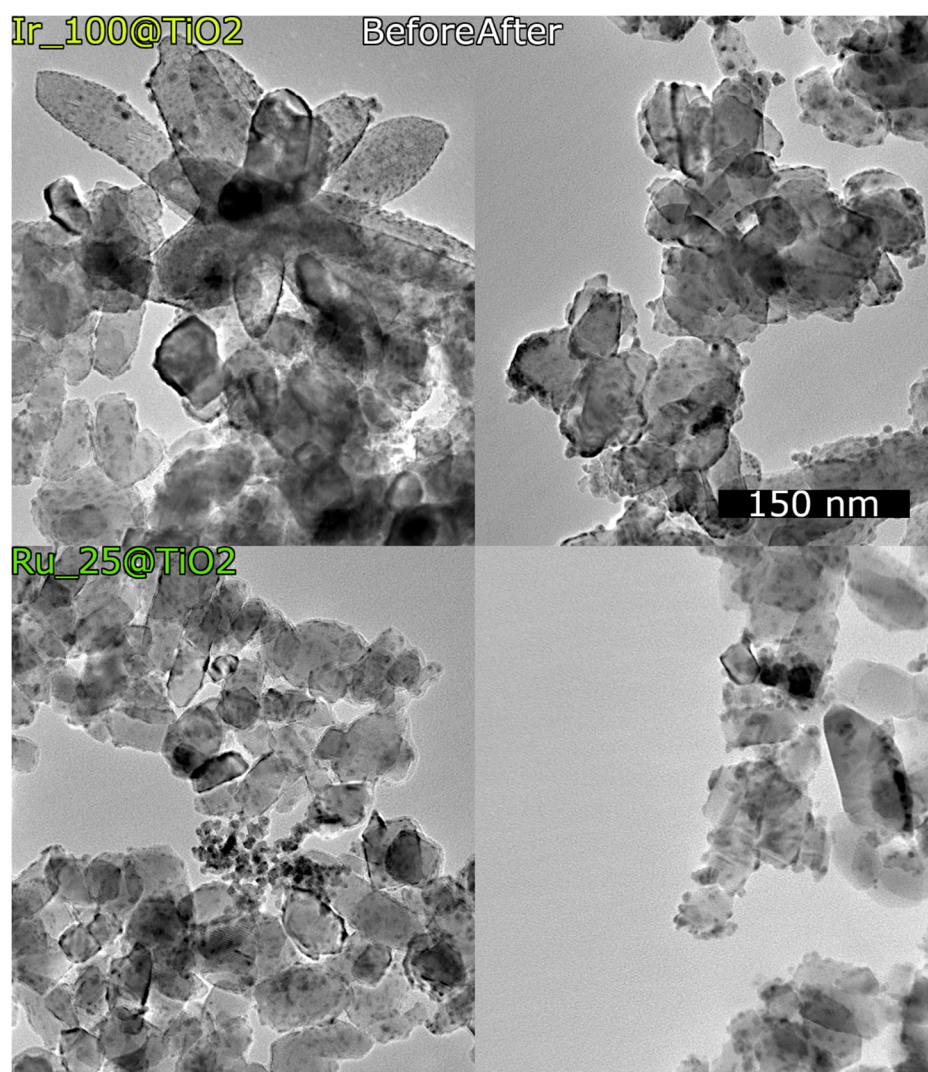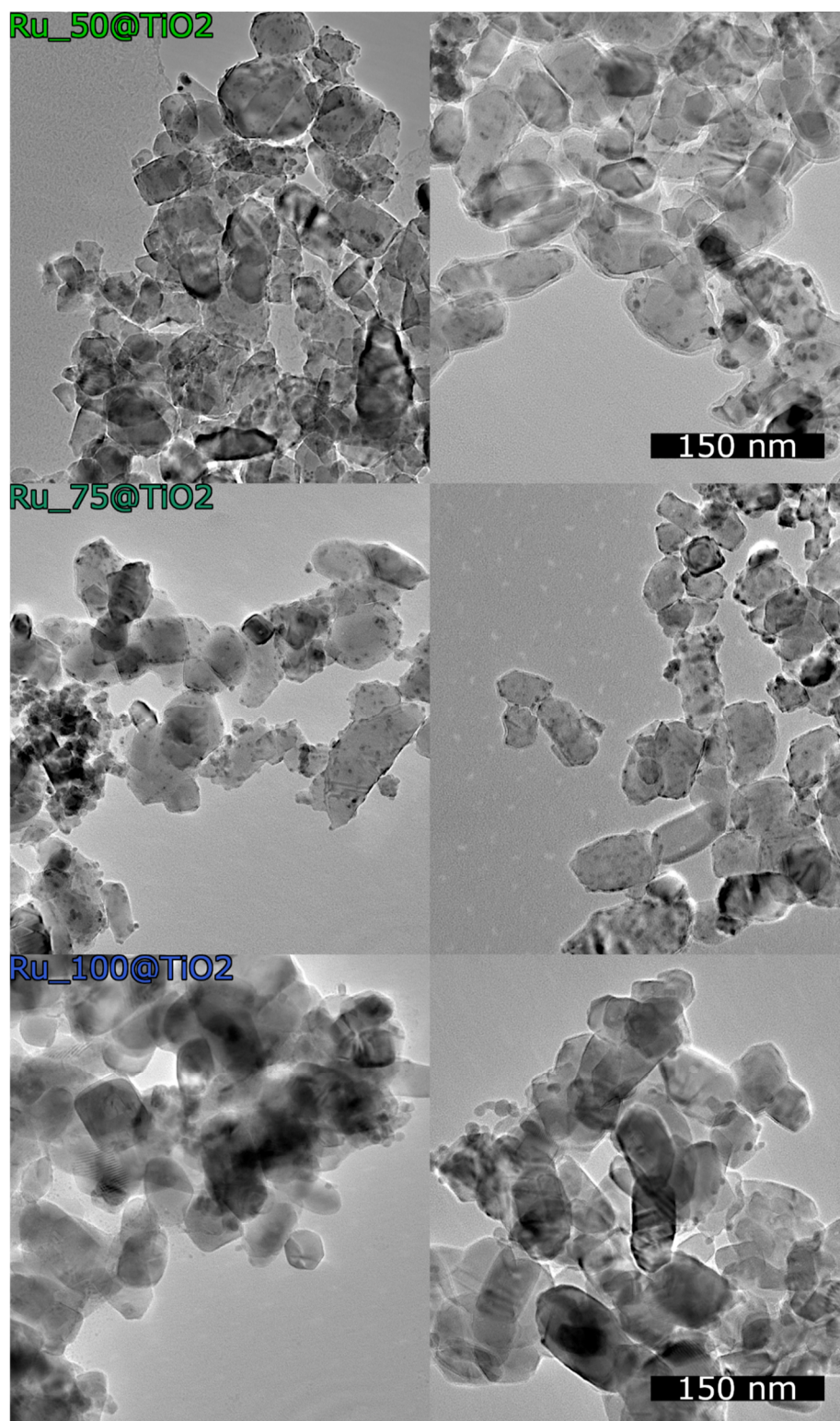
Figure 8.43: TEM images of Ru_x@TiO_2 samples at a magnification of 43,000 and varying composition x before (left) and after (right) catalytic methane combustion. This comparison shows no reaction induced alternations in the catalysts.

After all catalytic and kinetic experiments, the Ru_x@TiO_2 catalysts are post-characterized by TEM (**Figure 8.43**). A comparison with the as-prepared Ru_x@TiO_2 catalysts reveals that no reaction-induced alterations are discernible, i.e., the catalysts are stable under the applied reaction conditions.

8.2.5 Discussion

The supported mixed $Ru_xIr_{1-x}O_2@TiO_2$ are successfully prepared with well-defined composition x. In all cases 5 mol% of active component was employed in order to allow for in-depth characterization of the active component by XRD, XPS, TEM, and CO chemisorption. Most notably, XPS and also STEM element mapping indicate that the composition x of mixed $Ru_xIr_{1-x}O_2$ corresponds to that of the molar ratio of iridium and ruthenium precursors employed in the synthesis, clearly demonstrating the high level of control on the composition x.

Rutile-TiO_2 particles serve as nucleation centers in the Pechini method. While the dispersion of pure IrO_2 particles turns out to be high, deposition of pure RuO_2 on rutile TiO_2 is less clear-cut. According to HRTEM, RuO_2 forms thin layers on rutile-TiO_2 and in addition unsupported larger RuO_2 particles. This observation is consistent with a previous study, where pure RuO_2 is reported to grow epitaxially on rutile-TiO_2 but not on anatase TiO_2 particles.[227] TEM clearly reveals that the remaining Ru_x@TiO_2 samples with ruthenium compositions of 25 mol%, 50 mol%, and 75 mol% form supported particles besides agglomerates of unsupported mixed ruthenium-iridium oxide particles, although the density of supported particles is significantly lower than that of Ir_100@TiO_2.

Obviously, pure IrO_2 and pure RuO_2 adhere differently to the supporting rutile-TiO_2 particles. Surface science studies reveal rutile RuO_2 to form a strained pseudomorphic $RuO_2(110)$ layer adopting the surface lattice constants of the supporting rutile-$TiO_2(110)$,[226] while rutile IrO_2 grows with much less strain on rutile-$TiO_2(110)$.[219,228] Since the surface energy of IrO_2 is substantially higher than that of TiO_2 and the interfacial energy IrO_2/TiO_2 remains high, this may cause IrO_2 to form particles rather than a wetting film on rutile TiO_2 with a small surface and interface area. Due to the quasi-pseudomorphic growth of RuO_2 on rutile-TiO_2, the interfacial energy RuO_2/TiO_2 is low so that RuO_2 is able to partly wet the TiO_2 particles, despite similar the surface energies of RuO_2 and IrO_2.[229] Further growth of RuO_2 proceeds in separate particles with its native lattice constants. Obviously, this is energetically more favorable than increasing the RuO_2 film thickness beyond 1-2 nm.

The number of active sites or the relative active surface area for Ru_x@TiO_2 has been successfully quantified by CO uptake experiments (**Table 8.17**). The number of active sites is found to be high for Ir_100@TiO_2, while with increasing concentration of ruthenium the number of active sites decreases by a factor of 2-3. This decline in active sites can be related to the decreased concentration of supported particles. However, for pure Ru_100@TiO_2 the number of active sites is surprisingly high and not reconciled with large RuO_2 particles

evidenced by XRD (**Table 8.16**). The high active surface area of Ru_100@TiO$_2$ may be attributed to the observed thin layer growth of RuO$_2$ on rutile-TiO$_2$ (**Figure 8.37**).

The activity and the kinetics of catalytic methane combustion over supported Ru_x@TiO$_2$ and unsupported powder Ru_x catalysts with varying compositions x ranging from pure RuO$_2$ to pure IrO$_2$ in steps of 25 mol% was studied. A comparison between supported and unsupported catalysts reveals practically identical trends in the activity for X=0% to X=10% and identical kinetics as a function of the composition x. Therefore, the rutile TiO$_2$ support seems to have virtually no impact on the micro-kinetics of the methane combustion. However, for higher conversions the different dispersions of the active component on the support material seems to differently influence the heat and mass transfer which lead to re-ordering of the light-off curves. Nevertheless, this situation may change when the TiO$_2$ support is replaced for instance by CeO$_2$ or Al$_2$O$_3$, where charge transfer and spill-over phenomena are known to be operative.[230] At least for Pd-based catalysts, the standard catalyst for methane combustion,[25] the support has shown to play an important role.[86,231] For Pd embedded in CeO$_2$ the activity in methane combustion could be increased considerably.[232] Recall that under typical reaction conditions of methane combustion not metallic Pd but rather PdO is the active phase.[233]

In the low conversion catalytic tests (**Figure 8.38**) the most active catalyst turned out to be Ru_25@TiO$_2$ (Ru_25) followed by Ir_100@TiO$_2$ (Ir_100) and then with increasing ruthenium concentration the activity declines steadily with pure Ru_100@TiO$_2$ (Ru_100) being by far the least active catalyst. Pure IrO$_2$ is substantially more efficient than pure RuO$_2$ in methane combustion. This finding is in accordance with surface science experiments which demonstrate methane to be activated even at low temperatures on IrO$_2$(110),[112] while under the very same conditions RuO$_2$(110) is virtually inactive.[67] Obviously, methane activation is an important step in methane combustion and therefore Ru_100@TiO$_2$ is the least active catalyst among the homologous series Ru_x@TiO$_2$. From these surface science studies, it is quite surprising that pure RuO$_2$ is active at all in methane combustion. But the observed activity of RuO$_2$ is consistent with a recent study where RuO$_2$ supported on γ-alumina was discussed as alternative catalyst for methane combustion.[84]

Pure RuO$_2$(110) is, however, known to be an excellent catalyst in the CO oxidation reaction,[129] while on IrO$_2$(110) the adsorption of CO was found to be much stronger than on RuO$_2$.[220] In fact, RuO$_2$ has shown to be more active in the CO oxidation than IrO$_2$ (**Figure 8.16, Table 8.6**). Therefore, a synergism effect of ruthenium on the activity of methane combustion with solid solutions of Ru$_x$Ir$_{1-x}$O$_2$ is expected. Indeed, 25 mol% ruthenium in the mixed oxide catalysts

reveals a significant improvement of the catalytic performance in methane combustion. In order to decide whether this improvement is due to the higher dispersion of $Ru_xIr_{1-x}O_2$ on rutile TiO_2 or to an increase in intrinsic activity, the *STY* values need to be normalized to the number of active surface sites as provided by CO uptake experiments (**Table 8.17**). Since the trend in activity among Ru_*x*@TiO_2 is not affected by this normalization procedure, the improved performance of the Ru_25@TiO_2 sample in methane combustion is ascribed to an increase in the intrinsic activity of the mixed oxide. A very similar trend in activity is found for the unsupported Ru_*x* catalysts, where the *STY* is normalized to the BET surface area.

The superior performance of Ru_25@TiO_2 in methane combustion points towards an intimate interplay of methane activation (by IrO_2) and the subsequent formation of an oxygenated reaction intermediate from the methyl fragment, such as CO, CH_2O, or CHO_2 or the final oxidation step to CO_2 by RuO_2. Of course, RuO_2 may equally promote the oxidation of the abstracted H from methane to form water. This may be evident when one again considers corresponding surface science experiments: Hydrogen adsorption and subsequent annealing of the sample lead to water formation between 400 K to 500 K for $RuO_2(110)$[234] but result in a broad water desorption feature ranging from 400 K to 750 K for $IrO_2(110)$.[235] Quite surprising is the observation that Ru_75@TiO_2 and Ru_75, although being not the most active catalyst, are substantially more active than Ru_100@TiO_2 and Ru_100 (**Figure 8.38d**) by decreasing the reaction temperature *T10* by 80 K. This means that already a small concentration of iridium can improve the low temperature methane activity of RuO_2 considerably.

The observed kinetics (for conversions lower than 10%) of the methane combustion over unsupported Ru_*x* (**Table 8.19**) and supported Ru_*x*@TiO_2 (**Table 8.18**) are virtually identical, corroborating the view that the rutile-TiO_2 support does hardly affect the catalytic behavior of the active component. From the kinetic data of Ru_*x*@TiO_2 in **Table 8.18**, the catalysts can be grouped in two categories, one with a high concentration of ruthenium (50 mol%, 75 mol%) and the other with low ruthenium concentration of ruthenium (0 mol%, 25 mol%, 50 mol%). The apparent activation energies and the pre-factors of the ruthenium-rich catalysts (80-90 $kJ \cdot mol^{-1}$) are significantly lower than those of the iridium-rich catalysts (105±2 $kJ \cdot mol^{-1}$). The most active catalyst Ru_25@TiO_2 reveals the highest apparent activation energy and the highest pre-factor, resulting in a catalyst that at higher reaction temperature is even more active than the others. Obviously, the higher apparent activation energy is overcompensated by the high value of the pre-factor. This compensation effect, as mentioned repeatedly, is known as the

Cremer-Constable relation. Similar apparent activation energies as for the present iridium-rich catalysts are also reported for supported Pd and Pt based catalysts.[25]

For methane combustion over both Ru_x@TiO$_2$ and Ru_x, the reaction order in methane is close to one, while that in oxygen is zero. Obviously, oxygen is omnipresent on the catalyst's surface and oxygen vacancies can readily be replenished by O_2 exposure. Quite in contrast, methane activation seems to be rate limiting which is reflected by a reaction order of one in methane. These reaction orders for the total methane oxidation reaction over Ru_x@TiO$_2$ and Ru_x agree remarkably well with those reported for other noble metal catalysts.[236]

For the unsupported material, Ru_25 and Ru_75 remain the most active catalysts in the entire temperature and conversion range. Due most likely to transport limitations which vary among the supported materials with their varying dispersions and particle sizes, the catalytic activity of Ru_25@TiO$_2$ decreases with increasing conversion whereby Ir100@TiO$_2$ and Ru_75@TiO$_2$ become the most promising catalysts. At very high conversions the catalytic performance of Ru_75 and Ru_75@TiO$_2$ approaches even that of the pure Ir100 and Ir100@TiO$_2$ catalysts.

In **Table 8.21** the catalytic performance (*T50* and *T90*) of Ir_100@TiO$_2$ and Ru_75@TiO$_2$ as the most promising candidates in the catalytic methane combustion is compared to supported Pd catalysts, defining the benchmark catalysts for low temperature methane combustion. Unfortunately, a direct comparison of *T*50 and *T*90 values is hampered by differences in the mass of catalyst, the loading of the active component, the gas composition fed to the reactor, and the contact time with the catalyst material; all these factors affect the light-off curves.

Table 8.21: Comparison of *T50* and *T90* values of Ir_100@TiO$_2$ and Ru_75@TiO$_2$ with those of Pd@Al$_2$O$_3$ and Pd@TiO$_2$ under similar reaction conditions.

sample	mass of catalyst	loading	flow rate	%CH$_4$	*T50* [°C]	*T90* [°C]
Ir_100@TiO$_2$	20 mg	5 mol% (10 wt%)	100 sccm	2	346	447
Ru_75@TiO$_2$	20 mg	5 mol% (7 wt%)	100 sccm	2	363	469
Pd@TiO$_2$[237]	100 mg	5 wt%	100 sccm	0.8	331	403
Pd@Al$_2$O$_3$[238]	120 mg	5 wt%	100 sccm	1	≈350	≈400
Pd@Al$_2$O$_3$[239]	100 mg	0.5 wt%	100 sccm	1	≈395	≈460
Pd@Al$_2$O$_3$[240]	200 mg	2 wt%	100 sccm	0.2	≈600	≈660
Pd@Al$_2$O$_3$[241]	≈20 mg	5 wt%	200 sccm	0.25	340	560
Pd@Al$_2$O$_3$[242]	320 mg	2 wt%	100 sccm	1	460	-

From the *T50* and *T90* values summarized in **Table 8.21** it can be seen that the activity of both Ir_100@TiO$_2$ and Ru_75@TiO$_2$ is comparable to that of Pd@Al$_2$O$_3$. A direct comparison of the Ir_100@TiO$_2$ and Ru_75@TiO$_2$ with Pd@TiO$_2$ reveals that *T90* is 44 to 66 K lower. However, in this work the methane fed is two times higher and the amount of the active component is about 2 to 3 times lower than in the referenced study of Pd@TiO$_2$.

8.3 Catalytic Key Findings & Developed Reaction Scheme
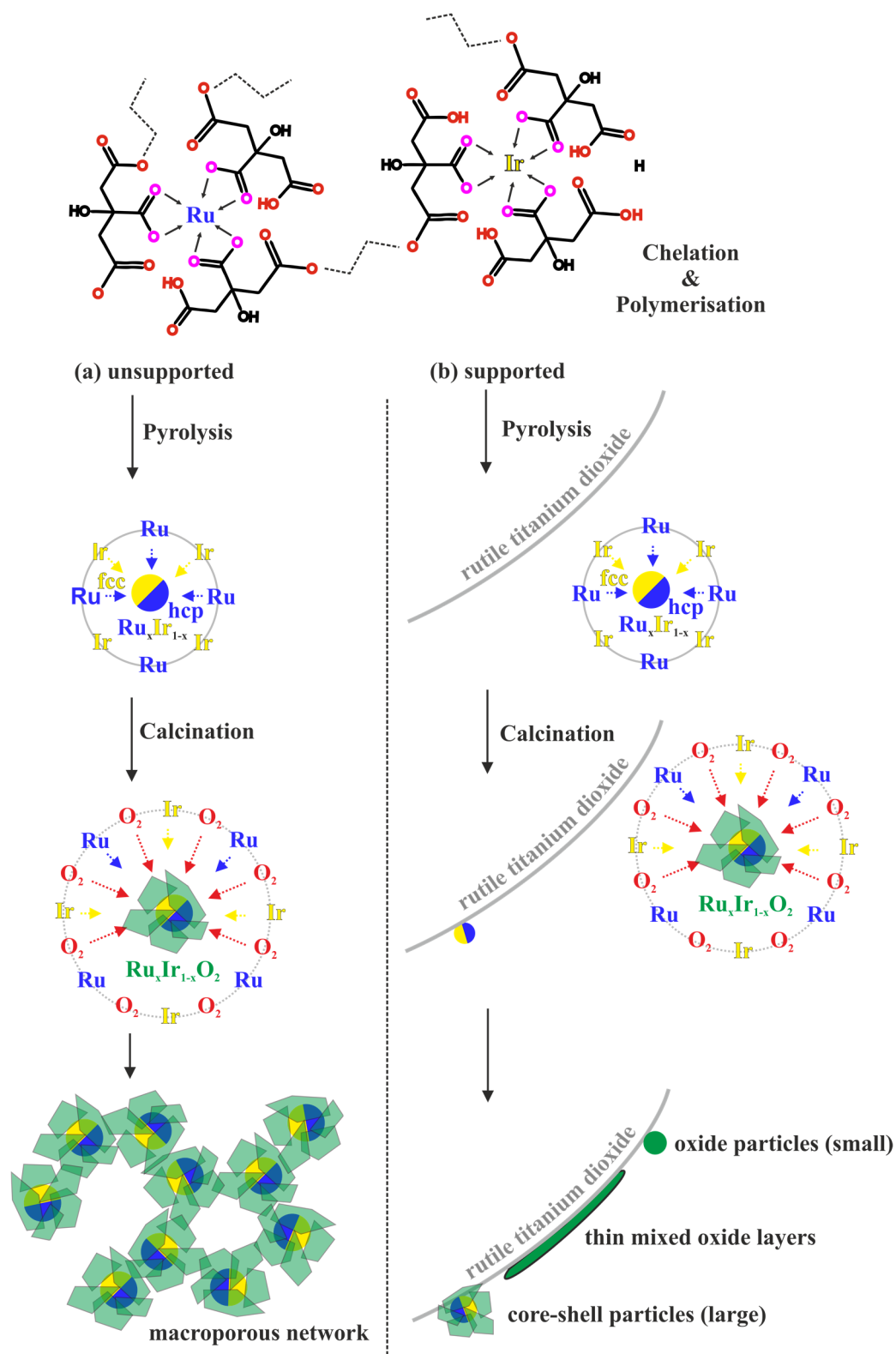
Figure 8.44: Schematic overview of the employed Pechini sol-gel method for a) unsupported ruthenium-iridium mixed materials and b) supported ruthenium-iridium mixed materials. An initial chelation of the metal cations by citric acid forms coordination complexes, which are cross-linked by ethylene glycol via esterification. A pyrolysis/calcination leads to the formation of binary metal alloys overgrown by the desired mixed oxide solid solution. In case of the supported materials, preformed rutile TiO_2 nanoparticles are dispersed in the solvent in a prior step and serve as nucleation sites.

First of all, it must be noted that the metallic component in the core does not contribute to the catalytic performance of the surface as can been understood from the developed reaction scheme shown in **Figure 8.44**. The catalytic activity of the unsupported $Ru_xIr_{1-x}O_2$ in the CO oxidation reaction under both stoichiometric and oxidizing conditions is investigated in terms of $T5$ (conversion $X=5\%$) values as well as apparent activations energies E_a and pre-factors STY_0, as derived by Arrhenius-like plots are summarized in **Table 8.22**.

Table 8.22: Kinetic data for catalytic CO oxidation over unsupported ruthenium-iridium mixed oxides under both stoichiometric and oxidizing conditions including the apparent activation energies E_a, the pre-exponential factors STY_0 and the $T5$ values. The light-off curves are measured with a heating ramp of 1 K·min^{-1}, 150 sccm total flow rate and 10-15 mg catalyst material. The STY are normalized to the BET surface area.

x [mol%]	0	12.5	25	37.5	50	62.5	75	87.5	100
stoichiometric conditions (3 sccm CO & 1.5 sccm O_2)									
E_a [kJ·mol^{-1}]	135	109	110	118	127	135	120	130	71
STY_0 [mol(CO_2)·h^{-1}·m^{-2}]	$3\cdot10^8$	$2\cdot10^6$	$4\cdot10^7$	$1\cdot10^9$	$1\cdot10^{11}$	$5\cdot10^{12}$	$2\cdot10^{10}$	$3\cdot10^{12}$	$1\cdot10^4$
$T5$ [°C]	234	196	158	142	115	104	117	**97**	119
oxidizing conditions (1.5 sccm CO & 3 sccm O_2)									
E_a [kJ·mol^{-1}]	97	107	107	114	114	113	116	117	90
STY_0 [mol(CO_2)·h^{-1}·m^{-2}]	$1\cdot10^6$	$1\cdot10^7$	$4\cdot10^7$	$2\cdot10^8$	$2\cdot10^9$	$3\cdot10^9$	$3\cdot10^9$	$3\cdot10^{10}$	$5\cdot10^6$
$T5$ [°C]	194	150	137	136	109	105	115	**99**	103

In general, the intrinsic activity increases with increasing amount of ruthenium in the $Ru_xIr_{1-x}O_2$ system, which is shown by the $T5$ values that increase with higher iridium content. The most active compound, however, is not Ru_100 (RuO_2) but Ru_87.5 ($Ru_{0.875}Ir_{0.125}O_2$) with a $T5$ value of 97 °C under stoichiometric conditions and 99 °C under oxidizing conditions, indicating the beneficial synergistic interaction of ruthenium and iridium. Pure IrO_2 is as expected the least active compound for the CO oxidation reaction under both stoichiometric and oxidizing with $T5$ values of 234 °C and 194 °C, respectively.

While the catalytic CO oxidation is only performed on the unsupported $Ru_xIr_{1-x}O_2$ for pure structure-activity investigation, the methane combustion reaction is performed also on more realistic supported materials, where the carrier provides a high dispersion of the active component with an increased thermal stability. To be able to exclude metal-support interactions, both the supported and unsupported materials are comparatively studied during methane combustion to ensure that the carrier does not influence the trend of intrinsic activities. The results are summarized in **Table 8.23**.

Table 8.23: Kinetic data for catalytic CH_4 combustion over unsupported and supported ruthenium-iridium mixed oxides including the apparent activation energies E_a, the pre-exponential factors STY_0, the reaction orders a/b and the $T5$ values. The light-off curves are measured with a heating ramp of 2 K·min^{-1} for unsupported and 1 K·min^{-1} for the supported materials. The total flow rate is 100 sccm and 10-15 mg catalyst for unsupported and 20-30 mg catalyst for supported materials are used. The STY are normalized to the BET surface area for the unsupported and to number of active sites for the supported materials.

x [mol%]	0	25	50	75	100
unsupported					
E_a [kJ·mol^{-1}]	110	117	110	103	90
STY_0 [mol(CO_2)·h^{-1}·m^{-2}]	$1 \cdot 10^7$	$5 \cdot 10^7$	$6 \cdot 10^6$	$2 \cdot 10^6$	$2 \cdot 10^4$
reaction orders CH_4/O_2	0.0 / 1.1	0.0 / 1.2	0.0 / 0.8	0.0 / 0.9	0.0 / 0.9
$T5$ [°C]	323	303	334	308	404
supported					
E_a [kJ·mol^{-1}]	105	107	104	93	82
STY_0 [mol(CO_2)·h^{-1}·(µmol #$a.s.$)$^{-1}$]	$3 \cdot 10^5$	$8 \cdot 10^5$	$2 \cdot 10^5$	$2 \cdot 10^4$	$5 \cdot 10^2$
reaction orders CH_4/O_2	0.0 / 1.0	0.0 / 0.9	0.0 / 0.8	0.0 / 0.9	0.0 / 0.9
$T5$ [°C]	304	296	324	323	374

The unsupported and supported materials both show the same trends of $T5$ values, activation energies and pre-factors as seen in **Table 8.23**. This confirms that the measured STY values actually represent the micro-kinetics since very different kind of samples reveal the same catalytic trend. Therefore, the support material as desired does not influence the activity trends of the active component, however, the apparent activation energies observed for the unsupported materials are generally (5 to 10 kJ·mol^{-1}) higher, which is due to the different heating ramps, 2K·min^{-1} for the unsupported and 1K·min^{-1} for the supported materials.

The structure-activity trends are exactly opposite between the CO oxidation reaction and the methane combustion reaction. While IrO_2 is the least active compound for CO oxidation, both unsupported and supported IrO_2 show outstanding activity for the methane combustion only surpassed by $Ru_{0.25}Ir_{0.75}O_2$ and $Ru_{0.25}Ir_{0.75}O_2@TiO_2$. Also opposed, the least active catalyst for methane combustion showed high activity in the CO oxidation reaction (**Table 8.22**). The best catalysts, $Ru_{0.25}Ir_{0.75}O_2$ ($T5$=303 °C) and $Ru_{0.25}Ir_{0.75}O_2@TiO_2$ ($T5$=296 °C) show the highest activation energies E_a (117 and 107 kJ·mol^{-1}, respectively) compensated by the highest pre-factors STY_0 ($5 \cdot 10^7$ mol(CO_2)·h^{-1}·m^{-2} and $8 \cdot 10^5$ mol(CO_2)·h^{-1}·µmol(#$a.s.$)$^{-1}$, respectively). Along the lines of CO oxidation, where the little admixture of iridium results in the best catalyst material ($Ru_{0.875}Ir_{0.125}O_2$), the intermixing of 25% ruthenium to IrO_2 leads to the best catalyst material for the methane combustion reaction. Both catalytic reactions reveal the synergistic interplay of ruthenium and iridium. The reaction orders is zero in oxygen and close to one in methane for both the unsupported and supported catalysts (**Table 8.23**). The C-H activation seemingly is rate-limiting while the supply of monoatomic oxygen at the active site is less hampered, which is why the iridium samples are understandably much more active than pure

RuO_2, just as predicted from surface science experiments that report single-crystalline $IrO_2(110)$ as a low-temperature promoter for the methane activation.[112,113,200]

In **Table 8.24,** the catalytic performance of the ruthenium-iridium mixed oxides in terms of *T50*, *T70*, and *T90* is compared to those of the benchmark catalyst $Pd@Al_2O_3$. Additionally, $Pd@TiO_2$ is included in the list for a more direct comparison of the active components ($Ru_xIr_{1-x}O_2$ vs. Pd) due to the same carrier material (TiO_2). Considering that the mass of the palladium catalysts is considerably 5 to 6 times higher and that the volumetric concentration of methane is chosen lower as well, the slightly higher *T50* and *T90* of $IrO_2@TiO_2$ and $Ru_{0.75}Ir_{0.25}O_2@TiO_2$ should not be interpreted as worse.

Table 8.24: *T*50, *T*70 and *T*90 values of the supported ruthenium-iridium mixed oxides compared to Pd catalysts from comparable experiments. Note the higher amount of catalyst in the Pd-based experiments from literature as well as the lower volumetric methane concentration.

sample	m_{cat}	nominal loading	$\dot{V}$	*Vol%* (CH_4)	*T50*	*T70*	*T90*
$IrO_2@TiO_2$	20	5 mol% (≈11 wt%)	100 sccm	2	346	359	447
$Ru_{0.75}Ir_{0.25}O_2@TiO_2$	20	5 mol% (≈7 wt%)	100 sccm	2	363	385	469
$Pd@TiO_2$[238]	100	5 wt%	100 sccm	0.8	331	?	403
$Pd@Al_2O_3$[239]	120	5 wt%	100 sccm	1	≈350	?	≈400

9. Conclusion & Outlook

Ruthenium-iridium mixed oxides, both unsupported and supported and referred to as $Ru_xIr_{1-x}O_2$ and $Ru_xIr_{1-x}O_2@TiO_2$, respectively, are successfully prepared by the Pechini sol-gel method with high structural and compositional control. The materials are thoroughly characterized via XRD, RAMAN, XPS, TEM and STEM, SEM, physisorption- and CO chemisorption experiments before application to catalytic CO oxidation and CH_4 combustion.

Extensive characterization of the unsupported materials reveal unprecedented details on the reaction mechanism during preparation. The calcination initially starts with a pyrolysis step followed by oxidation after a significant amount of the carbon backbone is decomposed during synthesis leading to core-shell agglomerates (secondary particles) where the metal core is encapsulated by the mixed oxide. Depending on the nominal composition x, the metal core either forms an alloy or is separated into an Ir-enriched fcc and an Ru-enriched hcp phase due to a miscibility gap in the composition range of $x=0.21$ to $x=0.74$. Thus, the samples with a nominal composition x of 25 mol%, 37.5 mol%, 50 mol% and 62.5 mol% form a ruthenium-rich hcp ($Ru_{0.74}Ir_{0.26}$) and an iridium-rich fcc phase ($Ru_{0.21}Ir_{0.79}$). However, the mixed oxide system does not face any miscibility gap and for each composition x a solid solution $Ru_xIr_{1-x}O_2$ is formed. Based on quantitative characterization, in particular X-ray photoelectron spectroscopy (XPS) and X-ray diffraction (XRD) data, the mean compositions of oxide and alloy are concluded to be identical and agree fairly well with the weighed out amounts of iridium and ruthenium precursors.

The unsupported ruthenium-iridium mixed oxide samples are subject to the prototypical CO oxidation reaction. Since the metal phase is buried, catalytic tests do only probe the activity of the mixed $Ru_xIr_{1-x}O_2$ oxide shell. Pure RuO_2 only at low reaction temperature is the most active catalyst revealing the lowest apparent activation energies. At moderate reaction temperatures above 100 °C the best performing mixed oxide in the CO oxidation reaction is $Ru_{0.875}Ir_{0.125}O_2$ owing to the higher apparent activation energy. As expected, the least active oxidation catalyst is pure IrO_2.

Both unsupported and supported ruthenium-iridium mixed oxide samples are subject to the more complex methane combustion reaction. Pure Ir_100 and Ir_100@TiO_2 are much more active in the combustion of methane than pure Ru_100 and Ru_100@TiO_2, with the former exhibiting an onset temperature of about 220 °C that is similar to onset temperatures encountered for Pd and Pt based catalysts.[25,236] The most active catalyst among the series of Ru_x and Ru_x@TiO_2 turned out to be Ru_25 and Ru_25@TiO_2. Obviously, methane

activation by IrO_2, although mandatory, is only part of the story. The oxidation of methyl to CO_2 is apparently another important step, which is promoted by the addition of RuO_2. Ru_75 and Ru_75@TiO_2, although being not the most active catalysts, are substantially more active than Ru_100 and Ru_100@TiO_2 by decreasing the *T10* temperature by 80 K. Therefore, already a small concentration of iridium improves the activity of RuO_2 in methane combustion considerably. The catalytic performances of Ir_100@TiO_2 and Ru_75@TiO_2 in methane combustion (in terms of *T50* and *T90*) are comparable to that reported for Pd catalysts. However, poisoning of the ruthenium-iridium mixed oxide catalysts by the constituents of the exhaust gas (CO_2, water, SO_2,…)[243] has not been considered and needs further scrutiny.

It is not expected that IrO_2 catalysts will replace Pd-based catalysts for the methane combustion due to the limited amount of mined Ir (6t/a). On the other hand, ruthenium based catalysts face problems of being volatile at temperatures above 500-600 °C due to overoxidation to RuO_3 and RuO_4.[107] However, mixture of 25 mol% or less of IrO_2 and RuO_2 may be an option since Ir thermally stabilize RuO_2, and Ru is significantly more abundant than Ir (30t/a) and about 8 times less expensive than Pd.

From the direct comparison of supported and unsupported catalysts during methane combustion, it can be concluded that the rutile-TiO_2 support does not affect the catalytic performance in methane combustion. However, this may change when switching to another support material such as CeO_2 or Al_2O_3 which have shown to improve the catalytic activity in methane combustion substantially over Pd-based catalysts.[25]

The trends of the intrinsic activities of the presented materials during catalytic CO oxidation and catalytic methane combustion are opposed. While the CO oxidation revealed ruthenium rich mixed oxides to be better catalysts, the methane combustion reaction is more efficient with higher amounts of iridium, results, which confirm the predicted roles of ruthenium as a good oxidation catalyst and iridium as a low-temperature promoter for the C-H activation. However, not pure RuO_2 and pure IrO_2 were the best catalysts for CO oxidation and methane combustion, respectively, but the little admixture of each other gave the best materials demonstrating the synergistic interplay of the noble metals. The motivation of combining the high activity of RuO_2 as an oxidation catalyst with the ability of low-temperature C-H-activation of IrO_2 was successfully implemented during methane combustion in both a synergistic point of view and efficiency point of view regarding the lower iridium content in the catalyst with the best performance under more realistic, high conversion conditions ($Ru_{0.75}Ir_{0.25}O_2$@TiO_2).

Future studies may involve further decrease of the iridium content below 25 mol% to gain even more efficient catalysts. In this work, the loading of the active component was chosen as 5 mol%, as a good compromise of having enough material for a decent bulk and surface characterization and still ensuring most of the active component to be dispersed on the support. However, for pure catalytic purposes the loading can be reduced to enhance the dispersion of the active component and thus maximize the noble metal utilization. Furthermore, the idea of a single-atom catalyst can be realized by preparing iridium-titanium-mixed oxides ($Ir_xTi_{1-x}O_2$) and ruthenium-titanium mixed oxides ($Ru_xTi_{1-x}O_2$) by modified Pechini methods with a large excess of the titanium precursor. Furthermore, the active components can be supported on a carrier to prepare $Ru_xTi_{1-x}O_2@TiO_2$ and $Ir_xTi_{1-x}O_2@TiO_2$ for highly dispersed catalyst materials. For a brief insight, **Figure 9.1** shows first auspicious XRD measurements of unsupported $Ru_xTi_{1-x}O_2$ (**Figure 9.1a**) and $Ir_xTi_{1-x}O_2$ (**Figure 9.1b**) with x=0.0625.
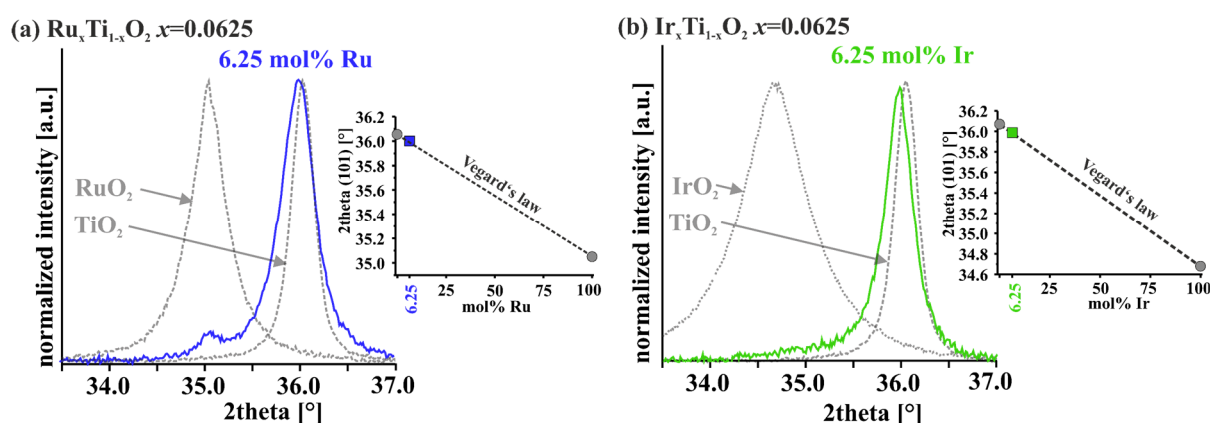

Figure 9.1: Section of XRD patterns of a) ruthenium-titanium mixed oxides and b) iridium-titanium mixed oxides. The rutile (101) reflexes of both $Ru_{0.0625}Ti_{0.9375}O_2$ and $Ir_{0.0625}Ti_{0.9375}O_2$ are shifted according to Vegard's law indicating the successful formation of solid solutions.

10. References

1. T.B. Larsen and J. Harrington Jr, *Geographical Review*, 2020, **11**, 95-117.
2. R. M. Carter, *AusIMM New Leaders' Conference*, Australia, 2.-3. May 2007.
3. E. X Berry, *International Journal of Atmospheric and Oceanic Sciences*, 2019, **3**, 13-26.
4. K. E. Trenberth, *Journal of Energy and Natural Resources Law*, 2018, **36**, 463–481.
5. D. Baus, "Overpopulation and the Impact on the Environment", The City University of New York, 2017.
6. S. E. Schwartz, *Journal of Geophysical Research: Atmospheres*, 2018, **123**, 3462–3482.
7. G. Mavromatidis, K. Orehounig, P. Richner and J. Carmeliet, *Energy Policy*, 2016, **88**, 343–354.
8. S. Bilgen, *Renewable and Sustainable Energy Reviews*, 2014, **38**, 890–902.
9. G. Kalghatgi, *Applied Energy*, 2018, **225**, 965–974.
10. W. H. Haider, *International Petroleum Technology Conference 2020,* Saudi-Arabia, 13.-15. January 2020.
11. M. J. Pickl, *Energy Strategy Reviews*, 2019, **26**, 100370.
12. G. Santos, *Transport Policy*, 2017, **59**, 71–74.
13. P. Nejat, F. Jomehzadeh, M. M. Taheri, M. Gohari and M. Z. Muhd, *Renewable and Sustainable Energy Reviews*, 2015, **43**, 843–862.
14. G. A. Marrero, *Energy Economics*, 2010, **32**, 1356–1363.
15. R. D. Reitz, H. Ogawa, R. Payri, T. Fansler, S. Kokjohn, Y. Moriyoshi, A. K. Agarwal, D. Arcoumanis, D. Assanis, C. Bae, K. Boulouchos, M. Canakci, S. Curran, I. Denbratt, M. Gavaises, M. Guenthner, C. Hasse, Z. Huang, T. Ishiyama, B. Johansson, T. v. Johnson, G. Kalghatgi, M. Koike, S. C. Kong, A. Leipertz, P. Miles, R. Novella, A. Onorati, M. Richter, S. Shuai, D. Siebers, W. Su, M. Trujillo, N. Uchida, B. M. Vaglieco, R. M. Wagner and H. Zhao, *International Journal of Engine Research*, 2020, **21**, 3–10.
16. H. Hao, Z. Liu, F. Zhao and W. Li, *Renewable and Sustainable Energy Reviews*, 2016, **62**, 521–533.
17. J. Dargay, D. Gately and M. Sommer, *Energy Journal*, 2007, **28**, 143–170.
18. C. Bae and J. Kim, *Proceedings of the Combustion Institute*, 2017, **36**, 3389–3413.
19. T. R. Anderson, E. Hawkins and P. D. Jones, *Endeavour*, 2016, **40**, 178–187.
20. N. Norouzi, M. Fani and Z. K. Ziarani, *Journal of Petroleum Science and Engineering*, 2020, **188**, 106827.
21. D. Gielen, F. Boshell, D. Saygin, M. D. Bazilian, N. Wagner and R. Gorini, *Energy Strategy Reviews*, 2019, **24**, 38–50.
22. K. Gillingham and P. Huang, *Energy Journal*, 2019, **40**, 1–26.
23. D. W. Cash, *Energy Research and Social Science*, 2018, **35**, 224–226.
24. S. A. Dyatlov, N. I. Didenko, E. A. Ivanova, E. B. Soshneva and S. v. Kulik, *IOP Conference Series: Earth and Environmental Science*, 2020, **434**, 012014.
25. L. He, Y. Fan, J. Bellettre, J. Yue and L. Luo, *Renewable and Sustainable Energy Reviews*, 2020, **119**, 109589.
26. S. Klebnikov, *Environmental Politics*, 2016, **1**, 8.
27. L. Krishna and C. A. Koh, *MRS Energy & Sustainability*, 2015, **2**, 1–17.
28. IEA (2019), "World Energy Outlook 2019", IEA, Paris. https://www.iea.org/reports/world-energy-outlook-2019 (31.05.2021).
29. R. B. Jackson, E. I. Solomon, J. G. Canadell, M. Cargnello and C. B. Field, *Nature Sustainability*, 2019, **2**, 436–438.

30. S. Perathoner and G. Centi, *Science and Technology Roadmap on Catalysis for Europe*, 2016.

31. J. Chen, H. Arandiyan, X. Gao and J. Li, *Catalysis Surveys from Asia*, 2015, **19**, 140–171.

32. A. Raj, *Johnson Matthey Technology Review*, 2016, **60**, 228–235.

33. L. D. D. Harvey and Zhen Huang, *Journal of Geophysical Research*, 1995, **100**, 2905–2926.

34. A. Glikson, *Energy Procedia*, 2018, **146**, 23–29.

35. T. V. Choudhary, S. Banerjee and V. R. Choudhary, *Applied Catalysis A: General*, 2002, **234**, 1–23.

36. M. F. M. Zwinkels, S. G. JÄRÅS, P. G. Menon and T. A. Griffin, *Catalysis Reviews*, 1993, **35**, 319–358.

37. R. Prasad, L. A. Kennedy and E. Ruckenstein, *Catalysis Reviews Science and Engineering*, 1984, **26**, 1-58.

38. P. Forzatti and G. Groppi, *Catalysis Today*, 1999, **54**, 165–180.

39. V. N. Parmon, A. D. Simonov, V. A. Sadykov and S. F. Tikhov, *Combustion, Explosion and Shock Waves*, 2015, **51**, 143–150.

40. R. Burch, *Catalysis Today*, 1997, **35**, 27–36.

41. N. Gascoin, Q. Yang and K. Chetehouna, *Applied Thermal Engineering*, 2017, **110**, 144–149.

42. S. Kondo, A. Takahashi and K. Tokuhashi, *Journal of Hazardous Materials*, 2002, **94**, 37–45.

43. S. Kondo, K. Takizawa, A. Takahashi and K. Tokuhashi, *Journal of Hazardous Materials*, 2011, **187**, 585–590.

44. C. Robinson and D. B. Smith, *Journal of Hazardous Materials*, 1984, **8**, 199–203.

45. C.P. Please, P.H. Hagan and D.W. Schwendeman, *SIAM Journal on Applied Mathematics*, 1994, **54**, 72-92.

46. S.R. Logan, *Journal of Chemical Education*, 1984, **59**, 279.

47. S. Bagheri, N. Muhd Julkapli and S. Bee Abd Hamid, *Scientific World Journal*, 2014, **2014**.

48. H. Becker, R. Güttel and T. Turek, *Catalysis Science and Technology*, 2016, **6**, 275–287.

49. D. Song and J. Li, *Journal of Molecular Catalysis A: Chemical*, 2006, **247**, 206–212.

50. R.M. German, *Woodhead Publishing Series in Metals and Surface Engineering*, 2010, 3-32.

51. M. Zanoletti, F. Godard and M. Perrier, *Canadian Journal of Chemical Engineering*, 2020, **98**, 2205–2213.

52. T. W. van Deelen, C. Hernández Mejía and K. P. de Jong, *Nature Catalysis*, 2019, **2**, 955–970.

53. S. Zhang, P. N. Plessow, J. J. Willis, S. Dai, M. Xu, G. W. Graham, M. Cargnello, F. Abild-Pedersen and X. Pan, *Nano Letters*, 2016, **16**, 4528–4534.

54. M. G. Willinger, W. Zhang, O. Bondarchuk, S. Shaikhutdinov, H. J. Freund and R. Schlögl, *Angewandte Chemie - International Edition*, 2014, **53**, 5998–6001.

55. P. Politzer and J. S. Murray, *Journal of Molecular Modeling*, 2018, **24**, 214.

56. R. Horn and R. Schlögl, *Catalysis Letters*, 2015, **145**, 23–39.

57. C. X. Zhou and T. R. Cundari, *ACS Omega*, 2019, **4**, 20159–20163.

58. T. Kwan and M. Jordan, *Chemical Physics Letters*, 2018, **708**, 216–221.

59. C. D. Elvidge, D. Ziskin, K. E. Baugh, B. T. Tuttle, T. Ghosh, D. W. Pack, E. H. Erwin and M. Zhizhin, *Energies*, 2009, **2**, 595–622.

60. R. Mansoor and M. Tahir, *Energy and Fuels*, 2021, **35**, 3675–3714.

61. A. Abdulrasheed, A. A. Jalil, Y. Gambo, M. Ibrahim, H. U. Hambali and M. Y. Shahul Hamid, *Renewable and Sustainable Energy Reviews*, 2019, **108**, 175–193.

62. C. Smith, A. K. Hill and L. Torrente-Murciano, *Energy and Environmental Science*, 2020, **13**, 331–344.

63. F. Dalena, A. Senatore, A. Marino, A. Gordano, M. Basile and A. Basile, *Science and Engineering*, 2018, 3-28.

64. A. P. Steynberg, *Studies in Surface Science and Catalysis*, 2004, **152**, 1-63.

65. G. Jones, J. G. Jakobsen, S. S. Shim, J. Kleis, M. P. Andersson, J. Rossmeisl, F. Abild-Pedersen, T. Bligaard, S. Helveg, B. Hinnemann, J. R. Rostrup-Nielsen, I. Chorkendorff, J. Sehested and J. K. Nørskov, *Journal of Catalysis*, 2008, **259**, 147–160.

66. J. Sehested, *Catalysis Today*, 2006, **111**, 103–110.

67. U. Erlekam, U. A. Paulus, Y. Wang, H. P. Bonzel, K. Jacobi and G. Ertl, *Zeitschrift für Physikalische Chemie,* 2005, **219**, 891-903.

68. M. Ghoussoub, S. Yadav, K. K. Ghuman, G. A. Ozin and C. V. Singh, *ACS Catalysis*, 2016, **6**, 7109–7117.

69. N. A. K. Aramouni, J. G. Touma, B. A. Tarboush, J. Zeaiter and M. N. Ahmad, *Renewable and Sustainable Energy Reviews*, 2018, **82**, 2570–2585.

70. M. C. J. Bradford and M. A. Vannice, *Catalysis Reviews Science and Engineering*, 1999, **41**, 1–42.

71. G. Valderrama, C. Urbina De Navarro and M. R. Goldwasser, *Journal of Power Sources*, 2013, **234**, 31–37.

72. M. P. Bracciale, B. de Caprariis, P. de Filippis and M. Scarsella, *Chemical Engineering Transactions*, 2019, **73**, 19–24.

73. C. Ruocco, B. de Caprariis, V. Palma, A. Petrullo, A. Ricca, M. Scarsella and P. de Filippis, *Journal of CO2 Utilization*, 2019, **30**, 222–231.

74. J. Du, X. X. Yang, J. Ding, X. L. Wei, J. P. Yang, W. L. Wang and M. L. Yang, *Journal of Central South University*, 2013, **20**, 1307–1313.

75. X. Cui and S. K. Kær, *Chemical Engineering Journal*, 2020, **393**, 124632.

76. B. Christian Enger, R. Lødeng and A. Holmen, *Applied Catalysis A: General*, 2008, **346**, 1–27.

77. S. C. Tsang, J. B. Claridge and M. L. Green, *Catalysis Today*, 1995, **23**, 3–15.

78. A. P. E. York, T. Xiao and M. L. H. Green, *Topics in Catalysis*, 2003, **22**, 345–358.

79. S. Grundner, W. Luo, M. Sanchez-Sanchez and J. A. Lercher, *Chemical Communications*, 2016, **52**, 2553–2556.

80. G. N. Mazo, O. A. Shlyakhtin, A. S. Loktev and A. G. Dedov, *Russian Chemical Bulletin*, 2019, **68**, 1949–1953.

81. J. B. Claridge, M. L. H. Green, S. C. Tsang, A. P. E. York, A. T. Ashcroft and P. D. Battle, *Catalysis Letters*, 1993, **22**, 299–305.

82. M.G. Poirier and J. Trudel, *Catalysis Letters*, 1993, **21**, 99-111.

83. P.D.F. Vernon, M.L.H. Green, A.K. Cheetham and A.T. Ashcroft, *Catalysis Letters*, 1990, **6**, 181-186.

84. T. Chomboon, W. Kumsung, M. Chareonpanich, S. Senkan and A. Seubsai, *Catalysts*, 2019, **9**, 335.

85. K. Nakagawa, K. Anzai, N. Matsui, N. Ikenaga, T. Suzuki and Y. Teng, T. Kobayashi and M. Haruta, Catalysis Letters, 1998, **51**, 163-167.

86. D. Ciuparu, M. R. Lyubovsky, E. Altman, L. D. Pfefferle and A. Datye, *Catalysis Reviews Science and Engineering*, 2002, **44**, 593–649.

87. J. H.Lee and D. L. Trimm, *Fuel Processing Technology*, 1995, **42**, 339-359.

88. M. Monai, T. Montini, R. J. Gorte and P. Fornasiero, *European Journal of Inorganic Chemistry*, 2018, **2018**, 2884–2893.

89. R. Burch and F. J. Urbano, *Applied Catalysis A, General*, 1995, **124**, 121–138.

90. Q. Duan, C. Zhang, S. Sun, Y. Pan, X. Zhou, Y. Liu, K. Chen, C. Li, X. Wang and W. Li, *Journal of Materials Chemistry A*, 2020, **8**, 7395–7404.

91. R. Burch, F. J. Urbano and P. K. Loader, *Applied Catalysis A, General*, 1995, **123**, 173–184.

92. S. Specchia, E. Finocchio, G. Busca, P. Palmisano and V. Specchia, *Journal of Catalysis*, 2009, **263**, 134–145.

93. M. Rotko, A. Machocki and B. Stasinska, *Applied Surface Science*, 2010, **256**, 5585–5589.

94. A. Hellman, A. Resta, N. M. Martin, J. Gustafson, A. Trinchero, P. A. Carlsson, O. Balmes, R. Felici, R. van Rijn, J. W. M. Frenken, J. N. Andersen, E. Lundgren and H. Grönbeck, *Journal of Physical Chemistry Letters*, 2012, **3**, 678–682.

95. M. Lyubovsky and L. Pfefferle, *Applied Catalysis A: General*, 1998, **173**, 107–119.

96. S. H. Oh and P. J. Mitchell, *Applied Catalysis B, Environmental*, 1994, **5**, 165–179.

97. S. K. Matam, M. H. Aguirre, A. Weidenkaff and D. Ferri, *Journal of Physical Chemistry C*, 2010, **114**, 9439–9443.

98. K. Murata, D. Kosuge, J. Ohyama, Y. Mahara, Y. Yamamoto, S. Arai and A. Satsuma, *ACS Catalysis*, 2020, **10**, 1381–1387.

99. V. H. Nissinen, N. M. Kinnunen and M. Suvanto, *Applied Catalysis B: Environmental*, 2018, **237**, 110–115.

100. W. R. Schwartz, D. Ciuparu and L. D. Pfefferle, *Journal of Physical Chemistry C*, 2012, **116**, 8587–8593.

101. J. M. Jones, V. A. Dupont, R. Brydson, D. J. Fullerton, N. S. Nasri, A. B. Ross and A. V. K. Westwood, *Catalysis Today*, 2003, **81**, 589–601.

102. Y. Zhang, P. Glarborg, K. Johansen, M. P. Andersson, T. K. Torp, A. D. Jensen and J. M. Christensen, *ACS Catalysis*, 2020, **10**, 1821–1827.

103. C. G. Freyschlag and R. J. Madix, *Materials Today*, 2011, **14**, 134–142.

104. Z. Hu, Z. Wang, Y. Guo, L. Wang, Y. Guo, J. Zhang and W. Zhan, *Environmental Science and Technology*, 2018, **52**, 9531–9541.

105. Zhe21

106. C. E. Düllmann, B. Eichler, R. Eichler, H. W. Gäggeler and A. Türler, *Journal of Physical Chemistry B*, 2002, **106**, 6679–6684.

107. Z. Hölgye and M. Křivánek, *Journal of Radioanalytical Chemistry*, 1978, **42**, 133–141.

108. I. Kajan, "Transport and Containment Chemistry of Ruthenium under Severe Accident Conditions in a Nuclear Power Plant", Chalmers University of Technology, Sweden, 2016.

109. C. K. Ryu, M. W. Ryoo, I. S. Ryu and S. K. Kang, *Catalysis Today*, 1999, **47**, 141–147.

110. W. Kumsung, M. Chareonpanich, P. Kongkachuichay, S. Senkan and A. Seubsai, *Catalysis Communications*, 2018, **110**, 83–87.

111. K. Nakagawa, T. Suzuki, T. Kobayashi and M. Haruta, *Chemistry Letters*, 1996, **25**, 1029-1030.

112. Z. Liang, T. Li, M. Kim, A. Asthagiri and J. F. Weaver, *Science*, 2017, **356**, 299–303.

113. M. Kim, A. Franklin, R. Martin, F. Feng, T. Li, Z. Liang, A. Asthagiri and J. F. Weaver, *Journal of Physical Chemistry C*, 2019, **123**, 27603-27614.

114. C. C. Wang, S. S. Siao and J. C. Jiang, *Journal of Physical Chemistry C*, 2012, **116**, 6367–6370.

115. Y. C. Liu, C. H. Yeh, Y. F. Lo, S. Nachimuthu, S. D. Lin and J. C. Jiang, *Journal of Catalysis*, 2020, **385**, 265–273.

116. D. Ferri and L. Forni, *Applied Catalysis B: Environmental*, 1998, **16**, 119-126.

117. H. C. Yao and Y. F. Y. Yao, *Journal of Catalysis*, 1984, **86**, 254–265.

118. M. C. Marion, E. Garbowski and M. Primet, *Journal of the Chemical Society Faraday Transactions*, 1990, **86**, 3027–3032.

119. M. I. Zaki, M. A. Hasan, L. Pasupulety, N. E. Fouad and H. Knözinger, *New Journal of Chemistry*, 1999, **23**, 1197–1202.

120. T.-C. Xiao, S.-F. Ji, H. T. Wang, K. S. Coleman and M. L. H. Green, *Journal of Molecular Catalysis A: Chemical*, 2001, **175**, 111–123.

121. Q. Shen, C. Cao, R. Huang, L. Zhu, X. Zhou, Q. Zhang, L. Gu and W. Song, *Angewandte Chemie*, 2020, **132**, 1232–1235.

122. A. Trovarelli, *Catalysis Reviews Science and Engineering*, 1996, **38**, 439–520.

123. T. Montini, M. Melchionna, M. Monai and P. Fornasiero, *Chemical Reviews*, 2016, **116**, 5987–6041.

124. J. Kašpar, P. Fornasiero and M. Graziani, *Catalysis Today*, 1999, **50**, 285–298.

125. A. Cimino and F. S. Stone, *Advances in Catalysis*, 2002, **47**, 141–306.

126. S. Cimino, L. Lisi, R. Pirone, G. Russo and M. Turco, *Catalysis Today*, 2000, **59**, 19–31.

127. V. Bashan and Y. Ust, *International Journal of Energy Research*, 2019, **43**, 7755–7789.

128. J. Yang and Y. Guo, *Chinese Chemical Letters*, 2018, **29**, 252–260.

129. S. Wendt, A. P. Seitsonen, Y. D. Kim, M. Knapp, H. Idriss and H. Over, *Surface Science*, 2002, **505**, 137–152.

130. W. Borchardt-Ott and H. Sowa, „Kristallographie", 9.Auflage, *Springer*, 2013, Heidelberg.

131. A. A. Bolzan, C. Fong, B. J. Kennedy and C. J. Howard, *Acta Crystallographica Section B: Structural Science*, 1997, **53**, 373–380.

132. C. L. McDaniel and S. J. Schneider, *Journal of Research of the National Bureau of Standards Section A: Physics and Chemistry*, 1969, **73A**, 213.

133. R. Schlögl, *Angewandte Chemie Int. Ed.*, 2015, **54**, 3465-3520.

134. I. E. Wachs and K. Routray, *ACS Catalysis*, 2012, **2**, 1235-1246.

135. J. Perez-Ramirez, C. Mondelli, T. Schmidt, O. F. K. Schlüter, A. Wolf, L. Mleczko and T. Dreier, *Energy Environmental Science*, 2011, **4**, 4786-4799.

136. H. Over and R. Schomäcker, *ACS Catalysis*, 2013, **3**, 1034-1046.

137. R. Lin, A. P. Amrute and J. Perez-Ramirez, *Chemical Reviews*, 2017, **117**, 4184-4247.

138. S. Trasatti, *Electrochimica Acta*, 2000, **45**, 2377-2385.

139. R. S. Yeo, J. Orehotsky, W. Visscher and S. Srinivasan, *Journal Electrochemical Society*, 1981, **128**, 1900–1904.

140. R. Hutchings, K. Müller, R. Kötz and S. Stucki, *Journal of Materials Science*, 1984, **19**, 3987–3994.

141. R. Kötz and S. Stucki, *Journal of The Electrochemical Society*, 1985, **132**, 103–107.

142. C. Angelinetta, S. Trasatti, L. D. Atanososka and R. T. Atanasoski, *Journal of Electroanalytical Chemistry*, 1986, **214**, 535–546.

143. C. Angelinetta, S. Trasatti, L. D. Atanasoska, Z. S. Minevski and R. T. Atanasoski, *Materials Chemistry and Physics*, 1989, **22**, 231–247.

144. L. Atanasoska, R. Atanasoski and S. Trasatti, *Vacuum*, 1990, **40**, 91–94.

145. C. C. Hu, Y. H. Huang and K. H. Chang, *Journal of Power Sources*, 2002, **108**, 117–127.

146. M. Blouin and D. Guay, *Journal of The Electrochemical Society*, 1997, **144**, 573–581.

147. L. E. Owe, M. Tsypkin, K. S. Wallwork, R. G. Haverkamp and S. Sunde, *Electrochimica Acta*, 2012, **70**, 158–164.

148. N. Danilovic, R. Subbaraman, K. C. Chang, S. H. Chang, Y. J. Kang, J. Snyder, A. P. Paulikas, D. Strmcnik, Y. T. Kim, D. Myers, V. R. Stamenkovic and N. M. Markovic, *Journal of Physical Chemistry Letters*, 2014, **5**, 2474–2478.

149. S. Cherevko, S. Geiger, O. Kasian, N. Kulyk, J.-P. Grote, A. Savan, B. R. Shrestha, S. Merzlikin, B. Breitbach, A. Ludwig, K. J. J. Mayrhofer, *Catalysis Today*, 2016, 262, 170-180.

150. L. Bai, Z. Duan, X. Wen, R. Si, Q. Zhang and J. Guan, *ACS Catalysis*, 2019, **9**, 9897–9904.

151. J.-M. Hu, J.-Q. Zhang and C.-N. Cao, *International Journal of Hydrogen Energy*, 2004, **29**, 791–797.

152. D. Lebedev, M. Povia, K. Waltar, P. M. Abdala, I. E. Castelli, E. Fabbri, M. v. Blanco, A. Fedorov, C. Copéret, N. Marzari and T. J. Schmidt, *Chemistry of Materials*, 2017, **29**, 5182–5191.

153. O. Kasian, S. Geiger, P. Stock, G. Polymeros, B. Breitbach, A. Savan, A. Ludwig, S. Cherevko and K. J. J. Mayrhofer, *Journal of Electrochemical Society*, 2016, **163**, 3099-3104.

154. M. E. G. Lyons and S. Floquet, *Physical Chemistry Chemical Physics*, 2011, **13**, 5314–5335.

155. R. K. B. Karlsson and A. Cornell, *Chemical Reviews*, 2016, **116**, 2982-3028.

156. T. Reier, H. N. Nong, D. Teschner, R. Schlögl and P. Strasser, *Advanced Energy Materials*, 2017, **7**, 1601275.

157. R. Kötz and S. Stucki, *Electrochimica Acta*, 1986, **31**, 1311-1316.

158. T. Hachiya, T. Sasaki, K. Tsuchida and H. Houda, *ECS Transactions*, 2009, **16**, 31-39.

159. H. Over, *Chemical Reviews*, 2012, **112**, 3356–3426.

160. V. Trieu, B. Schley, H. Natter, J. Kintrup, A. Bulan and R. Hempelmann, *Electrochimica Acta*, 2012, **78**, 188–194.

161. Y. Takasu, S. Onoue, K. Kameyama, Y. Murakami and K. Yahikozawa, *Electrochimica Acta*, 1994, **39**, 1993–1997.

162. S. Barison, S. Daolio, M. Fabrizio and A. de Battisti, *Rapid Communications in Mass Spectrometry*, 2004, **18**, 278–284.

163. M. C. Medeiros, J. B. de Medeiros, C. A. Martinez-Huitlem T. M. B. F. Oliviera, S. E. Mazzetto, F. F. M. da Silva and S. S. L. Castro, *Seperation and Purification Technology*, 2021, **264**, 118425.

164. I. M. Kodintsev, S. Trasatti, M. Rubel, A. Wieckowski and N. Kaufher, *Langmuir*, 1992, **8**, 283–290.

165. I. A. Lervik, M. Tsypkin, L. E. Owe and S. Sunde, *Journal of Electroanalytical Chemistry*, 2010, **645**, 135–142.

166. J. Cheng, H. Zhang, G. Chen and Y. Zhang, *Electrochimica Acta*, 2009, **54**, 6250–6256.

167. H. Okamoto, P. R. Subramanian and L. Kacprzak, *ASM International*, 1990, **3**, 2348.

168. S. A. M. Lima, F. A. Sigoli, M. R. Davolos and M. Jafelicci Jr., *Journal Alloys and Compounds*, 2002, **344**, 280-284.

169. S. Soisuwan, J. Panpranot, D. L. Trimm and P. Praserthdam, *Applied Catalysis A*, 2006, **303**, 268-272.

170. B. Caglar and B. Uner, *Catalysis Communications*, 2011, **12**, 450-453.

171. H. Tran, T. Mehta, M. Zeller and R. H. Jarman, *Materials Research Bulletin*, 2013, **48**, 2450-2456.

172. N. Mamaca, E. Mayousse, S. Arrii-Clacens, T. W. Napporn, K. Servat, N. Guillet, K. B. Kokoh, *Applied Catalysis B*, 2012, **112**, 376-380.

173. A. Rosario, L. Bulhoes and E. Pereira, *Journal of Power Sources*, 2006, **158**, 795-800.

174. A. J. Terezo and E. C. Pereira, *Materials Letters*, 2002, **53**, 339-345.

175. A. Reksten, F. Moradi, F. Seland and S. Sunde, *ECS Transactions*, 2014, **58**, 39-50.

176. M. P. Pechini, US Patent 3,330,697, 1967.

177. L. Dimesso, "Pechini Processes: An Alternate Approach of the Sol-Gel Method, Preparation, Properties, and Applications", in L. Klein and M. Aparicio,"Handbook of Sol-Gel Science and Technology", *Springer*, 2018, Cham.

178. T. O. L. Sunde, T. Grande and M. A. Einarsrud, "Modified Pechini Synthesis of Oxide Powders and Thin Films", in L. Klein and M. Aparicio,"Handbook of Sol-Gel Science and Technology", *Springer*, 2018, Cham.

179. T. T. Pham, S. G. Kang and E. W. Shin, *Applied Surface Science*, 2017, **411**, 18–26.

180. E. N. Balko and C. R. Davidson, *Journal of Inorganic and Nuclear Chemistry*, 1980, **42**, 1778-1781.

181. A. R. Denton and N. W. Ashcroft, *Physical Review A*, 1991, **43**, 3161.

182. G. E. M. JAUNCEY, *Proceedings of the National Academy of Sciences*, 1924, **10**, 57-60.

183. I. Lukačević, S. K. Gupta, P. K. Jha and D. Kirin, *Materials Chemistry and Physics*, 2012, **137**, 282–289.

184. Y. bin Cho, A. Yu, C. Lee, M. H. Kim and Y. Lee, *ACS Applied Materials and Interfaces*, 2018, **10**, 541–549.

185. C. H. Henry and J. J. Hopfield, *Physical Review Letter*s, 1965, **15**, 964-966.

186. A. C. Wiesheu, „Raman-Mikroskopie zur Analyse von organischen Bodensubstanzen und Mikroplastik", Technische Universität Münschen, 2017.

187. H. J. Lewerenz, S. Stucki and R. Kötz, *Surface Science*, 1983, **126**, 463–468.

188. H.-J. Freund, G. Meijer, M. Scheffler, R. Schlögl and M. Wolf, *Angewandte Chemie Int. Ed.*, 2011, **50**, 10064-10094.

189. R. Klaewkla, M. Arend and W. F. Hoelderich, "A Review of Mass Transfer Controlling the Reaction rate in Heterogenous Catalytic Systems", in H. Nkajima, "Mass Transfer – Advanced Aspects", *IntechOpen*, 2011, Japan.

190. D. Mu, Z. S. Liu, C. Huang and N. Djilali, *Microfluidics and Nanofluidics*, 2008, **4**, 257–260.

191. S. A. Smyth, K. T. Christensen and D. C. Kyritsis, *Proceedings of the Combustion Institute*, 2009, **32**, 3035–3042.

192. D. B. Jaynes and A. S. Rogowski, *Soil Science Society of America Journal*, 1983, **47**, 425-430.

193. Vorlesungsskript „Grundzüge der Technischen Chemie II – Chemische Reaktionskinetik", Universität Bochum, WS 2004/2005.

194. M. Boudart, *Chemical Reviews*, 1995, **95**, 661–666.

195. T. F. Garetto, E. Rincón and C. R. Apesteguía, *Applied Catalysis B: Environmental*, 2004, **48**, 167–174.

196. S. H. Oh, P. J. Mitchell and R. M. Siewert, "Methane Oxidation over Noble Metal Catalysts as Related to Controlling Natural Gas Vehicle Exhaust", in R.G. Silver, J. E. Sawyer and J. C. Summers, "Catalytic Control of Air Pollution", *ACS Symposium Series*, 1992, **495**, Chapter 2: 12-25.

197. A. Frennet, *Catalysis Reviews Science Engineering*, 1974, **10**, 37–68.

198. C. Kemball, *Advances in Catalysis*, 1959, **11**, 223–262.

199. S. Wendt, A. P. Seitsonen and H. Over, *Catalysis Today*, 2003, **85**, 167–175.

200. M. Kim, A. D. Franklin, R. Martin, Y. Bian, J. F. Weaver and A. Asthagiri, *Journal of Catalysis*, 2020, **383**, 181–192.

201. A. H. Reksten, A. E. Russel, P. W. Richardson, S. J. Thompson, K. Mathisen, F. Seland and S. Sunde, *Phys. Chem. Chem. Phys.*, 2019, **21**, 12217-12230.

202. R. S. Chen, Y. S. Huang, Y. M. Liang, D. S. Tsai and K. K. Tiong, *Journal Alloys and Compounds*, 2004, **383**, 273-276.

203. S. Y. Mar, C. S. Chen, Y. S. Huang and K. K. Tiong, *Applied Surface Scienc*, 1995, **90**, 497-504.

204. J.A. Rodriguez and D.W. Goodman, *Science*, 1992, **257**, 897-893.

205. S. J. Freakley, J. Ruiz-Esquius, D. J. Morgan, *Surface Interface Analysis*, 2017, **49**, 794-799.

206. P. Steiner and S. Hüfner, *Solid State Communications*, 1981, **37**, 79-81.

207. P. Steiner, S. Hüfner, N. Martensson and B. Johansson, *Solid State Communications*, 1981, **37**, 73-77.

208. W. Olovsson, L. Bech, T. H. Andersen, Z. Li, S. V. Hoffmann, B. Johansson, I. A. Abrikosov and J. Oasgaard, *Journal Physical Review B*, 2005, **72**, 075444.

209. H. Over, A.P. Seitsonen, E. Lundgren, M. Semdh and J. N. Andersen, *Surface Science*, 2002, **504**, 196-200.

210. Z. Mao and C. T. Campbell, *ACS Catalysis*, 2019, **9**, 9465–9473.

211. D. Y. Murzin, *Catalysis Letters*, 2019, **149**, 1455–1463.

212. A. Farkas, G. C. Mellau and H. Over, *Journal of Physical Chemistry C*, 2009, **113**, 14341–14355.

213. A. S. Dobrota and I. A. Pasti, *Journal Electrochemical Science Engineering*, 2020, **10**, 141-159.

214. A. Farkas, F. Hess and H. Over, *Journal Physical Chemistry C*, 2012, **116**, 581-591.

215. F. Hess, A. Farkas, A. P. Seitsonen and H. Over, *Journal of Computational Chemistry*, 2012, **33**, 757–766.

216. C. Bläker, „Experimentelle und theoretische Untersuchungen zur Kombination von Adsorptionsvolumetrie und- kalorimetrie", Universität Duisburg-Essen, 2018.

217. C. H. Yeh, B. C. Ji, S. Nachimuthu and J. C. Jiang, *Applied Surface Science*, 2021, **539**, 148244.

218. H. Over, Y. D. Kim, A. P. Seitsonen, S. Wendt, E. Lundgren, M. Schmid, P. Varga, A. Morgante and G. Ertl, *Science*, 2000, **287**, 1474–1476.

219. M. Abb, T. Weber, L. Glatthaar, *Langmuir*, 2019, **35**, 7720-7726.

220. M. Abb, T. Weber, D. Langsdorf, V. Koller, S. M. Gericke, S. Pfaff, J. Zetterberg, A. Preobrajenski, H. Grönbeck and E. Lundgren et al., *Journal Physical Chemistry C*, 2020, **124**, 15324-15336.

221. J. Assmann, V. Narkhede, N.A. Breuer, M. Muhler, A.P. Seitsonen, M. Knapp, D. Crihan, A. Farkas, G. Mellau and H. Over, *Journal Physics: Condensed Matter*, 2008, **20**, 184017.

222. D. Rosenthal, F. Girgsdies, O. Timpe, R. Blume, G. Weinberg, D. Teschner and R. Schlögl, *Zeitschrift Physikalische Chemie*, 2009, **223**, 183-207.

223. N. W. Cant, P. C. Hicks, B. S. Lennon, *Journal Catalysis*, 1978, **54**, 372-383.

224. J. T. Kiss, R. D. Gonzalez, *Journal Physical Chemistry*, 1984, **88**, 892-897.

225. J. Assmann, E. Löffler, A. Birkner, M. Muhler, *Catalysis Today*, 2003, **85**, 235-249.

226. Y. He, D. Langsdorf, L. Li and H. Over, *Journal of Physical Chemistry C*, 2015, **119**, 2692–2702.

227. G. Xiang, X. Shi, Y. Wu, J. Zhuang and X. Wang, *Scientific Reports*, 2012, **2**.

228. T. Weber, V. Vonk, M. J. S. Abb, J. Evertsson, M. Sandroni, J. Drnec, A. Stierle, E. Lundgren and H. Over, *Journal of Physical Chemistry Letters*, 2020, **2**, 9057–9062.

229. G. Novell-Leruth, G. Carchini and N. López, *Journal of Chemical Physics*, 2013, **138**, 194706.

230. Y. Lykhach, J. Kubát, A. Neitzel, N. Tsud, M. Vorokhta, T. Skála, F. Dvořák, Y. Kosto, K. C. Prince, V. Matolín, V. Johánek, J. Mysliveček and J. Libuda, *Journal of Chemical Physics*, 2019, **151**, 204703.

231. J. Nilsson, P. A. Carlsson, S. Fouladvand, N. M. Martin, J. Gustafson, M. A. Newton, E. Lundgren, H. Grönbeck and M. Skoglundh, *ACS Catalysis*, 2015, **5**, 2481–2489.

232. M. Cargnello, J. J. Delgado Jaén, J. C. Hernández Garrido, K. Bakhmutsky, T. Montini, J. J. Calvino Gámez, R. J. Gorte and P. Fornasiero, *Science*, 2012, **337**, 713–717.

233. M. van den Bossche and H. Grönbeck, *Journal of the American Chemical Society*, 2015, **137**, 12035–12044.

234. M. Knapp, D. Crihan, A. P. Seitsonen, E. Lundgren, A. Resta, J. N. Andersen and H. Over, *Journal of Physical Chemistry C*, 2007, **111**, 5363–5373.

235. T. Li, M. Kim, Z. Liang, A. Asthagiri and J. F. Weaver, *Topics in Catalysis*, 2018, 61, 397–411.

236. P. Gélin, L. Urfels, M. Primet and E. Tena, *Catalysis Today*, 2003, **83**, 45–57.

237. J. Okal, M. Zawadzki and K. Baranowska, *Applied Catalysis B: Environmental*, 2016, **194**, 22–31.

238. T. R. Baldwin and R. Burch, *Applied Catalysis*, 1990, **66**, 337–358.

239. Y. Chen, J. Lin, X. Chen, S. Fan and Y. Zheng, *Catalysis Science and Technology*, 2021, **11**, 152–161.

240. P. Gélin and M. Primet, *Applied Catalysis B: Environmental*, 2002, **39**, 1–37.

241. H. Yoshida, T. Nakajima, Y. Yazawa and T. Hattori, *Applied Catalysis B: Environmental*, 2007, **71**, 70–79.

242. O. Demoulin, B. le Clef, M. Navez and P. Ruiz, *Applied Catalysis A: General*, 2008, **344**, 1–9.

243. N. M. Kinnunen, J. T. Hirvi, K. Kallinen, T. Maunula, M. Keenan and M. Suvanto, *Applied Catalysis B: Environmental*, 2017, **207**, 114–119.

11. List of abbreviations

BET	Brunauer-Emmet-Teller
C	carbon
CER	chlorine evolution reaction
CPOM	catalytic partial oxidation of methane
DFT	discrete fourier transform
DRIFTS	diffuse reflectance infrared fourier transform spectroscopy
DRM	dry reforming of methane
DSA	dimensionally stable anodes
EDS	energy-dispersive x-ray spectroscopy
FWHM	Full width at half maximum
H	hydrogen
HER	hydrogen evolution reaction
HRTEM	high resolution transmission electron microscopy
Ir	iridium
LNG	liquefied natural gas
MFC	mass flow controller
MFM	mass flow meter
NIST	National Institute of Standards and Technology
NDIR	non-dispersive infrared
NO_x	nitrogen oxides
O	oxygen
OER	oxygen evolution reaction
Pd	palladium
Rh	rhodium
Ru	ruthenium
SAED	selected area electron diffraction
SEM	scanning electron microscopy
SMR	steam methane reforming
STEM	scanning transmission electron microscopy
STY	space time yield
TCD	thermal conductivity detector
TEM	transmission electron microscopy
Ti	titanium
TGA	thermogravimetric analysis
TOF	turn over frequency
TPR	temperature programmed reaction
UHV	ultra-high vacuum
XRD	x-ray diffraction
XPS	x-ray photoelectron spectroscopy